KU LEUVEN

ARENBERG DOCTORAL SCHOOL
Faculty of Engineering Science

A high frequency rheometrical study on colloidal suspensions

Bram Schroyen

Supervisor:
Prof. dr. ir. Peter Van Puyvelde

Dissertation presented in partial fulfilment of the requirements for the degree of Doctor of Engineering Science (PhD): Chemical Engineering

September 2018

A high frequency rheometrical study on colloidal suspensions

Bram SCHROYEN

Examination committee:
Prof. dr. ir. P. Wollants, chair
Prof. dr. ir. P. Van Puyvelde, supervisor
Prof. dr. ir. J. Degrève
Prof. dr. ir. S. Kuhn
Prof. dr. C. Clasen
Prof. dr. N. Willenbacher
(Karlsruhe Institute of Technology)

Dissertation presented in partial fulfilment of the requirements for the degree of Doctor of Engineering Science (PhD): Chemical Engineering

September 2018

© 2018 KU Leuven – Faculty of Engineering Science
Uitgegeven in eigen beheer, Bram Schroyen, Celestijnenlaan 200F box 2424, B-3001 Leuven (Belgium)

Alle rechten voorbehouden. Niets uit deze uitgave mag worden vermenigvuldigd en/of openbaar gemaakt worden door middel van druk, fotokopie, microfilm, elektronisch of op welke andere wijze ook zonder voorafgaande schriftelijke toestemming van de uitgever.

All rights reserved. No part of the publication may be reproduced in any form by print, photoprint, microfilm, electronic or any other means without written permission from the publisher.

Disperge et impera.

SCAN WITH YOUR SMARTPHONE AND BE AMAZED*:

*Android: enable NFC in settings and tag
*iOS 11 (or higher): download and open NFC app

Preface

During the past 4 years, I have often received the question 'what it feels like to do a PhD'. I have never been able to come up with a comprehensive response to this question. Partially, this is caused by the fact that giving clear responses was never my strongest suit (as many readers might affirm). The main reason though is that a PhD is such a complex, many-sided and personal journey. Personally, I loved it from the start. It is definitely challenging, it can be frustrating by times, and often you feel like you are in way over your head. But at the same time it's a highly rewarding journey that keeps you at the edge of your seat throughout. One of the biggest rewards are the people that I met. The incredible diversity in backgrounds and cultures that I encountered will make me richer for the rest of my life. Before delving into the science, this section is devoted to acknowledge that.

Jan and Peter, I want to begin with thanking you for giving me the opportunity to start this PhD. Coming from interfacial rheology I was already happy that preparing for a measurement took less than half a day, but boy oh boy it turned out to be even better than that. However, my gratitude goes much deeper than this, because you have both shown to be good and caring persons. The past years might have been complicated from an organisational point of view, but we succeeded in finding a good balance. Peter, I want to thank you for always supporting me, giving me opportunities and for allowing me to explore further. Jan, your guidance together with the many challenges that you gave me have continuously stimulated me and allowed me to grow beyond my limits, and I will always be grateful for that.

Although I am taking credit for the work in this thesis, I would never have been able to realise it without the help of many people. First of all, I acknowledge SIM Flanders for providing funding for this project. I want to thank Günter Auernhammer and Shilin Huang from MPI for introducing me to the world of high-frequency rheometry. Werner and Christian for their help with constructing the high-frequency setups and for being incredibly accurate. Herman and Hanne,

for all the times that I passed by for advice or to fix something. Ljiljana, Romana, Gabriele and Chiao for the finest particle synthesis. Jim Swan from MIT for his help with interpreting the data. Jan Mewis and Norm Wagner for writing 'Colloidal suspension rheology' - this has been my bible for the past years. Marie-Claude and Beatrice for way too much administrative work. And finally Anja and Nico, for organising and taking care of the group/lab: I truly believe that the lab would break down in an instant without you. Kirill, since you are the one that breaks down things this is probably not true, but you do make the lab a better place!

During my PhD I was lucky enough to feel at home in two different labs and I am grateful to everyone - smarties and softiez alike: (KUL) Rob, Ward, Wouter M, Wouter S, Gio, Stijn, Leander, Manish, Mr. T., Maya, Sebastian, An-Sofie, Robin, Yannick, Irene, Dries and Moritz ; (ETH) Raphi, Andy, Fotios, Manolis, Steffen, Martin, Nick, Mahesh, Damian, Laura, Rao, Roman, Iacopo, Julia, Peter, Mathias, Florian and Joe. Specifically I want to thank from Leuven: Greet for all the wonderful distractions, Mathieu for being a great teaching example, Jan for all the sarcasm, Ava just for being as you are, Steffen for sharing the heavy burden in our office (you know what I am talking about), Jasper and Helene for being *super*cute and Michael for being a point of reference. From Zürich: Gagik for all the random bullshit that can make anyone's day, Gert for being the other orphan, Alexandra for sharing my misery with rings, André for reminding me of skiing on a daily basis with your goggles, Victoria for the continuous background giggling, Lili for being delightful and Vappu for all the good care and for just being too nice. Other friends and colleagues in the trenches: Ale and Laura for being awesome, Martina and Dzemi, Lauriane - the french connection, Zsigi for road trips and talking even more than simulating,.. And finally Susa, Karel, Lisa and Franci - or Rachel, Ross, Phoebe and Mike in our own series - for a home outside of the lab as well.

Over the past years I have traveled and moved quite a bit between Belgium and Switzerland. At least enough to know all the shortcuts through Alsace or to know the best dining experiences along the highway. There are a few people that I want to thank for also making Zürich feel like home. Gabreli, for all the good times in- and outside of the lab, and in- and outside of Switzerland. From time to time I had to hand Gabo a few games in pool as a gift for saving friendship, but it has been worth it. And Raftina, for being a second family in Zürich. Raf and I forged a 'band of brothers' in the whom of Glandon apartments, and continue to experience similar entertaining complexities in our lives. I can truly say that the past years would not have been as good without you guys. Unfortunately, the frequent traveling - often within short notice - has also made it more difficult to organise things with friends. Nonetheless I am fortunate enough to have awesome friends, and I want to deeply thank all of them - being

from Heppen, Beverlo, Leuven, or from the St. M. Gangster squad - for always making me look forward to return to Belgium.

My inmost gratitude goes to my family, my parents and grandparents for their never ending love, care and support. Mama, papa, ik ben waar ik ben dankzij jullie, en dat zal ik nooit vergeten. Hoe ver ik ook ben, ik weet dat ik altijd een thuis heb waarop ik kan terugvallen (ik zal ook proberen dit niet té vol te stouwen), en dat is de belangrijkste wetenschap. Physically we might be further away, but we are close in heart.

And finally, as last but definitely not as least, Roby. From all the good things I have received from my 4 years of PhD, you have been the best. I am eternally thankful that, before starting your project, you had no clue of the amount of physics that is involved when studying suspensions and that you decided to work at our group. You have made my life many times more complex, but also more fun, more interesting, and frankly better in every way. The only thing that I regret is that I didn't invite you for pizza sooner..

Bram Schroyen

Abstract

Colloidal suspensions are present in a wide range of natural and synthetic applications. Their colloidal nature leads to a complex interplay between different interaction forces and defines their structure. In order to understand and manipulate the behaviour of a suspension, knowledge on the relationship between structure and properties is hence crucial. Rheology is particularly useful for deriving such relationships. Furthermore, it allows to investigate suspensions directly at relevant concentrations. Small amplitude oscillatory measurements are of particular interest: the potential of tuning the frequency of the oscillation makes it possible to vary both the time and length scale that is probed and allows to obtain an integrated fingerprint of the material.

Specifically, this thesis focuses on the potential role of rheology in determining local scale parameters of the colloidal building blocks in a suspension. In order to obtain information on the local scale, the applied frequency must be larger than the characteristic time scale of the colloidal suspension. Typically, such ranges are above the accessible frequency limit of standard devices, and we must therefore turn ourselves to non-conventional 'high-frequency' methods for studying the high-frequency response. A wide range of such methods have been developed in the past for studying various material classes. In our case, the aim is to characterise colloidal dispersions up until their high-frequency limiting region, in which hydrodynamics dominate the response. This region is typically reached from frequencies larger than 1 kHz. Going to excessively high frequencies is also not of interest, as the penetration depth of the deformation should be such that bulk properties are probed. Given these limitations, piezo rheometry offers the most simple and robust solution to investigate the local scale properties.

The first major part of this work concerns the development of a homebuilt piezo shear rheometer. The design phase of the rheometer was aided by simulating the electromechanical behaviour of the setup. A sensitive mechanical alignment method is installed for a fast and accurate gap control and is combined with a

careful signal analysis method for accurate measurements between 10 - 2000 Hz. The instrument directly extends the accessible frequency range of conventional rotational instruments into the low kHz region, and can hence be used to study the continuous transition of colloidal suspensions into the high-frequency regime. By applying a pure shear flow, material properties can be derived in a straightforward manner. However, near the device limits, certain correction factors have to be taken into account. Correction methods are proposed for the low- and high-frequency limits of the instrument, and for low-viscous fluids measured at intermediate to high frequencies. Calibration and validation results show that the piezo shear rheometer can accurately detect viscoelastic properties at amplitude ratios $> 7.1\sqrt{f}$ with an accuracy of $\approx 2°$ in phase.

The frequency range accessible by the piezo shear rheometer is used to study local scale properties in colloidal suspensions. The second part of this work focuses on stabilised suspensions, and more particularly on the interplay between the surface topology of colloids and the local stress contributions in a suspension. Model particles with different types of surface topologies are used, ranging from colloids with grafted polymer layers of varying layer thicknesses to charged raspberry-like particles with controllable surface roughness. The measured stress responses are rescaled to remove purely hydrodynamic components and to highlight the Brownian and interparticle contributions. At high frequencies, when the response probes contributions close to the particle surface, the results reveal an intricate interplay between hydrodynamic lubrication stresses, repulsive interactions and surface topology. Furthermore, the shear thickening behaviour of the various suspensions is experimentally determined. While such non-equilibrium behaviour fundamentally differs from the near-equilibrium high-frequency stress contributions, the interplay between surface topology and local scale stresses is also established here.

The third part discusses the use of high-frequency rheology to assess the local structure in partially dispersed suspensions. The degree of dispersion of colloidal particles in a suspension is crucial for many applications, and is for instance an important parameter for the performance of nanomaterials. Quantifying the degree of dispersion is often non-trivial. This chapter aims at deriving a direct relationship between rheological properties and the degree of dispersion from the loss modulus measured at high frequencies. Measurements on spherical silica particles, with a varying degree of dispersion in low molecular weight PDMS, are used to demonstrate how high-frequency rheometry can be used to quantify dispersion quality. The linear viscoelastic properties are compared to analytical scaling theories to demonstrate that a hydrodynamically dominated regime is reached. The dependency of the relative high-frequency loss modulus on volume fraction is then compared to predictions of a hydrodynamic viscosity model for the derivation of a dispersion quality index. In addition, it is used

to follow the evolution of the dispersion quality in a dispersion process as a function of mixing time and power input.

The findings presented in this thesis illustrate that high-frequency rheology is a sensitive tool to probe local scale properties in colloidal suspensions. By focusing on specific stress contributions, interaction parameters or local structural properties can directly be derived. Such relationships are useful in two ways. On one hand, knowledge on the properties of the colloidal building blocks will lead to an improved understanding of the complex phenomena that colloidal dispersions display, and will pave the way for improved model predictions. On the other hand, rheology is a versatile technique that allows to study suspensions directly at relevant concentrations. The possibility for using it as a probe to quantify local structural properties is highly relevant for many practical applications.

Samenvatting

Colloïdale suspensies zijn wijdverspreid en zijn terug te vinden in een groot aantal toepassingen. Aangezien deze materialen colloïdaal zijn zijn de oppervlakte-eigenschappen van groot belang. Deze leiden tot een complexe wisselwerking tussen verschillende interactiekrachten en zijn bepalend voor de microstructuur. Indien we colloïdale suspensies willen begrijpen en gebruiken is het dus cruciaal om de relatie tussen structuur enerzijds en eigenschappen anderzijds te kennen. Reologie is uitermate interessant om zulke relaties te bepalen en is algemeen toepasbaar. We concentreren ons vooral op frequentie-afhankelijke metingen uitgevoerd bij kleine amplitudes, of binnen de lineariteitsgrenzen van het materiaal. Het voordeel van dit type metingen is dat de onderzochte tijds- en lengteschaal kan gevarieerd worden door de frequentie van de meting aan te passen. Op die manier is het dus mogelijk een integraal beeld te krijgen van het materiaal.

Concreet onderzoeken we in deze thesis de mogelijke rol van reologie om lokale eigenschappen te bepalen van de bouwstenen in colloïdale suspensies. Om lokale informatie te vergaren moet de opgelegde frequentie van de metingen hoger zijn dan de karakteristieke frequentieschaal van colloïdale suspensies. Zulke frequenties zijn vaak hoger dan het meetbereik van commerciële toestellen. We moeten dus specifieke hoog-frequente methodes toepassingen om deze metingen uit te voeren. Het doel is om het gedrag van de suspensies te karakteriseren tot een hoog-frequent 'terminaal' gebied bereikt wordt waarin hydrodynamische effecten domineren. Dit gebied wordt typisch bereikt vanaf 1 kHz, afhankelijk van de specifieke eigenschappen van de suspensie. Een te hoge frequentie is ook ongewenst: de penetratiediepte van de opgelegde beweging daalt, en vanaf bepaalde frequenties ($\sim$ MHz) is het enkel mogelijk om oppervlakte-eigenschappen te meten. Gezien deze voorwaarden is piëzo reometrie de beste en meest robuuste methode om de lokale eigenschappen te bestuderen.

In het eerste deel van dit werk wordt de piëzo reometer besproken. Het ontwerp van de setup is mede tot stand gebracht door het elektromechanisch gedrag te

simuleren. De gevoeligheid van zowel de alignering als de meting zelf zijn van groot belang. De alignering gebeurt mechanisch en kan snel en accuraat worden gecontroleerd. De signaalanalyse is geoptimaliseerd voor metingen tussen 10 - 2000 Hz. Het instrument breidt het meetgebied van commerciële toestellen uit met 2 decades en laat dus toe om het gedrag van colloïdale suspensies te bestuderen tot in het hoog-frequent gebied. Materiaaleigenschappen kunnen rechtstreeks worden afgeleid en correctiefactoren zijn voorzien om het meetbereik uit te breiden wanneer de limieten van het toestel worden bereikt. De calibratieresultaten tonen aan dat de piëzo reometer in staat is om op kwantitatieve wijze viscoelastische materiaaleigenschappen te bepalen. De ondergrens van de amplitude ratio is $> 7.1\sqrt{f}$ terwijl de fout op de fasehoek maximum $\approx 2^\circ$ bedraagt.

De piëzo reometer is gebruikt om lokale eigenschappen in colloïdale suspensies te bestuderen. Het tweede deel van dit werk focust op stabiele suspensies. De wisselwerking tussen de oppervlakte-eigenschappen, en specifiek de topologie van het oppervlak, en de lokale interacties en spanningsbijdrages is bestudeerd. We veranderen de oppervlakte-eigenschappen op een gestructureerde manier en werken enerzijds met sterisch gestabiliseerde deeltjes met variërende polymeerketens en anderzijds met ladingsgestabiliseerde framboosvormige deeltjes met gecontroleerde oppervlakteruwheid. Pure hydrodynamische effecten worden verwijderd van de opgemeten spanningen door middel van een algemene herschaling. Op deze manier worden de interdeeltjes- en Browniaanse bijdrages direct onderzocht bij hogere frequenties, of op lengteschalen dichtbij het deeltjesoppervlak. De resultaten vertonen een complexe wisselwerking tussen hydrodynamische lubricatiespanningen, repulsieve interdeeltjesinteracties en oppervlaktetopologie.

In het derde deel wordt hoog-frequente reologie gebruikt om de lokale microstructuur in colloïdale suspensies te bepalen. Hier onderzoeken we attractieve of onstabiele suspensies die slechts gedeeltelijk zijn gedispergeerd. De dispersiegraad, of de kwaliteit van de suspensie, is van cruciaal belang voor verschillende toepassingen. Het bepaalt bijvoorbeeld voor een groot gedeelte de performantie van nanomaterialen. Het doel van het hoofdstuk is de afleiding van een directe relatie tussen de opgemeten reologische eigenschappen enerzijds en de dispersiekwaliteit anderzijds. Aan de hand van sferische silica partikels met variërende dispersiegraad in PDMS tonen we aan hoe hoog-frequente reologie hiervoor op een kwantitatieve manier kan worden gebruikt. We tonen aan dat een hoog-frequent gebied wordt bereikt waarin hydrodynamische effecten de spanningsbijdrage van de partikels bepaalt. Deze bijdrage is enkel afhankelijk van de lokale microstructuur en kan vergeleken worden met hydrodynamische viscositeitsmodellen. Op deze manier kan een index voor de dispersiegraad worden afgeleid die enkel afhankelijk is van de effectieve volumefractie van

partikels of aggregaten. Deze index kan bijvoorbeeld worden gebruikt om de evolutie van de dispersiegraad te volgen tijdens het dispergeren in een bepaald mengproces.

De resultaten in deze thesis tonen aan dat hoog-frequente reologie een gevoelige methode is om lokale eigenschappen te onderzoeken in colloïdale suspensies. Zowel interactieparameters als lokale structuureigenschappen kunnen worden bepaald. Dit kan op twee manieren van toepassing zijn. De vergaarde kennis over de interacties tussen en structuur van colloïdale bouwstenen leiden tot een beter begrip van het complex gedrag van suspensies. Reologie is ook een veelzijdige methode die toelaat om verschillende suspensies te onderzoeken en die geen verdunning vereist. De mogelijkheid om het bijvoorbeeld als sensor te gebruiken om lokale structuureigenschappen te kwantificeren is relevant voor vele toepassingen.

List of symbols

Symbol	Definition	Unit
a	particle radius	[m]
a_c	particle core radius	[m]
A	general representation for a constant	[-]
AR	amplitude ratio	[N·m^{-1}]
B	'Gleissle' shift factor	[-]
C	electric capacitance	[C·V^{-1}]
C	prefactor for rescaling the stress contributions	[-]
d_a	distance between surface asperities	[m]
d_f	fractal dimension	[-]
d_p	particle diameter	[m]
d_s	penetration depth of a shear wave	[m]
d_{15}	piezoelectric shear mode coupling coefficient	[m·V^{-1}]
d_{33}	piezoelectric thickness mode coupling coefficient	[m·V^{-1}]
D_a	aggregate diameter	[m]
$\mathcal{D}_0$	single-particle diffusivity	[m^2·s^{-1}]
$\mathcal{D}_{ss}$	short time self-diffusion coefficient	[m^2·s^{-1}]
$\mathbf{D}_E$	electric displacement field	[C·m^{-2}]
$\mathbf{E}$	electric field	[V·m^{-1}]
F	force	[N]
f	frequency	[Hz]
g	gravitational constant	[m·s^{-2}]
G	shear modulus	[Pa]
G^*	complex shear modulus	[Pa]
G'	elastic or storage modulus	[Pa]
G''	viscous or loss modulus	[Pa]
h	thickness/height of a topological feature	[m]
H	gap height	[m]
I	electric current	[A]
j	imaginary unit	[-]

K	spring constant	[N·m^{-1}]
K_c	correction constant for electric cross-talk	[N·m^{-1}]
k_B	Boltzmann's constant	[J·K^{-1}]
m	mass	[kg]
$\mathbf{n}$	normal vector	[m]
N_1	1st normal stress difference	[Pa]
N	mixing velocity	[s^{-1}]
N_p	amount of particles	[-]
N_a	amount of aggregates	[-]
P	pressure	[Pa]
Q	electric charge	[C]
r	radial distance between particle centers	[m]
R	radius	[m]
R_g	radius of gyration	[m]
S	surface area	[m^2]
s_{55}	compliance coefficient in shear mode	[m^2·N^{-1}]
s_p	area per grafted molecule	[m^2]
t	time	[s]
$\mathbf{t}$	tangential vector	[m]
T	temperature	[K],[°C]
u	velocity (general or in the x-direction)	[m·s^{-1}]
V	voltage	[V]
v	velocity in the y-direction	[m·s^{-1}]
w	velocity in the z-direction	[m·s^{-1}]
x	1st coordinate of a Cartesian system	[m]
$\mathbf{x}_z$	displacement field	[m]
x_z	displacement in the x-direction	[m]
X_f	real component of the fluid impedance	[kg·m^{-2}·s^{-1}]
X_i	in-phase input electric signal	[V]
y	2nd coordinate of a Cartesian system	[m]
y_z	displacement in the y-direction	[m]
Y_f	imaginary component of the fluid impedance	[kg·m^{-2}·s^{-1}]
Y_i	out-of-phase input electric signal	[V]
z	3rd coordinate of a Cartesian system	[m]
z_z	displacement in the z-direction	[m]
Z	electrical impedance	[Ω]
Z_f	fluid impedance	[kg·m^{-2}·s^{-1}]

Greek symbols

Symbol	Definition	Unit
α	dimensionless frequency	[-]
α_E	1st Euler angle	[rad]
β_E	2nd Euler angle	[rad]
γ	shear strain	[-]
γ_E	3rd Euler angle	[rad]
γ_w	complex wave propagation coefficient	$[\text{m}^{-2}]$
$\dot{\gamma}$	shear rate	$[\text{s}^{-1}]$
δ	phase angle	[°]
$\boldsymbol{\epsilon}$	strain tensor	[-]
$\dot{\boldsymbol{\epsilon}}$	rate of strain tensor	$[\text{s}^{-1}]$
ϵ_0	permittivity of free space	$[\text{C}\cdot\text{V}^{-1}\cdot\text{m}^{-1}]$
ϵ_r	relative permittivity	[-]
ζ	zetapotential of a surface	[V]
η	viscosity	[Pa·s]
η^*	complex viscosity	[Pa·s]
η'	in-phase component of the complex viscosity	[Pa·s]
η''	out-of-phase component of the complex viscosity	[Pa·s]
θ_{Ls}	measured phase shift	[°]
λ_s	wavelength	[m]
ν	Poisson's ratio	[-]
ξ	damping factor	$[\text{N}\cdot\text{s}\cdot\text{m}^{-1}]$
ρ	density	$[\text{kg}\cdot\text{m}^{-3}]$
ρ_v	electric charge density	$[\text{C}\cdot\text{m}^{-3}]$
σ	stress (often used for shear stress)	[Pa]
$\boldsymbol{\Sigma}$	stress tensor	[Pa]
τ_p	characteristic relaxation time	[s]
ϕ	volume fraction	[-]
Φ	interparticle potential	[J]
ω	angular velocity	$[\text{rad}\cdot\text{s}^{-1}]$

Subscripts

Symbol	Definition
0	zero-shear/frequency limiting
∞	high-frequency limiting
a	asperity
$char$	characteristic
co	contour
cp	capacitive
cr	critical
e	elastic
eff	effective
h	hydrodynamic
i	input
L	LockIn
m	medium or matrix
n	normal
o	output
p	particle
r	reduced
ref	reference
rel	relative
s	shear
v	viscous

Superscripts

Symbol	Definition
B	Brownian
g	gravitation
H	hydrodynamic
P	interparticle

Abbreviations

Symbol	Definition
A/D	analog-to-digital
AR	amplitude ratio
AFM	atomic force microscopy
DLS	dynamic light scattering
DP	degree of polymerisation
DQI	dispersion quality index
DWS	diffusing wave spectroscopy
HF	high-frequency
MEK	methyl ethyl ketone
MP	Multiphysics
PBD	polyisobutadiene
PDMS	polydimethylsiloxane
PHSA	polyhydroxystearic acid
PIB	polyisobutene
PIC255	piezoelectric material used for the shear stacks
PMMA	polymethyl methacrylate
PSR	piezo shear rheometer
PZT	lead zirconate titanate
Q-factor	quality factor
RC	resistor-capacitor
S	magnetic stirring
SEM	scanning electron microscopy
TTS	time-temperature superposition
UT	Ultra-Turrax
US	ultrasound

Contents

Abstract ix

Samenvatting xiii

List of symbols xvii

Contents xxiii

1 Introduction 1

1.1 Colloidal dispersions 1

1.2 Rheology 3

1.3 Motivation 8

1.4 Outline 8

2 High-frequency bulk rheometry 11

2.1 Introduction 12

2.2 Shear wave propagation 13

2.3 Techniques 14

2.3.1 Subresonant acoustic rheometers 15

2.3.2 Bulk resonators and immersed rheometers 20

2.3.3 High-frequency ultrasound rheometers 24

2.3.4 Cantilevers and resonating viscometers 27
2.4 Applications 28
2.4.1 Macromolecular solutions 29
2.4.2 Colloidal dispersions 29
2.4.3 Polymers and composites 30
2.5 Conclusions 30

3 Piezo shear rheometer **33**
3.1 Design of the piezo shear rheometer 34
3.1.1 Experimental setup 34
3.1.2 Simulations 36
3.2 Calibration and performance 43
3.2.1 Signal detection 43
3.2.2 Calibration 48
3.2.3 Performance and limits of the device 50
3.2.4 Gap loading effects 51
3.3 Validation 55
3.3.1 Overlap with a commercial device: viscous, viscoelastic and elastic samples 55
3.3.2 Comparison with TTS data 57
3.4 Conclusions 62

4 Stress contributions in colloidal suspensions **65**
4.1 Introduction 66
4.2 Experimental 67
4.2.1 Model systems 67
4.2.2 Rheological measurements 70
4.3 Results and discussion 70

4.3.1 Rheological behaviour of the model system 70
4.3.2 Comparison based on ϕ_{eff} 74
4.3.3 Method for rescaling the stresses 75
4.3.4 Analysis of the stress contributions 79
4.3.5 Shear thickening behaviour 86
4.4 Conclusions 90

5 Dispersion quality **91**
5.1 Introduction 92
5.2 Experimental 95
5.2.1 Preparation of silica dispersions 95
5.2.2 Rheological measurements 96
5.2.3 Monitoring a dispersion process 96
5.3 Results and discussion 97
5.3.1 Rheological behaviour of the model system 97
5.3.2 Frequency scaling 99
5.3.3 Derivation of a dispersion quality index 102
5.3.4 Monitoring a dispersion process 106
5.4 Conclusions 108

6 Conclusions and Outlook **111**

A Appendix **119**
A.1 Appendix to chapter 4 119
A.1.1 SEM Images 119
A.1.2 Calculation of the high-frequency elastic modulus 122
A.2 Appendix to chapter 5 124
A.2.1 'Gleissle' shift factor 124

A.2.2 Simulations of the Ultra-Turrax mixer 124

List of Figures **143**

List of Tables **147**

Curriculum Vitae **149**

List of publications **151**

Chapter 1

Introduction

The title of this dissertation hints at the importance of two major components throughout the work: 'high-frequency rheometry' and 'colloidal dispersions'. In fact, the relationship between these components forms the basis and motivation for this thesis. This chapter serves to introduce both concepts, and paves the way for the topics that are discussed further on.

1.1 Colloidal dispersions

Dispersions are two-component systems in which discrete constituents are dispersed in a continuous phase. The term 'colloid' refers to the dispersed phase and generally corresponds to a size range between $\sim$ nm and $\sim \mu$m. A pragmatic definition of colloidal particles is that the surface properties of such a particle dominate the bulk ones. Colloid science dates back to the 19th century, when Robert Brown discovered that small particles dispersed in a fluid undergo random motion. This phenomenon was defined later as 'Brownian' motion. The colloidal state and properties were delineated by Thomas Graham, who is often considered as the founder of modern colloid science [1].

Colloidal dispersions are ubiquitous both in natural and industrial environments. Natural examples for instance include blood, milk, or even smoke, in which small solid particles are dispersed in air. An early synthetic example was the use of carbon black for creating inks in ancient Egypt and China [2, 3]. At present, colloidal dispersions can be found in many everyday applications such as paints, food products, cosmetics, or composite materials. Furthermore,

model dispersions have important scientific value and are often employed to test theories for molecular or nano materials. Specifically, colloidal suspensions denote dispersions that consist of solid particles dispersed in a liquid medium. In this thesis, the term 'colloidal dispersion' is used interchangeably with 'colloidal suspension', and is used mainly when indicating the dispersed nature of the particles.

Although the colloidal range is often defined by the size of the constituents, a better definition of the upper limit stems from a definition of the body forces that act on the dispersed particles. The energy scale in a colloidal system is set by the thermal energy k_BT, with k_B Boltzmann's constant and T the temperature. Typical values of the thermal energy are small, with $k_BT \approx 4 \cdot 10^{-21}$ J at environmental temperature, but define the characteristic energy and stress in the system. For instance, the random motion that occurs as a result of this energy is responsible for an osmotic pressure. Thermal collisions between molecules of the medium and suspended particles also induce a Brownian force F^B on the particles:

$$F^B = \frac{k_BT}{a}, \tag{1.1}$$

which scales inversely with the particle radius a. Furthermore, the suspended particles are subjected to gravity, leaving to a gravitational force F^g:

$$F^g = (\rho_p - \rho_m)\frac{4}{3}\pi a^3 g. \tag{1.2}$$

ρ_p and ρ_m are the particle and fluid density, respectively, while g is the gravitational constant. The colloidal range is defined by the values of particle sizes for which Brownian contributions are equal to or larger than gravitation.

The thermal motion of particles dispersed in a medium inherently causes a hydrodynamic drag on the particle surfaces. For the simplest case of a single colloidal particle moving through a fluid at a velocity u, and at laminar conditions, the resulting hydrodynamic force F^H is given by

$$F^H = 6\pi\eta_m a \cdot u. \tag{1.3}$$

The hydrodynamic force scales with the medium viscosity η_m and slows down the thermal motion. The relationship between the particle displacement and hydrodynamic drag is given by the well-known single-particle diffusivity $\mathcal{D}_0$ [4–6]:

$$\mathcal{D}_0 = \frac{k_BT}{6\pi\eta_m a}, \tag{1.4}$$

and sets the characteristic time scale in a dilute suspension: *i.e.* the time that is required for a particle to relax or diffuse a distance equal to its own size. This

relationship becomes more complex for non-dilute conditions due to multi-body effects. Furthermore, at higher concentrations, the relative motion between particles in close proximity can cause strong hydrodynamic lubrication stresses.

Particles in dispersion can interact through an entire range of interaction forces. Due to the colloidal nature of the particles, these interactions play a prominent role in colloidal suspensions. For instance, dispersion forces are inherently attractive and arise as a result of the polarisation of electron clouds induced by neighbouring atoms. They are omnipresent and will inevitably lead to aggregation of the particles if no stabilisation is foreseen. Stability can be imparted by tuning the surface characteristics of the particles. The presence of charges on the colloid surfaces creates an electrostatic repulsion between the suspended particles, while a polymeric stabilisation layer grafted on the surface induces steric repulsion and prevents particles to come into close contact. An additional type of interaction arises in the presence of soluble polymers in the dispersion. They give rise to depletion forces, which result from an osmotic pressure due to the depletion of the additives in the thin layer between particles, and can for instance act to push particles together.

Colloidal interactions influence the properties of colloidal suspensions in two ways. They determine the particle interaction forces, and hence directly affect the total stresses in a dispersion. The interaction force $F(r)$ is typically expressed via an interparticle potential as:

$$F(r) = -\frac{d\Phi(r)}{dr}. \tag{1.5}$$

The interparticle potential $\Phi(r)$ varies with r, the radial distance between two particle centres, depending on the type and strength of interaction. In addition, colloidal interactions alter the microstructure of the suspension and colloidal systems can typically show a rich phase behaviour. For instance, figure 1.1 shows that for a charge-stabilised suspension, depending on the extent of the repulsive interaction, the dispersion can either reach a crystalline, fluid-like or flocculated state.

1.2 Rheology

The term ‘rheology’ literally means ‘the study of flow’. In fact, the field of rheology aims at characterising the behaviour of materials in response to a deformation or flow. It has been applied extensively to investigate various complex material classes, ranging from polymers to solutions, gels or dispersed systems [7]. Rheology is particularly useful to study colloidal suspensions for two important reasons. First of all, colloidal suspensions are present in

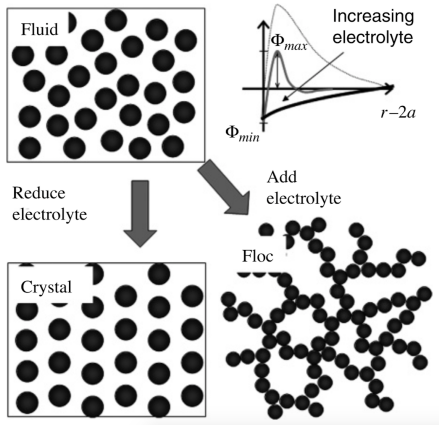

Figure 1.1: Illustration of the effect of the interparticle interactions on the microstructure of a charge-stabilised colloidal suspension. Electrolytes screen the electrostatic interactions. Reducing the electrolyte concentration induces crystallisation, while increasing the amount of electrolyte can lead to flocculation (from Mewis and Wagner [3]).

.

many technological applications and understanding the behaviour under specific flow conditions is crucial for successful product and process design. Secondly, the rheological response is highly sensitive to the microstructure of and the interactions that play inside the suspension. Furthermore, rheology allows to investigate suspensions at various particle concentrations, and can hence directly probe the microstructure at relevant conditions.

In order to derive material properties, it is crucial to operate under well-defined kinematic conditions in a rheometrical measurement. One such type of deformation that is commonly used is an ideal shear flow. The concept is illustrated in figure 1.2. The top plate moves at a velocity u_0 while the bottom plate is kept stationary. In the absence of slip or non-idealities in the flow behaviour, the velocity profile varies linearly over the gap H and results in a constant velocity gradient or shear rate $\dot{\gamma} = \frac{du}{dy} = cte$. A material placed in between both plates will resist the applied flow. In case of a Newtonian fluid, the resulting shear stress equals:

$$\sigma_{xy} = \eta \cdot \frac{du}{dy} = \eta \cdot \dot{\gamma} \tag{1.6}$$

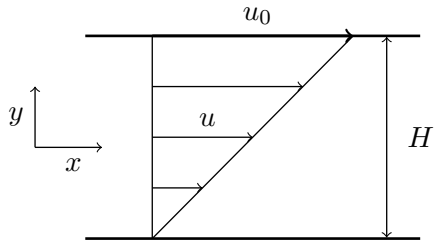

Figure 1.2: Schematic of a simple shear flow. The upper plate moves at a velocity u_0 in the x-direction while the lower plate is stationary. H represents the gap.

and scales with the fluid viscosity η. When a Hookean solid is placed in between both plates, the shear stress varies with the applied deformation $x_{z,0}$

$$\sigma_{xy} = G \cdot \frac{x_{z,0}}{H} = G \cdot \gamma \tag{1.7}$$

via the shear modulus G of the material. Hence, by monitoring the opposing shear stress exerted on the plates, the material properties can be derived. Note that for rheological applications considering pure shear flow, the tensorial notation of the stress is often abandoned and the shear component is simply written as σ. In colloidal suspensions, Brownian, hydrodynamic and colloidal interactions give rise to both elastic and viscous stress components, and more elaborate analysis methods are required to identify the different contributions.

Frequency domain

Small amplitude oscillatory shear measurements are very useful to study the viscoelastic properties of complex materials [8]. Practically, they exist in the application of a continuously varying sinusoidal shear deformation:

$$\gamma(t) = \frac{x_{z,0}}{H} \cdot \sin(2\pi f t) = \gamma_0 \cdot \sin(2\pi f t), \tag{1.8}$$

with f the applied frequency. The strain amplitude γ_0 is kept small to probe the material at its near-equilibrium state, and allows to probe the suspension without disrupting the microstructure. Evidently, the critical amplitude for which this assumption remains valid is material dependent and is, in case of colloidal suspensions, strongly influenced by the interparticle interactions that are present. Due to the sinusoidal nature of the deformation, the shear rate varies as:

$$\dot{\gamma}(t) = \gamma_0 2\pi f \cdot \cos(2\pi f t). \tag{1.9}$$

As shown in figure 1.3, continuously varying the shear strain and rate allows to directly probe the elastic and viscous stress contributions. Elastic contributions

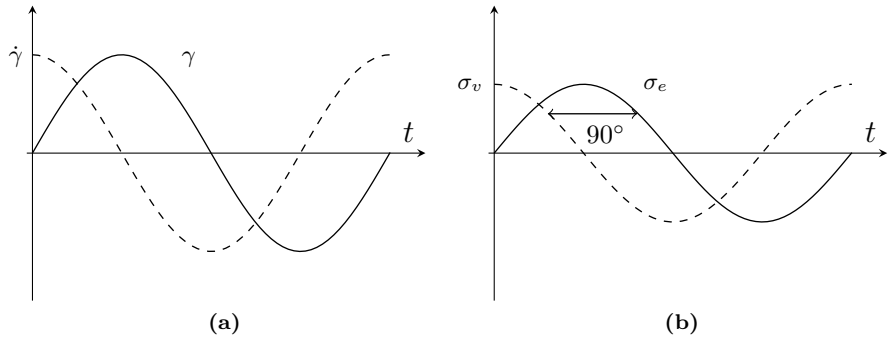

Figure 1.3: Illustration of an oscillatory shear flow experiment. (a) Sinusoidal shear displacement and shear rate. (b) Resulting elastic and viscous stresses.

are in-phase with the deformation, while viscous contributions are 90° out-of-phase. Viscoelastic materials hence display a phase angle δ that lies in between 0 and 90°. When using a complex notation for the in- and out-of-phase stresses, the stress can be decomposed in a real and imaginary part:

$$\sigma = (G' + jG'') \cdot \gamma = G^* \gamma. \tag{1.10}$$

G' and G'' are the elastic (or storage) and viscous (or loss) moduli, and represent measurement-independent material properties. Similarly, the stresses can be written in terms of complex viscosities as:

$$\sigma = (\eta' - j\eta'') \cdot \dot{\gamma} = \eta^* \dot{\gamma}, \tag{1.11}$$

with $\eta' = G''/(2\pi f)$. Monitoring the continuously varying stress signal enables detection of the complex modulus G^* and phase angle δ, and hence the in- and out-of-phase stress contributions.

A particularly useful feature of oscillatory measurements is that, by varying the frequency f, the time scale under investigation can be changed. This proves to be very relevant since for colloidal dispersions, and for complex fluids in general, the behaviour changes depending on the time scale that is probed. A recognisable example is 'Silly Putty', a silicone based polymer, which acts as a solid when deformed abruptly but readily flows at longer times [9]. By varying the frequency, it is possible to obtain an integrated picture of the rheological behaviour.

Time domain

Similarly, material properties can be derived via the response to a rotational shear deformation. For instance, from the time-dependent stress response to a step strain experiment executed within the linearity limits of the material, a relaxation modulus $G(t)$ can be derived:

$$G(t) = \frac{\sigma(t)}{\gamma_0}, \tag{1.12}$$

which is related to the frequency dependent complex modulus G^*. In addition, increasing the applied shear rate or stress allows to study the behaviour of suspensions outside of their equilibrium conformation. Hydrodynamic stresses increase at increasing flow rates; they alter the balance between the different interaction forces and disrupt the microstructure. For instance, a reorganisation of the microstructure is often seen which reduces the resistance against flow and causes the well-known 'shear thinning' behaviour. At even higher rates, large stresses that occur between particles being pushed together can lead to an increase in the viscosity again. In addition, significant stress contributions other than the pure shear component can arise. Understanding the nature of these rheological phenomena and their relationship with the microstructure is key for controlling the behaviour and performance of colloidal dispersions.

Continuum approximations in dispersed systems

In rheometrical measurements, it is assumed that the velocity profile varies linearly over the gap and that the material acts as a continuum. Important to realise is that for colloidal dispersions, which contain discrete constituents distributed in a medium, this is theoretically not the case. Nonetheless, the basic rheological concepts are used for dispersion rheology as well, and a so called 'pseudo-continuum' approach is adopted. This has important consequences. In case of suspensions, the fillers are solid and non-deformable. Hence, the deformation that is applied is only taken up by the medium, meaning that local shear rates and stresses are higher than the average values measured by an instrument. This is critical for instance for dispersions in viscoelastic fluids [10]. Another consequence relates to the length scales in the system. In order to derive relevant macroscopic properties, the dimensions of the measured sample should be much larger than the characteristic dimensions of the building blocks of the dispersion and their resulting microstructure.

1.3 Motivation

This thesis focuses on the potential role of rheology in determining local scale parameters of the colloidal building blocks in a suspension. Rheology is highly sensitive to the microstructure, and allows to directly probe suspensions at relevant filler volume fractions. However, the rheological response offers macroscopic properties, and relating these properties to local scale parameters is more challenging. Frequency-dependent rheological measurements can be used to obtain information on different time and length scales. In this work, it is suggested to use the high-frequency (HF) response for deriving such local parameters.

In absolute terms, the expression 'high-frequency' is rather meaningless. In the framework of colloidal suspensions, it is related to the characteristic time scale of the dispersion itself. For a dilute colloidal suspension of hard spheres, this scale simply relates to the diffusional time scale in the suspension (equation 1.4), which occurs at a characteristic frequency f_{char}:

$$f_{char} = \frac{k_B T}{a^3 12\pi^2 \eta_m}. \tag{1.13}$$

f_{char} also sets a characteristic length scale, since it relates to the frequency at which a particle is able to diffusive a distance equal to its own size. This diffusional boundary layer decreases with frequency, and in order to probe stresses at shorter length scales near the surfaces of the colloidal building blocks, the applied frequency must be much larger than f_{char}. From equation 1.13, it can be seen that the frequency range of interest depends on the properties of the suspension. For instance, for a dispersion of hard spheres of 50 nm radius dispersed in a Newtonian matrix of 0.1 Pa·s, frequencies must be larger than 10 Hz. Such ranges are typically above the accessible frequency limit of standard rotational rheometers, and we must therefore turn ourselves to non-conventional methods for studying the high-frequency response.

1.4 Outline

Not unlike a colloidal dispersion, this thesis is a two-component system. The first main part of the manuscript considers high-frequency rheometry. The second part focuses on the application envisaged here: a high-frequency rheological study of colloidal suspensions.

Chapter 2 describes the state of the art of high-frequency bulk rheometry. The discussion mainly concentrates on a review of different instruments based on

their mode of operation and the resulting operating window. The measurement ranges of different types of techniques are compared. The chapter ends with a discussion of a few material classes for which the use of high-frequency rheometry has proven particularly valuable and suggests some areas of interest. Chapter 3 considers the design and analysis of a homebuilt piezo shear rheometer. The design was optimised for studying colloidal suspensions at frequencies that directly extend the accessible range of conventional methods. The calibration and validation of the instrument are discussed together with the different limitations.

Chapters 4 and 5 summarise the results of high-frequency rheological measurements on colloidal suspensions. Chapter 4 focuses on the role of the particle surface topology on the local stresses that arise near its surfaces. Colloids with different topologies are studied, ranging from particles with a grafted polymer layer to roughened particles. While chapter 4 considers stabilised and well-dispersed particles, chapter 5 concentrates on attractive, partially aggregated suspensions. The use of high-frequency rheology for determining the local structure of the colloidal building blocks is investigated. These building blocks can be dispersed particles or aggregates, and a measure for the degree of dispersion is derived.

Ultimately, chapter 6 finalises this work with general conclusions on high-frequency rheometry and its role in determining local scale parameters in suspensions. The outlook presents routes for further research and includes opportunities both towards rheometer design as well as experimental studies and applications.

Chapter 2

High-frequency bulk rheometry

High-frequency rheometry is a form of mechanical spectroscopy which probes the local microstructure and dynamics of complex materials. Although the exact frequency range of interest is material dependent, applications often require frequencies larger than those accessible by conventional rotational devices. This chapter presents an overview of different high-frequency bulk rheometrical techniques, *i.e.* rheometers that can operate at acoustic (20 Hz − 20 kHz) or ultrasound (> 20 kHz) frequencies. As with all rheometers, precise control or at least know-how is of prime importance. Hence, one of the key design parameters stems from the inherent effects of wave propagation that occur in oscillatory measurements. These effects are particularly important at elevated frequencies and are discussed first. Different high-frequency techniques are classified based on their mode of operation within the propagation limits and are reviewed subsequently. A comparative overview of the different types of techniques in terms of their measurement ranges is provided. The chapter ends with a discussion of a few material classes for which the use of high-frequency rheometry has proven particularly valuable.

The following chapter is written in the format of a manuscript to be submitted:

> B. Schroyen, P. Van Puyvelde, J. Vermant. High-frequency bulk rheometry.

B. Schroyen executed the literature survey and wrote the manuscript.

2.1 Introduction

Small amplitude oscillatory measurements probe the equilibrium structure of a material and deliver its rheological fingerprint in the frequency domain. Changing the frequency also infers a variation in the time or length scale that is investigated. Low-frequency moduli depend on slow processes which are typically collective properties whereas measurements at high frequencies allow to zoom in into the microstructure and to reveal information on the local dynamics. For instance, high-frequency rheology has been used to determine interaction strengths and local structural information in colloidal dispersions [11, 12] or to identify fast relaxation processes in polymers [13]. In fact, in order to obtain an integrated picture of many complex fluids, oscillatory measurements over an extended frequency range are required. The exact location of the "high-frequency region" on an absolute frequency scale depends on the characteristic time scales of the material under investigation and can vary over several decades [14]. As an illustration for the case of colloidal dispersions, the high-frequency region is typically reached above 1 kHz.

Conventional rotational rheometers typically operate at frequencies below $10 - 100$ Hz. Their low-frequency limit is set by the patience of the operator and, for many practical applications, the low-torque limit. At high frequencies inertial effects come into play; they scale with frequency $\propto f^2$ and will eventually dominate the response. The exact limit depends on the properties of the measurement system and sample. For rheologically simple materials with relaxation times governed by the same physical mechanism, time-temperature superposition can be applied to access higher frequencies [15]. However, for many complex materials, this principle does not hold and the high-frequency region has to be reached physically by means of different measurement instruments. A vast array of techniques has been developed since the middle of the previous century, owing to the large interest in rheological properties at elevated frequencies both for practical and fundamental purposes. This review aims at summarising rheometrical techniques for high-frequency rheology. We focus mainly on techniques that directly probe bulk material properties. Microrheological techniques, *e.g.* using light scattering or tweezers, have been developed and successfully applied as well [14]. However, they require the extrapolation of bulk properties from measurement values, which can be an issue for instance for heterogeneous systems. For an extensive review on microrheology, the reader is redirected to Furst and Squires [16].

High-frequency rheometrical techniques span a range between $0.1 - 10^8$ Hz, starting from methods that directly extend the accessible frequencies of conventional rotational rheometers until setups operating in the MHz range, near fluid inertia and continuity limits. Wave propagation effects are discussed

first; these play an important role when extending to higher frequencies over such a large span and impose important design limitations. Different techniques are organised and discussed based on their mode of operation and location within the propagation limits. The review concludes with a few practical applications that illustrate the value of high-frequency rheometry for different complex material classes.

2.2 Shear wave propagation

Similar to commercial rotational devices, high-frequency rheometers probe material properties by means of mechanically induced oscillations. The sample's response can be determined either from the moving surface or from a second, stationary surface. Oscillatory displacements in a bulk fluid lead to the creation of waves, either longitudinal or transverse in nature depending on the direction of motion relative to the orientation of the surface, which propagate through the sample. For instance, an oscillatory in-plane movement of a surface with velocity $u(t) = u_0 \cdot e^{j2\pi ft}$ induces a shear wave [17,18]. The velocity profile in the normal (z) direction can be obtained by solving the Navier-Stokes equations [19], as follows:

$$u(z,t) = \left[A_1 e^{j\gamma_w z} + A_2 e^{-j\gamma_w z}\right] \cdot e^{j2\pi ft}. \tag{2.1}$$

$\gamma_w^2 = \frac{-j(2\pi f)^2 \rho}{|G^*|}$ is the complex wave propagation coefficient and depends on the fluid properties, *i.e.* the density ρ and amplitude of the complex modulus $|G^*|$. Constants A_1 and A_2 depend on the boundary conditions of the system. The wave equation (equation 2.1) illustrates that propagation effects inherently influence the signal detection, since both amplitude and phase vary along the direction of propagation. Furthermore, the wave created at the surface of the excitation unit is gradually attenuated with increasing distance due to the dissipation of energy. This is depicted schematically in figure 2.1. For operating purposes two limiting cases can be identified. In the gap loading limit, the wave travels through a fluid that is confined between two surfaces and is not attenuated over the propagation distance. Conversely, in the surface loading limit, the wave is completely damped inside the fluid. Rheological measurements are mostly performed within either of these two limits. Schrag [20] determined the effect of wave propagation on shear rheological measurements when deviating from these limits, *i.e.*, when the measurement gap H is similar in magnitude compared to the wavelength λ_s:

$$\lambda_s = \frac{1}{f\sqrt{\frac{\rho}{|G^*|}}\cos(\frac{\delta}{2})}. \tag{2.2}$$

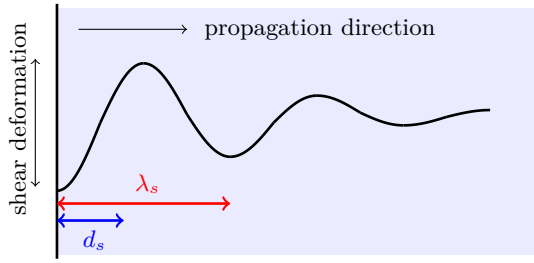

Figure 2.1: Schematic of a shear wave propagating from a surface. The wave is gradually attenuated in the propagation direction; λ_s is the wavelength and d_s the penetration depth.

Both the wavelength λ_s and penetration depth d_s, given by

$$d_s = \frac{1}{2\pi f \sqrt{\frac{\rho}{|G^*|}} \sin(\frac{\delta}{2})}, \tag{2.3}$$

generally decrease with increasing frequency depending on the fluid properties [17]. The penetration depth decreases with increasing phase angle δ due to enhanced damping, which is in contrast with the wavelength. Figure 2.1 for instance sketches the relationship between λ_s and d_s for $\delta = 45°$. Both variables are important design factors that need to be taken into account. Wave propagation effects also limit the type of materials or microstructures that can be studied, in particular at high frequencies, since the penetration depth defines the maximal distance over which the sample is probed.

2.3 Techniques

Figure 2.2 shows an overview and the accessible frequency ranges of the different types of techniques that will be discussed. The techniques are allocated based on their mode of operation within the wave propagation limits discussed before. Subresonant rheometers, with an accessible frequency range < 10 kHz, attempt at operating within the gap loading limit given. In the kHz region the wavelength decreases below 1 mm for many fluids (equation 2.2, depending on the exact sample properties) and gap loading operation is impossible except for very small gaps. Rheometers operating at or near resonance frequencies in the kHz range hence mostly function within the surface loading limit. At high ultrasonic frequencies > 1 MHz, the penetration depth becomes so small that surface properties rather than bulk properties are probed (equation 2.3). Cantilevers are discussed separately; so far it has proven challenging to accurately

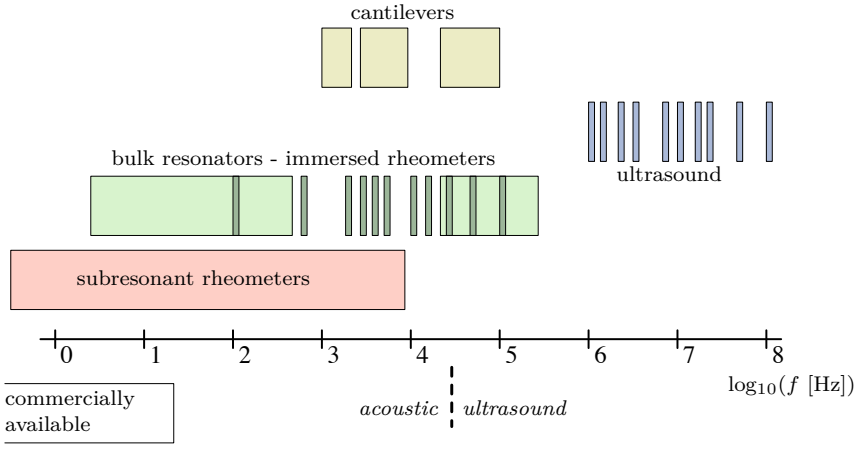

Figure 2.2: High-frequency rheometrical techniques compared based on their accessible frequency ranges. Conventional rotational rheometers are given as a reference. The transition between the acoustic (20 Hz - 20 kHz) and the ultrasound (> 20 kHz) range is indicated as well.

extract rheological properties and related setups have mainly been used as viscosity sensors. The working principles of the different types of high-frequency techniques are discussed below. Table 2.1 provides a comparative overview of their operating limits.

2.3.1 Subresonant acoustic rheometers

Subresonant acoustic rheometers can be used to determine complex fluid properties at frequencies that directly extend the accessible frequency range of commercial rotational devices (figure 2.2). The majority of such techniques makes use of piezotechnology. Their measurement principle is similar to those of conventional rheometers, *i.e.* the material is confined in between 2 parallel surfaces and operation in the gap loading limit is generally assumed. However, excitation of the signal is carried out by small piezoelectric elements instead of a heavy motor which drastically reduces the inertia of the measurement system. The upper limit in frequency range is given by mechanical resonances of the system, and postponing or suppressing such resonances is an important design criterion. Below, different methods are discussed and compared based on their method of deformation and resulting flow field.

Table 2.1: Comparison of accessible ranges (min - max) in frequency, temperature, complex viscosity/modulus, strain amplitude and required sample volume for different techniques. The table is divided in subresonant rheometers (1), bulk resonators and immersed rheometers (2), ultrasound rheometers (3) and cantilevers (4). Note that typical values are given based on what is available in literature; they represent the accessible ranges for a certain type of technique rather than a specific device. Question marks indicate values that are taken from typical measurement ranges when actual device specifications were not stated.

	f [Hz]	T [°C]	$\lvert\eta^*\rvert$ [Pa·s]	$\lvert G^*\rvert$ [Pa]	γ [%]	Vol [ml]
(1) Piezo linear shear (monolithic) [21–24]	$0.1 - 5 \cdot 10^3$	$25 - 150$	–	$> 10^2$	≤ 0.01	≤ 0.1
(1) Piezo linear shear (stack) [25, 26]	$0.1 - 2 \cdot 10^3$	$10 - 50$	> 0.05	$5 - 10^9$	< 0.1	≤ 0.1
(1) Piezo rotation [27]	$0.5 - 2 \cdot 10^3$	$-100 - 300$	–	$> 10^2$	≤ 0.1	~ 0.1
(1) Piezo squeeze [28–30]	$1 - 4 \cdot 10^3$	$10 - 60$ (?)	$10^{-3} - 2$	$0.1 - 10^4$	≤ 0.1	~ 0.1
(1) Electromagn. torsional [31]	$10^{-6} - 10^4$	$2 - 60$ (?)	–	$10^4 - 10^9$	< 0.01	–
(1) Electromagn. linear shear [32]	$10 - 10^4$	–	> 100	–	< 20	–
(1) Thermal linear shear [33]	$0.5 - 5 \cdot 10^2$	–	$1 - 100$	$50 - 10^4$	–	$\leq 5 \cdot 10^{-6}$
(2) Piezo torsional [11, 34–36]	$10^3 - 10^5$	$10 - 35$	$5 \cdot 10^{-4} - 0.5$	$10 - 10^5$	≤ 1	≥ 10
(2) Electromagn. tors. $(f_r, \Delta f)$ [37–41]	$10^2 - 2 \cdot 10^4$	$20 - 25$ (?)	$5 \cdot 10^{-4} - 0.06$	–	≥ 1	≥ 15
(2) Electromagn. tors. (f_r, ω_{max}) [42, 43]	$2 - 5 \cdot 10^2$	$20 - 25$ (?)	$10^{-3} - 2$	–	–	~ 20
(2) Torsional guided waves [44–47]	$2 \cdot 10^4 - 3 \cdot 10^5$	$5 - 85$	$10^{-3} - 10$	–	–	~ 0.1
(2) Planar shear [48]	$6 \cdot 10^2$	–	$5 \cdot 10^{-3} - 0.5$	–	–	~ 0.1
(2) Wire vibrometer [49–51]	$\sim 10^3$	$5 - 60$	$3 \cdot 10^{-3} - 0.1$	$5 - 10^3$	–	~ 60
(3) Thickness shear [52–54]	$10^6 - 10^8$	$10 - 60$	$> 10^{-4}$	$10^4 - 10^9$ (?)	≤ 0.1	≤ 0.1
(3) Thickness shear (high temperat.) [55]	$5 \cdot 10^4 - 10^8$	$-150 - 300$	$> 10^{-2}$	$10^6 - 10^9$ (?)	≤ 0.1	≤ 0.1
(3) Reflectometry [56–59]	$5 \cdot 10^6 - 5 \cdot 10^7$	$15 - 85$	–	$10^5 - 10^9$	–	≤ 0.5 (?)
(4) Cantilevers [60–62]	$10^3 - 10^5$	$5 - 40$	$10^{-3} - 2$	$10 - 10^5$	–	≤ 0.05

Piezo shear rheometers

Piezo shear rheometers make use of transverse waves propagating through the sample (equation 2.1). A first design, introduced by Cagnon and Durand [21] and shown in figure 2.3 (a), contained 2 sets of piezoceramic shear elements attached to glass substrate surfaces. Excitation elements, driven by an AC voltage, create a linear shear deformation, while the elements on the opposite side were used for detection. The design was both simple and robust and facilitated a large operating range in terms of frequency (table 2.1). Extensions were made to the original design, incorporating optical paths for microscopy and light scattering studies or combining a magneto-rheological setup [22–24]. In order to ensure gap loading operation, measurement gaps are typically small (order $\sim 100\,\mu$m) and require accurate alignment. Roth et al. [25] implemented piezoelectric shear stacks (figure 2.3 (b)), which improve the sensitivity and reduce both electric cross-talk and parasitic displacements but are less temperature resistant (table 2.1). Calibration is relatively simple for linear shear rheometers with decoupled excitation and detection units. Without important electromechanical contributions from the system, fluid properties can be derived in a straightforward manner by comparing the excitation (V_o) and detected (V_i) signals:

$$\left|\frac{F}{x_z}\right|_s = A_p \cdot \frac{V_i}{V_o}. \tag{2.4}$$

$\left|F/x_z\right|_s = |AR|_s$ is the shear amplitude ratio, while A_p represents a system constant. Both the complex modulus and phase angle can be derived easily from the detected signal. Furthermore, measurements can be carried out at small strain amplitudes and required sample volumes are small (table 2.1). Surface tension effects can be an issue for smaller volumes, in particular for fluids with low bulk viscosities. The resolution in measurable viscosity/modulus is limited by the accurate detection of the output signal, while the upper limit is set by the mechanical compliance - or deformability - of the piezoelements or -stacks and is typically high.

A different type of design was developed by Kirschenmann and Pechhold [27] and is shown in figure 2.3 (c). The setup consists of a piezo-wheel with 6 spokes; driving elements are attached to 3 spokes and create a rotational shear deformation, while elements on the other spokes are used for detection. The coupling of the excitation and detection reduces the sensitivity and complicates the analysis: fluid properties need to be determined by subtracting the response of the empty cell from the measured complex torque. Furthermore, the complete measurement system was relatively heavy, leading to an increase in inertia. However, important advantages are the rotational symmetry and the possibility

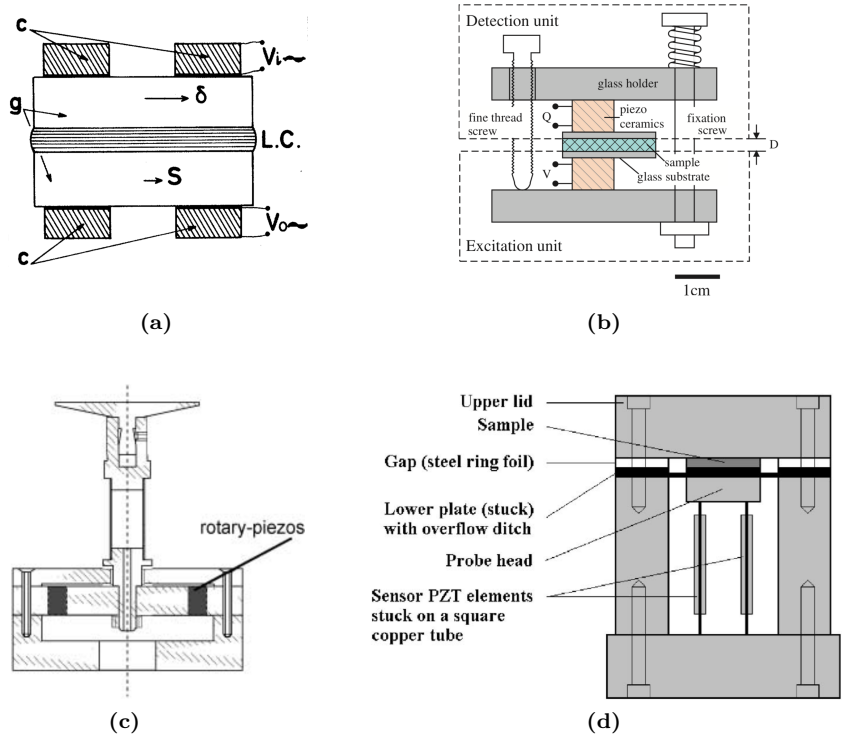

Figure 2.3: Overview of different subresonant piezo rheometers: linear shear rheometers with (a) monolithic shear elements [21] or (b) shear stacks [25], (c) rotational shear flow [27] and (d) squeeze flow rheometers [30].

for decoupling the substrate from the piezoelements, hence facilitating the temperature control (table 2.1).

Piezo squeeze flow rheometers

Pressure wave or oscillatory squeeze flow rheometers make use of longitudinal waves to determine complex fluid properties. Early designs consisted of a sample confined in between two substrates that are attached to piezoelectric elements, similar to initial linear shear flow setups (figure 2.3 (a)) [28, 29]. General advantages are their simplicity in design and construction and the high temperature resistance of longitudinal piezoelements [63]. The main disadvantage on the other hand is the more complex flow field that arises.

The compressional deformation induces a Poiseuille flow that moves radially outwards through the slit. Although such pressure driven flows have been used extensively to determine rheological properties [8], important assumptions have to be made here to derive linear viscoelastic moduli based on the applied compression. In case of an axisymmetric cell operated within the lubrication approximation (gap $H \ll$ substrate radius R) and in the absence of inertia, slip, surface tension or compressibility effects, the complex modulus can be derived via the measured normal amplitude ratio (equation 2.4):

$$|G^*| = \frac{2}{3\pi}\frac{H^3}{R^4} \cdot |AR|_n \,. \tag{2.5}$$

The applied compression amplifies the force detection compared to shear [29], and hence increases the sensitivity drastically but reduces the upper limit for the amplitude ratio (table 2.1) which is set by the system's compliance. First order correction factors for inertia and slip coefficients have been derived as well [13, 63–65]. Pechhold et al. [66] developed a squeeze flow setup with excitation and detection elements positioned at the bottom (figure 2.3 (d)) [30]. Both the linear viscoelastic moduli and compressibility could be determined by measuring at different gap heights. The setup was eventually combined with a rotational piezo rheometer (figure 2.3 (c)) for simultaneous shear and squeeze flow measurements [67]. Sánchez et al. [68] designed and empirically modelled a mini squeeze flow setup with decoupled excitation and detection elements for measurements on highly viscous samples with volumes $< 10\,\mu$l. However, only the complex viscosity was reported and displayed considerable scattering.

Other shear rheometers

Shear rheometers with different methods of excitation/detection have been developed as well. For instance, Chen and Lakes [31] performed broadband measurements on viscoelastic solids by means of an electromagnetically driven torsional apparatus. Effects of resonances were reduced by decoupling the detection of the displacement via interferometry and by numerically correcting for the resonance behaviour. The accessible frequency range could be enlarged for materials with very small phase angles by analysing the resonance frequency shift (table 2.1). Recently, Koganezawa et al. [69] developed an electromagnetically driven planar shear setup for the characterisation of viscoelastic fluids. The displacement is detected with a laser Doppler vibrometer. A first attempt was made at modelling the first resonance modes of the setup to extend the measurable frequency range ≥ 10 kHz, but needs refinement. Verbaan et al. [32] suggested a more direct approach for extending the upper limit of subresonant techniques by introducing a high-viscous damper into the design. In addition, double-leaf springs were implemented to guide the deformation of the sliding

plate rheometer and prevent out-of-plane displacements. The damper effectively alters the behaviour around the resonance frequency, but adaptations to the setup are required to improve the sensitivity for fluids with lower viscosities (table 2.1).

Recent years have seen a growing interest for fluid characterisation using only small sample volumes or in confined environments. Christopher et al. [33] designed a MEMS based nanopositioner stage for in-plane oscillations. The sample is confined at gaps $< 20\,\mu$m, which reduces the required sample volume but requires sensitive alignment. Excitation of the oscillation is carried out by a thermal actuator, similar to cantilever designs, which is connected to the stage via parallel dual lever nanopositioners. Detection of the displacement is performed optically. The setup was able to probe viscoelastic material properties in a qualitative manner, but design improvements are required. Nonetheless, while several MEMS based viscosity probes have been developed recently, the setup developed by Christopher et al. [33] is the only subresonant shear probe able to measure both amplitude and phase.

Gap loading limitations

The assumption of operation in the gap loading limit constrains the maximum measurement gap H that may be applied at a given frequency. The gap H must be much smaller than the shear wavelength λ_s, which is a decreasing function of frequency with a magnitude depending on the sample properties (equation 2.2). In the frequency range accessible by subresonant rheometers, this mainly presents an issue for materials with smaller moduli or low complex viscosities. Decreasing the gap drastically increases the accessible viscosity range. The attenuation of the propagating wave depends on the density and viscoelastic properties of the fluid under investigation. Schrag [20] derived analytical expressions based on the wave equation (equation 2.1) for correcting the measured viscoelastic properties when operating outside the gap loading limit. Although not often applied, such correction factors are essential to extract the correct physical response.

2.3.2 Bulk resonators and immersed rheometers

A second main category involves techniques that operate at somewhat higher frequencies in the acoustic or low ultrasonic range (figure 2.2). Besides a few exceptions, setups in this range make use of resonating structures that undergo well-defined deformations. Their measurement principle is based on the influence of a sample on the resonance behaviour. Accessible frequencies of a specific

setup hence depend on the exact resonance modes. Because of the reduced wavelength at kHz frequencies, operation in the surface loading limit is mostly assumed, so that the distance between the resonating structure and stationary wall or sample surface must be large (equation 2.2). The penetration depth d_s is still sufficiently large so that bulk properties are probed (equation 2.3). Similar to the previously discussed subresonant rheometers, different resonators with various deformation modes have been developed.

Torsional shear rheometers

Torsional resonators consist of cylindrical elements that are immersed and undergo a purely torsional deformation. The motion creates a propagating shear wave that is fully attenuated in the sample. The deformation profile of the shear wave is well-described and rheological properties can readily be derived, but are coupled with inertial effects. Resonance modes can either be driven piezoelectrically, magnetostrictively or electromagnetically.

Piezoelectric resonators were introduced first by Mason [34] and are generally driven by a torsional mode quartz crystal, resonating at one or more discrete frequencies depending on the dimensions of the structure. The resonance modes are very temperature-dependent and precise temperature control is crucial. Figure 2.4 (a) shows a schematic of a piezoelectrically driven torsional resonator and sketches the penetration of the torsional wave into the sample [11]. In order to derive both amplitude and phase of a complex fluid, two independent measures of the sample's influence are used: the shift in resonance frequency f_r and a damping factor. The latter is generally derived via the broadening of the resonance curve Δf [11, 35]. The Q-factor ($Q = f_r/\Delta f$) quantifies the extent of damping and needs to be large ($\gg 1/2$) for sufficient measurement accuracy. In case of piezoelectrically driven resonators, excitation of the oscillation and detection are straightforward. The fluid impedance $Z_f = X_f + jY_f$, or its complex resistance against flow, depends on the measured properties via:

$$X_f = A_1 \cdot (\Delta f - \Delta f_{air}), \tag{2.6}$$

$$Y_f = A_2 \cdot (f_r - f_{r,air}), \tag{2.7}$$

and can be related to the linear viscoelastic moduli:

$$G' = \frac{X^2 - Y^2}{\rho}, \tag{2.8}$$

$$G'' = \frac{2 \cdot XY}{\rho}. \tag{2.9}$$

The moduli are hence strongly coupled with the density. Constants A_1 and A_2 must be determined through calibration [11, 36]. Typically, required sample volumes are large to ensure operation in the gap loading limit (table 2.1). Note that the influence of inertia on the resonance behaviour can be of interest as well, for instance for the determination of film thicknesses [70].

Electromagnetically or magnetostrictively driven torsional resonators oscillate in a magnetic field. Specific examples include the multiple lumped resonator [37] or the torsional pendulum [38]. Contrary to piezo-driven resonators, detection of the oscillatory displacement is generally performed independently, *i.e.* either optically or electromagnetically via separate detection coils. Larger strain amplitudes are typically required to obtain sufficient signal to noise ratio (table 2.1). Romoscanu et al. [39] succeeded in performing calibration-free measurements by measuring the phase shift digitally, via a single excitation/detection coil, and by accurately modelling the system. In order to optimise the Q-factor as a function of the material properties, the resonating structure can be adapted, for instance by introducing coaxial segments [40]. More recently, Brack et al. [41] made use of such coaxial resonators to implement a method for simultaneous measurements at multiple discrete frequencies. Different attempts were made to combine torsional resonators with rotational devices for simultaneous steady shear flow and high-frequency measurements [71, 72]. Such instruments can be useful for probing materials under non-equilibrium conditions.

Resonators that analyse the frequency shift f_r and bandwidth Δf typically display a high resolution for low-viscous materials. Although the design of the resonating structure can be optimised to some extent towards the targeted fluids, the limit set by the Q-factor reduces the accuracy in case of excessive damping (table 2.1). To overcome this limitation, Wang et al. [42] adapted an electromagnetically driven pendulum apparatus for measurements on more viscous fluids. Viscoelastic properties were now obtained from the f_r together with either the maximum angular velocity ω_{max} or bandwidth Δf. The accuracy using the maximum velocity method increased with increasing damping and exceeded that of normal bandwidth measurements from $|\eta^*| > 0.2$ Pa·s. Furthermore, analysing the entire resonance curve allowed to use the resonator in a continuous mode around the resonance frequency [43]. Disadvantages were the presence of parasitic in-plane displacements in addition to the torsional motion, a rather limited frequency range, and severe design limitations due to the gap loading assumption at low frequencies (< 1 kHz, equation 2.2).

In addition to resonator methods, other types of torsional techniques have been developed. McSkimin [44] introduced a method for determining bulk viscoelastic properties in the kHz region by means of guided waves transmitted along an immersed cylindrical rod. The fluid impedance Z_f (equations 2.8−2.9) could

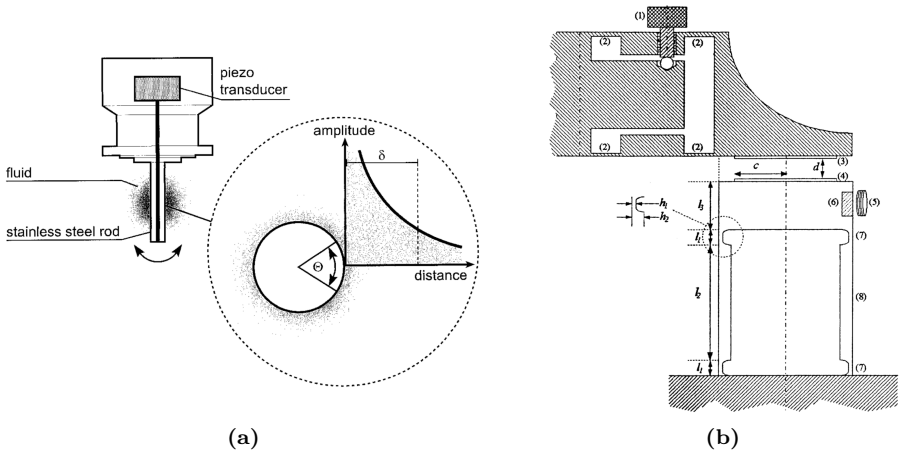

Figure 2.4: Overview of different resonator methods. (a) Schematic of a piezoelectrically driven torsional resonator and illustration of the wave penetration from the surface of the resonator into the sample [11]. (b) Drawing of a planar shear resonator: d is the gap between both substrates ((3),(4)); the bottom substrate is driven electromagnetically ((5),(6)) [48].

be derived semi-empirically from the measured attenuation and phase shift of the wave after reflection from the free end. Excitation and detection is carried out either using piezoelectric or magnetostrictive materials [44–46]. While most setups make use of immersed rods, hollow tube instruments with increased sensitivity and reduced sample volume were developed as well [46]. These instruments however require a full analysis of the viscoelastic wave propagation since surface loading conditions cannot be assumed for the fluid inside the tube. Generally, reflected wave methods show an increased applicability towards more viscous fluids compared to torsional resonators with freely damped waves (table 2.1). Moreover, operation outside of discrete resonance frequencies allows continuous operation and facilitates measurements at elevated temperatures. A major drawback was found to be the existence of non-linearities in the torsional motion which causes systematic errors [46, 47].

Planar shear resonators

In-plane oscillations of platelike structures create well-defined planar shear waves. Romoscanu et al. [48] developed an electromagnetically driven parallel plate resonator (figure 2.4 (b)). Test fluids are confined between the two plates with

an adjustable gap thickness of order $\sim 100\,\mu$m. At such gaps, wave propagation effects could not be ignored (equation 2.2), and the setup required in-depth analyses of the viscoelastic wave and fluid-structure interaction. Viscoelastic properties were derived by direct measurement of the frequency and phase shift of a damped reflected wave around discrete resonance frequencies, hence interpolating between different methods [34,44]. The instrument was performant in terms of accessible viscosity range compared to other resonator methods (table 2.1), although a correction factor was required for viscosities > 0.1 Pa·s. In addition, the setup requires much smaller sample volumes.

Other deformations

Resonators with different types of deformation modes were constructed as well, but have mainly been applied as viscometers. They are briefly discussed below (cantilevers and resonating viscometers). An exception is the vibrating wire rheometer, which make use of an immersed wire in a magnetic field [49, 50]. By fitting the measured voltage in the vibrating wire with theoretical models, measurements of the linear viscoelastic properties of low-viscous fluids were enabled within reasonable accuracy. The exact resonance mode (~ 1 kHz, table 2.1) can be altered via the amount of pretension on the wire. In a recent follow-up study, strain sensitive optical sensors were implemented for an enhanced accuracy on the measured displacement [51].

2.3.3 High-frequency ultrasound rheometers

High-frequency ultrasound rheometers employ resonance modes in the MHz range (figure 2.2). At such high frequencies, the penetration depth d_s (equation 2.3) reduces to the order of μm or smaller, depending on the fluid properties and exact frequency range. Consequently, only the microstructure near the wall of the resonator is probed and care must be taken that bulk properties are still being measured. Required sample volumes for surface loading operation on the other hand are much smaller.

Shear waves

Most ultrasound rheometers operate in shear mode and employ resonating thickness-shear quartz crystals. The resonance frequencies of these crystals are much higher than those used for torsional resonators. Thickness-shear mode resonators, or quartz crystal microbalances, were originally used for mass detection of thin films due to the strong sensitivity of the resonance curve to

the inertia of a loaded sample at very high frequencies [73, 74]. However, the resonance behaviour is influenced by viscous damping as well and detection of both frequency shift and bandwidth, for instance from impedance measurements, enabled the derivation of viscoelastic properties (equations 2.6 − 2.7) [52]. For instance, figure 2.5 (a) sketches a thickness-shear mode resonator and illustrates the change in resonance behaviour due to a load. A factor complicating the analysis is the strong coupling between inertia and viscoelasticity [73]. Decoupling these contributions is possible using wave interference at small gaps, but is difficult to carry out experimentally. Viscoelastic properties for different types of complex fluids could only be determined by accurate modelling of the behaviour of the thickness-shear mode resonator and fluid-structure interaction. For instance, Bandey et al. [53] described various loading conditions, including semi-infinite (surface loading) and finite (reflection effects) viscoelastic fluids, Newtonian fluids and ideal inertial layers. Although the crystals primarily exert a shear deformation, it was found that parasitic longitudinal waves are present and need to be taken into account as well [75]. In order to derive viscoelastic moduli, careful calibration with Newtonian standards of varying density and/or viscosity is required [54]. Despite these experimental difficulties, thickness-shear mode rheometers are relevant to obtain rheological information of viscoelastic fluids and films in the MHz range. Furthermore, they are sensitive towards low-viscous materials and only require a limited amount of sample compared to torsional resonators (table 2.1). More advanced configurations were developed

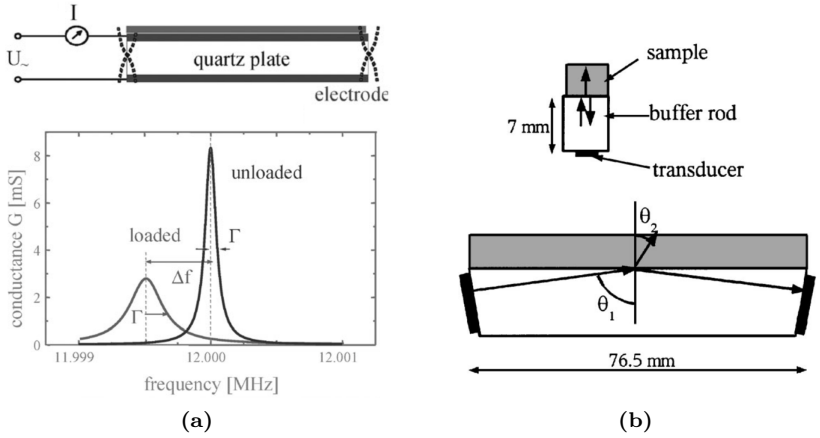

Figure 2.5: Examples of ultrasound rheometers: (a) illustration of a thickness-shear mode resonator and of the shift in the measured resonance behaviour due to a load placed on top of the quartz plate [73]. (b) Schematics of reflectometer setups with normal (top) or inclined incident waves (bottom) [59].

as well, such as a high temperature- and pressure-resistant setup (< 1 GPa, table 2.1) [55], or more recently a resonator with interdigitated electrodes for simultaneous measurements of mass, viscosity and conductivity [76].

Reflectometry

Mason et al. [56] introduced a different technique for determining viscoelastic fluid properties in the MHz range. Reflectometry is based on the analysis of the reflection coefficient of a planar shear wave at the interface of an elastic solid and the fluid under investigation. Quartz crystals are used for the creation of a planar shear wave, perpendicular to the propagation direction, as well as for the detection of the reflected wave. The wave travels through the elastic solid which shows no dispersion and only limited attenuation. As long as surface loading conditions are fulfilled, the thickness of the fluid sample does not influence the results [57]. Alig et al. [58] made an important advancement by adapting the original single-frequency pulse technique to a quasi-broadband acoustic system for simultaneous measurements over a wider frequency span. Figure 2.5 (b) illustrates different modes of operation depending on the angle of the incident/reflected wave to the surface, which can be normal or inclined. The fluid impedance Z_f (equations 2.8 − 2.9) can be derived from the measured complex reflection coefficient $R_f = \left|R_f\right| e^{-j\delta_f}$:

$$Z_f = Z_e \cos(\theta) \cdot \frac{1 - R_f^2 + 2jR_f \sin(\delta_f)}{1 + R_f^2 + 2jR_f \sin(\delta_f)}, \tag{2.10}$$

with Z_e the impedance of the elastic solid, θ the incident wave angle (figure 2.5 (b)), and $\left|R_f\right|$ and δ_f respectively the measured amplitude and phase of the reflection coefficient. Inclining wave setups are more sensitive due to an amplification of the signal (equation 2.10), and the optimal angle was observed to be $\theta \approx 77°$ [59]. Normal wave measurements however are easier to conduct experimentally and were found to be less prone to diffraction effects. Reflectometer setups showed a reduced sensitivity and accuracy compared to thickness-shear mode resonators, but the continuous frequency range can be of interest (table 2.1). Integrated reflectometry setups for measurements at elevated temperatures were constructed as well, employing either shear or longitudinal waves [77]. Although longitudinal ultrasonic transducers allow for a larger temperature range, shear waves are more sensitive. Ono et al. [78] combined both benefits by using shear waves converted from a longitudinal transducer for a high-temperature reflectometer setup with a potential range up to 400 °C.

2.3.4 Cantilevers and resonating viscometers

Immersed resonating structures can be used to determine bulk rheological properties at frequencies > 100 Hz (table 2.1). However, they generally require a large sample volume to fulfil surface loading conditions. Recent years have seen an increased interest for fluid characterisation at small scales, *e.g.* to reduce sample volumes or perform in-situ measurements. In combination with advances in fabrication methods, this has pushed the development of miniature fluid sensors.

Cantilevers

AFM microcantilevers have been used for various applications where high sensitivities are required, including force measurements or spectroscopy [79]. Furthermore, experimental investigations have shown that cantilevers operated at their resonance frequencies can be used for deriving fluid viscosities based on the oscillation displacement, which is used as a feedback parameter [80,81]. Such derivations generally incorporate a theoretical analysis performed by Sader [82] on the frequency response of an immersed beam cantilever, driven by a thermal driving force and undergoing flexural vibration modes. The size of the oscillating structure is typically much smaller than the wavelength of motion. As a result, hydrodynamic length scales were found to be very small ($\sim 10\,\mu$m), reducing the required sample volume (≤ 1 nl) but limiting the structural length scale that can be studied. Smaller cantilever dimensions showed an enhanced sensitivity for the fluid viscosity [83].

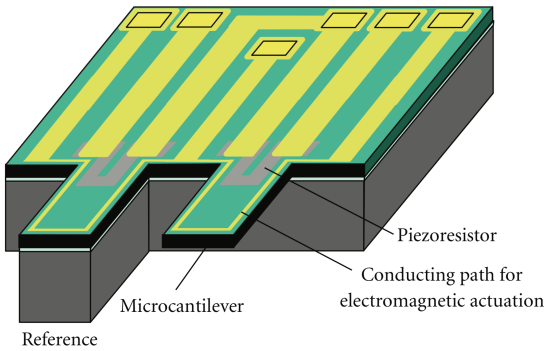

Figure 2.6: Schematic of a microcantilever on a silicon chip with integrated excitation and detection [60].

Deriving rheological properties from the frequency response of a cantilever is less trivial due to the complex flow field around the tip, and modelling the complex hydrodynamic force exerted by the fluid remains challenging [84]. Dufour et al. [60] determined linear viscoelastic moduli over a substantial frequency range around multiple discrete resonances ($1 - 100$ kHz) with a cantilever on a chip (figure 2.6, table 2.1). However, the resulting accuracy on the rheological properties was limited and improvements to both the experimental setup and modelling approaches are still necessary [61]. Similar to torsional resonators, the quality factor of the oscillation in the fluid must be sufficiently high for accurate detection of the frequency response. Larger 'mesoscale' cantilevers with reduced sensitivity but larger Q-factors were constructed for probing fluids with larger moduli [62].

Resonating viscometers

In addition to flexural cantilevers, other types of complex resonating structures have been developed for measuring fluid properties at elevated frequencies. Examples are membrane and immersed plate resonators with either Lorentz force or piezo actuation for tests on low-viscous fluids [85–88], or waveguide techniques for probing highly viscous fluids [89]. Miniaturised probes in particular offer substantial potential for in-situ measurements in confined environments [90]. However, a major drawback compared to more traditional resonance methods that undergo shear deformations is their often ill-defined deformation mode. Similar to cantilevers, describing the motion and determining the fluid-structure interaction is hence non-trivial and their applicability has been limited to detecting density and viscosity. A complete description of different viscosity probes is outside of the scope of this review.

2.4 Applications

This section elaborates on some of the applications for high-frequency rheometry. Note that this discussion is not exhaustive, but highlights some material classes for which high-frequency rheometry has proven useful. As already mentioned above, the exact location of the "high-frequency region" on an absolute frequency scale depends on the characteristics of the material, and we focus on examples for which homebuilt high-frequency setups rather than conventional rheometers are used. Only applications related to bulk viscoelastic properties are described here; high-frequency rheometry, and ultrasound rheometry in particular, can also be used to derive properties of viscoelastic films [91,92]. Furthermore, high-frequency methods, and resonators in particular, often display a high resolution

towards the detectable viscosity (table 2.1) and are suitable to measure the viscosity of low-viscous and/or biological fluids as well [93].

2.4.1 Macromolecular solutions

Solutions of macromolecules display a rich rheological behaviour with characteristic relaxation times that relate to microstructural properties. The high-frequency response can be used to investigate the microstructure on a local scale. In case of dilute solutions the fluid viscosity is generally low, rendering torsional resonator methods highly suitable for probing bulk properties (table 2.1). The Birnboim-Schrag multiple-lumped resonator [37] was used extensively for determining the viscoelastic behaviour of various dilute polymer solutions, such as star or comb-polymers [94, 95], and was applied for instance for estimating small degrees of long-chain branching based on the measured relaxation times [96]. Furthermore, both torsional resonators and oscillatory squeeze flow instruments have proven useful to study the short-time dynamics and structure of wormlike micellar solutions [14, 97, 98] or polysaccharide solutions [99]. By combining different rheometrical techniques together with DWS microrheology, Willenbacher and Oelschlaeger [14] provided an integrated picture of the viscoelastic response of a micellar solution, spanning a frequency range of 8 decades. The different techniques showed good agreement and characteristic features of the wormlike micelles such as the persistence length could be derived from the high-frequency terminal response.

2.4.2 Colloidal dispersions

Early work on colloidal dispersions dates back half a century; *e.g.* Hellinckx and Mewis [100] applied a guided wave method [44] to characterise pigment dispersions at high processing shear rates based on the Cox-Merz principle [101]. High-frequency rheology is particularly useful to study local dynamics and interactions in colloidal dispersions. The lower limit of the high-frequency region, and hence the required frequency range and technique, depends on the dominant characteristic time and length scales of the system. For instance for dilute hard spheres, the lower limit is set by the time scale of diffusional Brownian motion (equation 1.13) [102]. The upper limit is when fluid and particle inertial contributions come in to play. Both bulk resonators and subresonant piezo rheometers have been used to study colloidal dispersions. Ultrasound rheometers are of lesser interest; the high-frequency region is generally reached ≥ 1 kHz and the penetration depth will decrease to the order of the structural length scales of the material at higher ultrasonic frequencies (equation 2.3). The high-frequency

response can be used to obtain information on the interparticle interactions that play at length scales close the particle surface and revealed a complex interplay between thermodynamic and hydrodynamic contributions [12, 103]. The elastic modulus allows for direct analysis of the interaction potential [104], and was for instance used by Bergenholtz et al. [11] for colloidal charge determination in charge-stabilised dispersions. Conversely, the limiting high-frequency loss modulus only contains hydrodynamic contributions from the particles and medium and can be used to obtain microstructural information on the local scale. Results on emulsions are more scarce. Romoscanu et al. [39] for instance employed torsional and planar shear resonators for measuring the viscoelastic behaviour of emulsions near their characteristic relaxation time induced by droplet elasticity.

2.4.3 Polymers and composites

Although polymers can display a complex relaxation spectrum similar to macromolecular solutions, moduli are orders of magnitude higher and different measurement approaches are required. Subresonant piezo rheometers have been implemented for decades to study the properties of liquid-crystal polymers and/or composites [22, 25]. For instance, Zanna et al. [105] investigated the influence of different molecular parameters on the rheological properties of cross-linked polysiloxane. Piezo rheometry was combined with time-temperature superposition to extend the accessible range even more, and the high-frequency region could be used to determine the onset of and scaling in the Rouse regime. More recently, Atakhorrami et al. [106] studied the scale-dependent mechanics of semiflexible polymer networks representing the cytoskeleton of eukaryotic cells and compared bulk rheological properties with the local response obtained from microrheology. Important discrepancies were observed between both techniques in the intermediate regime (> 100 Hz), owing to local non-continuum effects. For homogeneous polymers with structural length scales that are sufficiently small (equation 2.3), faster processes at or above the intermediate regime can be probed by performing measurements at even higher frequencies. For instance, Szántó et al. [107] recently measured the entanglement relaxation time of polyethylene melts by means of quartz resonators operating in the MHz range.

2.5 Conclusions

Various high-frequency rheometrical techniques have been developed, spanning a frequency range from $0.1 - 10^8$ Hz. Table 2.1 presents a comparative summary of

different device types. Wave propagation effects play an important role in high-frequency rheology, and influence not only the experimental design parameters but also the structural length scales that can be probed. Subresonant rheometers are most similar to conventional rotational devices and are operated under gap loading conditions at frequencies < 10 kHz. Higher frequency techniques mostly assume surface loading and measure at or between resonance frequencies. For instance, both torsional and planar resonator setups were developed to determine rheological properties between $0.1 - 100$ kHz. Access to the MHz range could be obtained by employing different types of resonating structures, but the penetration depth of the wave decreases $< 10\,\mu$m and measured values do not necessarily represent bulk properties.

Different techniques target specific material classes and frequencies, and identifying a suitable high-frequency method depends on the exact application that is addressed. For many complex fluids, such as colloidal dispersions or micellar solutions, access to low-to-intermediate kHz frequencies is highly relevant for probing interactions and specific features of the local scale microstructure. Examining the ultrasound MHz range can be useful for detecting very fast processes and relaxation times of homogeneous materials, or to determine rheological properties of viscoelastic films. Furthermore, high-frequency rheology should be seen as complementary to conventional shear rheology. Combining high-frequency measurements with conventional rotational tests can offer an integrated view over the microstructure, ranging from collective properties at low frequencies to local scale properties at high frequencies.

Chapter 3

Design and analysis of a piezo shear rheometer

In this chapter, the design and analysis of a piezo shear rheometer is discussed. The first part is the design phase in which the focus gradually narrows from a broad conceptual stage to a detailed elaboration of the different elements. The the second part broadens again and starts from the construction and implementation of small elements towards a general functioning and optimalisation of the entire setup.

The design of the homebuilt setup was based on the specific application envisaged. In this case, the rheometer aims at characterising colloidal suspensions, focusing on their high-frequency limiting behaviour, which is typically reached at frequencies higher than 1 kHz. Another limit stemmed from the penetration depth of the travelling wave: relevant microstructural length scales in colloidal dispersions often reach μm dimensions and limit the maximum frequency for measuring bulk properties. Both design criteria favoured a rheometer able to operate in the high-frequency acoustic range with bulk properties being probed. Furthermore, in order to obtain an integrated rheological picture of a colloidal dispersion, the ability to span a continuous frequency range from low frequencies (*i.e.* measured with a conventional rotational device) to high acoustic frequencies is highly relevant. By means of a piezo shear rheometer, accessible frequencies could be directly extended into the acoustic range in a simple and robust manner. A critical design parameter is the optimisation towards high resonance frequencies, which determine the upper limit of the frequency window.

The chapter commences with a detailed explanation of the experimental setup. The design was aided by simulating the electromechanical behaviour of the setup in COMSOL Multiphysics. In a subsequent section, the calibration and performance of the instrument are discussed. The signal analysis was optimised to optimise the resolution towards lower viscous materials and sample properties can be derived in a straightforward manner. In order to improve the accuracy near the operating limits of the instrument, system-dependent effects need to be taken into account. The chapter ends with a validation of the setup by means of different viscous and viscoelastic standards.

Extracts of the following chapter appeared in published format and are adapted to shape this dissertation:

> B. Schroyen, J. W. Swan, P. Van Puyvelde, J. Vermant. Quantifying the dispersion quality of partially aggregated colloidal dispersions by high frequency rheology. *Soft Matter*, 13:7897, 2017.

B. Schroyen designed and executed the experiments, performed the data post-processing and wrote the major part of the manuscript.

3.1 Design of the piezo shear rheometer

3.1.1 Experimental setup

Figure 3.1 shows a schematic view of the piezo shear rheometer together with pictures of the frame and measurement cell. The measurement cell consists of two piezoceramic stacks (PICA P-141.05 Shear Actuators, PI Ceramic GmbH) that operate in a simple shear mode, similar in design to the device of Roth et al. [25]. The outer surface of the piezoceramic material is coated with an epoxy resin. Each stack is glued to a stainless steel base plate on one side and a square titanium substrate of 10 mm side length on the other. Samples are placed in between both piezo stacks. Both the excitation and detection of the measurement signal are performed by means of a LockIn amplifier (described in section 3.2.1). The BNC cables connecting the amplifier to the elements have to be carefully shielded to prevent electrical crosstalk.

The base plates of both elements are fixed to an aluminium frame, which serves as a support for the alignment tools and shields off the inner part of the cell from the environment. In order to optimise the alignment accuracy and efficiency, a three-point mechanical alignment method is used [108]. Inductive

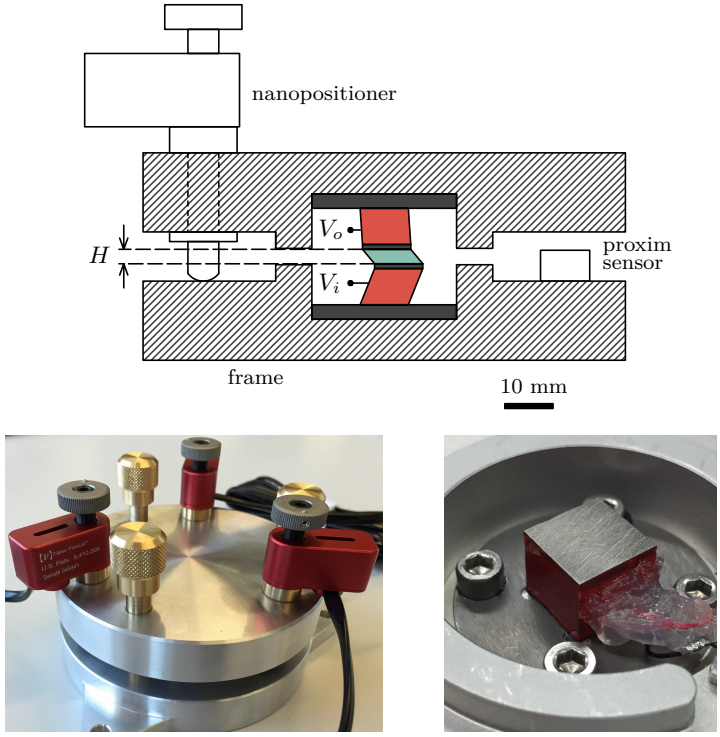

Figure 3.1: (top) Schematic of the piezo rheometer. (bottom) Pictures of the frame with nanopositioners and fixation screws (left) and of the piezoelectric stack used for excitation inside the measurement cell (right).

proximity sensors (SMT-9700 20N Non-contact Displacement Sensors, KAMAN Instrumentation) are installed on the bottom frame, measuring both the gap and parallelism with an accuracy of 10 nm and maximum range of 400 μm. The gap is controlled by 3 nano-positioning screws (8301 Piezo Linear Actuator, Newport Corporation) with a minimum step size of 30 nm. The zero-gap was determined by a combination of 2 methods: a) by determining the “rest" position of the upper plate on the lower plate by means of the sensors and b) by measuring frictional forces between the substrates of both elements during small amplitude oscillations. As a result, the alignment and zero-gap position could be determined with an accuracy of $\sim 1\,\mu$m, resulting in a level of parallelism $\leq 0.005°$. The gap setting is maintained by 3 large screws with ultra-fine threads to ensure a strong coupling. Finally, the bottom frame is fixed with 3 screws to a breadboard (Nexus Honeycomb Optical Breadbard, Thorlabs), which applies passive damping and provides solid support.

There is no specific temperature control foreseen and the setup needs to be operated under controlled laboratory environments. In principle, the setup is compact and can easily be placed in a temperature control box. the upper limit is determined by the nanopositioners and requires temperatures $< 50\,^{\circ}\mathrm{C}$, while the lower limit is set by the point at which condensation starts occurring. The piezoelectric shear stack can be used until 100 °C, so that more localised heating would allow for an extended temperature range.

3.1.2 Simulations

Simulations were performed to determine the electromechanical behaviour of the instrument. COMSOL Multiphysics (version 5.1), a finite-element analysis software, was used to model the multiphysics nature of the setup and efficiently vary different parameters for optimising the design.

Modelling of the piezo shear rheometer

The piezo shear rheometer was modelled for two different purposes. In a first step, only the measurement cell itself was considered to simulate the displacement and force detection of the piezoceramic stacks under standard operation. In a second step the measurement cell was integrated in the mechanical setup (figure 3.1) to aid the design of the frame and screws for maximising the 1st resonance frequency.

Figure 3.2 (left) shows the measurement cell simulated in COMSOL MP. The cell consisted of 2 piezoelectric stacks, coated with epoxy resin and mirrored against each other, titanium substrates and stainless steel base plates. Except for the piezoceramic material, standard material properties from the COMSOL MP library were used. The cell is simulated for two cases of gap loading: an air gap to simulate the free displacement of the bottom element, and a filled gap for calculating the voltage and displacement of the detection element. The properties of the piezoelectric material used for the models are listed in table 3.1 and were obtained from PI Ceramic. The piezoelectric coupling between mechanical and electrical contributions is described by the d coefficients. For the piezo shear stacks with alternating plates of opposite polarisation, the d_{15} coefficient is dominant and describes a shear deformation that is orthogonal to the electric field direction. Parasitic deformations stemming from thickness (d_{33}) or transverse (d_{15}) coefficients are effectively canceled out. The most important elements of the mechanical compliance matrix are listed as well and represent the deformability of the material. Note that the shear compliance (s_{55}) is very

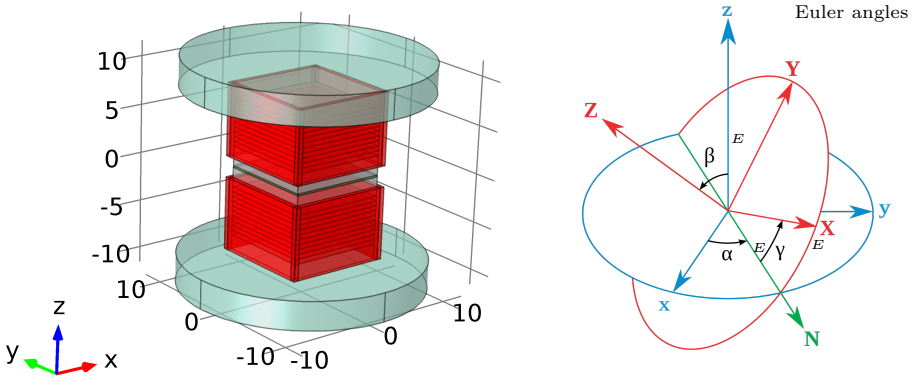

Figure 3.2: (left) Measurement cell simulated in COMSOL MP. The axes represent the coordinate system of the geometry. (right) Schematic illustrating the principals of Euler angles, applied for the coordinate systems of the piezoelectric crystals.

small compared to that of typical soft materials and can typically be ignored during operation.

The material properties in table 3.1 are defined in the coordinate system of the piezoelectric crystal. Hence, the orientation of the crystal axes needs to be described by means of their Euler angles with respect to the coordinate system of the geometry (figure 3.2). The 3rd axis is generally defined as the polarisation direction. In case of a shear deformation with a dominant d_{15} coefficient, the 1st axis indicates the electric field direction which induces a rotation around the 2nd axis. Table 3.2 lists the Euler angles for the different crystal orientations in the 2 stacks, which are mirrored against each other and contain alternating plates of opposite polarisation (+,−). The orientations were implemented by means of rotated coordinate systems.

The physics were implemented in COMSOL MP via the 'Piezoelectric devices' interface, combining solid mechanics and electrostatics with the governing equations for piezoelectric materials. Except for the piezoelectric stack, the

Table 3.1: Material coefficients for PIC255 (provided by PI Ceramic).

coupling		compliance		other	
d_{31} [m/V]	$-1.74 \cdot 10^{-10}$	s_{11} [m^2/N]	$1.59 \cdot 10^{-11}$	ρ [kg/m^3]	7800
d_{33}	$3.94 \cdot 10^{-10}$	s_{33}	$1.07 \cdot 10^{-11}$	ϵ_r [-]	1700
d_{15}	$5.35 \cdot 10^{-10}$	s_{55}	$4.49 \cdot 10^{-11}$	ν [-]	0.36

Table 3.2: Euler angles for the different crystal orientations with respect to the geometrical coordinate system (x, y, z).

crystal	α_E [rad]	β_E [rad]	γ_E [rad]
bottom, +	0	$3\pi/2$	$3\pi/2$
bottom, −	0	$\pi/2$	$\pi/2$
top, +	0	$3\pi/2$	$\pi/2$
top, −	0	$\pi/2$	$3\pi/2$

domains were assumed to behave as linear elastic materials within the small deformations applied. The governing equations describing the solid mechanics are based on the equilibrium momentum equation. In the absence of body forces and initial stresses, their time domain representation is given by:

$$-\rho\frac{\partial^2 \mathbf{x}_z}{\partial t^2} = \nabla \cdot \boldsymbol{\Sigma}, \tag{3.1}$$

$$\boldsymbol{\epsilon} = s\boldsymbol{\Sigma} + d^T\mathbf{E}. \tag{3.2}$$

In the equations above, ρ is the density, $\mathbf{x}_z$ the displacement field, $\mathbf{E}$ the electric field and $\boldsymbol{\Sigma}$ and $\boldsymbol{\epsilon}$ respectively the stress and strain tensors. The coefficients s and d are described in table 3.1. Equation 3.2 contains a second term that is only present within the piezoelectric domains and represents the coupling with the electric field. Hence, the mechanical behaviour is coupled with the electrostatics, which can be described by:

$$\nabla \cdot \mathbf{D}_E = \rho_v, \tag{3.3}$$

$$\mathbf{D}_E = \epsilon_0\epsilon_r\mathbf{E} + d\boldsymbol{\Sigma}, \tag{3.4}$$

with $\mathbf{D}_E$ the electric displacement field, ρ_v the charge density and ϵ_r and ϵ_0 the relative permittivity and permittivity of free space, respectively. The first expression (equation 3.3) ensures the conservation of charge, while the second expression (equation 3.4) describes the relationship between the electric displacement field, electric field and stress. Note that above, the naming convention of solid mechanics theory is applied. Above equations are written in their strain-charge form.

The different boundary conditions that were applied are listed in table 3.3. The measurement cell (figure 3.2) was fixed mechanically both at the top and bottom base plates. The electric connections represent the electrodes on the piezoelectric elements, alternating between voltage and ground connections. The excitation connections are controlled by a sinusoidal output voltage from the LockIn

Table 3.3: Boundary conditions applied in the solid mechanics interface (top) and electrostatics interface (bottom).

fixed surfaces	$\mathbf{x}_z = 0$
free surfaces	/
free surfaces	$\mathbf{n} \cdot \mathbf{D}_E = 0$
connections excitation	$V = V_o \cdot \sin(2\pi f \cdot t)$
connections detector	$\frac{\partial Q_0}{\partial t} = I_{ext}$
ground connections	$V = 0$

amplifier. Detector connections were circuit connected, relating the total charge induced by the electric displacement field (equation 3.4) to an external current, to enable voltage detection. A zero-charge boundary condition was applied to the outside surfaces of the insulator. For simulations with a filled gap loading, a sample with properties equal to one of the viscous calibration standards was used (ρ = 970 kg/m^3 and η = 0.97 Pa·s). Simulating the interplay with a viscous sample requires solving the Navier-Stokes equations in an additional multiphysics coupling and necessitates a finer mesh. In order to reduce the calculation time the sample was simulated as a linear elastic material with a frequency dependent modulus G equivalent to η (via $G \sim |G^*| = 2\pi f \cdot |\eta^*|$). The resulting amplitude is therefore the same as for the actual viscous sample. Note that the effect of the sample on the simulated detected voltage is simple and is expected to depend linearly on its modulus (via $\sigma = |G^*| \cdot x_{z,o}/H$ and equation 3.4) except for materials with very large moduli, for which the compliance of the piezoelectric stack affects the deformation (equation 3.2). While such samples are outside the scope of this study, it can be worthwhile to simulate the behaviour of the stacks near these compliance limits. Damping or dielectric/coupling losses were not taken into account for this simple model.

Figure 3.3 displays the free displacement (air gap) of the excitation stack at f = 1 kHz. The sinusoidal output voltage (table 3.3, excitation) induces a sinusoidal shear deformation as a result of the inverse piezoelectric effect (equation 3.2). The deformation in the normal direction is insignificant over the entire oscillation cycle. It must be realised that this is an ideal curve and that in real operation, hysteresis can be present [109]. It is therefore important to monitor the raw input signal from the detection element as well (described in section 3.2.1). Figure 3.3 (right) illustrates the deformation mode at the peak displacement. The calculated peak displacements are $x_{z,o}$ = 53.5 nm and $z_{z,o}$ = 0.014 nm in the shear and normal directions, respectively. This shear deformation value agrees with the simplified prediction for free deformation $x_{z,o} = d_{15}V_o$ (equation 3.2).

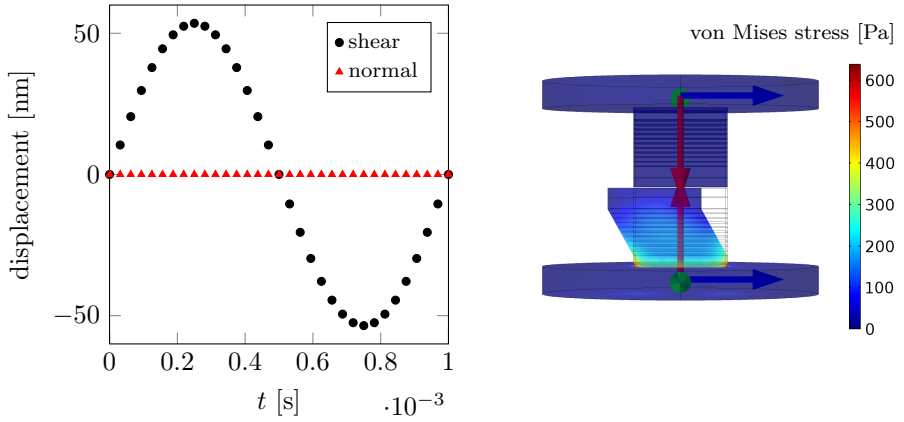

Figure 3.3: Simulation of the free displacement of the bottom stack, used as the excitation element, at $f = 1$ kHz and $V_o = 10$ V. (left) Oscillating displacement in the shear and normal directions as a function of time. (right) Rescaled peak displacement. The coloured axes in the model illustrate the coordinate systems of the piezoceramic stacks (+). The colour scaling represents the von Mises stresses.

When the sample is confined between both plates, the applied deformation results in a shear stress on the top element. Figure 3.4 compares the magnitude of the simulated input voltage with the predicted voltage based on $V_i = \frac{d_{15}}{C} \cdot F_i = \frac{d_{15}}{C} \frac{S}{H} \cdot x_{z,o} \cdot |G^*|$ (equation 3.4), with d_{15} the shear deformation coefficient and $C = 2.8 \cdot 10^{-8}$ C/V the capacitance of the entire piezoceramic stack (table 3.4). The gap thickness $H = 200$ μm. At a frequency of 1 kHz, the measured output voltage at the circuit ends of the detector piezo equaled $V_i = -31.8\,\mu$V; the negative sign results from the relative orientation of the two piezoceramic stacks. This relates to a sample induced displacement and force at the detection surface of $x_{z,i} = d_{15} \cdot V_i \approx 0.17$ pm and $F = F_i = F_o \approx 0.17$ mN. The measured viscosity can hence be derived via $|\eta^*| = \frac{H}{S} \frac{F_i}{x_{z,o}} \frac{1}{2\pi f} \approx 0.99$ Pa·s, which is close to the predefined viscosity of 0.97 Pa·s. The small discrepancy can be caused by assumptions and errors in the simulation near the element's edges.

Ultimately, the resonance behaviour of the entire setup was simulated in COMSOL MP by performing an eigenfrequency study. The setup was fixed from the bottom surface of the frame, representing the fixation to the breadboard, while all the other surfaces were left unconstrained. Results were used for design optimisation of the frame and fixation screws. Figure 3.5 displays the mode shape of the current setup at the 1st resonance frequency at $f \sim 2.9$ kHz. At this frequency, the nanopositioners are resonating, and these elements were required for the alignment. Special fixation screws were manufactured with

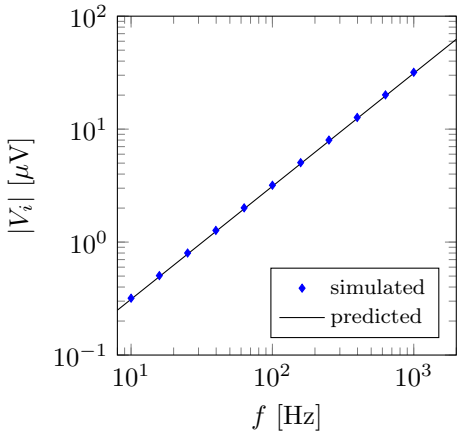

Figure 3.4: Magnitude of the input voltage at the detection element with a confined sample ($\eta = 0.97$ Pa·s) for different frequencies at $V_o = 10$ V. The values simulated in COMSOL MP are compared with predicted values based on the coefficients of the piezoelectric stack.

an ultra-fine thread to push the 1st resonance frequency as much as possible towards this high limit. Fixing the bottom plate of the setup thoroughly to the breadboard is critical: simulations showed that an unconstrained setup results in much lower resonance frequencies.

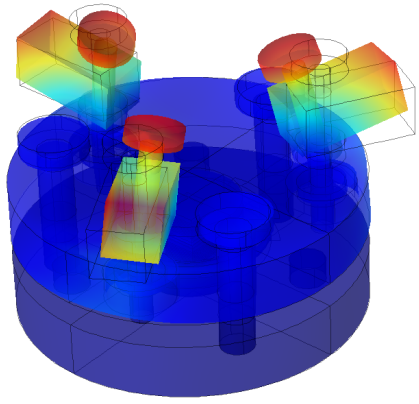

Figure 3.5: Mode shape at the 1st resonance frequency, occurring at ~ 2.9 kHz. The setup is fixed at the bottom surface of the frame.

Effect of the level of parallelism

Within the linear viscoelastic region, errors in the gap height only result in an under-/overestimation of the modulus due to their effect on the strain amplitude. The influence of errors in parallelism however is far less trivial as it can create complex shear and squeeze flow patterns. The effect of misalignment between the two substrates on the measured input voltage was simulated in COMSOL MP. Figure 3.6 (left) shows a schematic of the simulated geometry and consists of 2 blocks representing the piezoelectric stacks. A viscous fluid ($\eta = 0.97$ Pa·s) was confined in the gap. The bottom wall creates a shear deformation at a velocity $u_o = x_{z,o} 2\pi f \cdot \cos(2\pi f \cdot t)$ (equation 3.2). On the other hand, the top wall is stationary, kept at an average gap height $H = 100$ μm and is gradually tilted to decrease the level of parallelism. The fluid behaviour was simulated in the 'Laminar flow' interface, which combines the Navier-Stokes and continuity equations, hence solving for the velocity field $\mathbf{u} = (u,w)$ and pressure P.

The influence of misalignment on the measured input voltage was determined by calculating the shear induced stresses. Stresses acting on the detector surface S in the flow (x) and gradient (z) directions were calculated via a combination

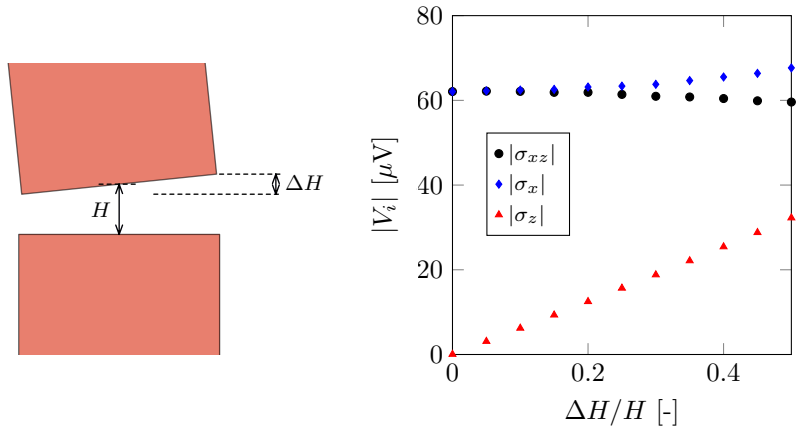

Figure 3.6: Simulated effect of the error in parallelism on the voltage amplitude measured at the top stack for a gap of 100 μm ($f = 1$ kHz, $V_o = 10$ V). (left) Schematic of the tilted geometry (dimensions axes in mm). (right) Comparison of different stress contributions : (a) only viscous shear stresses operating in the x-direction, (b) total stresses in x, and (c) total normal stresses.

of hydrostatic and viscous contributions [19]:

$$\sigma_x = -\eta \cdot \left[2\frac{\partial u}{\partial x} + \left(\frac{\partial u}{\partial z} + \frac{\partial w}{\partial x}\right) \right], \tag{3.5}$$

$$\sigma_z = P - \eta \cdot \left[\left(\frac{\partial u}{\partial z} + \frac{\partial w}{\partial x}\right) + 2\frac{\partial w}{\partial z} \right]. \tag{3.6}$$

When the surfaces are perfectly aligned (error = 0 μm), the main contribution to the measured stresses stems from the shear deformation so that $\sigma_x \approx \sigma_{xz} = -\eta \cdot \frac{\partial u}{\partial z}$. Note that at such small gaps, analytical approximations can be derived as well via the lubrication theory. Nonetheless, these are less generally applicable for tilted surfaces and simulation results are shown here. Figure 3.6 compares the different stress contributions as a function of the dimensionless error on parallelism $\Delta H/H$. The input voltage magnitude is calculated via $|V_i| = \frac{d_{15}}{C} \cdot |\sigma| \cdot S$ (equation 3.4). Normal forces can induce electrical signals through the thickness coefficients of the piezoelectric material. Although these coefficients are largely cancelled out in the stack due to the alternating polarisation of the plates, the remnant coefficient can be as large as 2 % of the d_{15} coefficient [110]. A maximum value of $0.02 \cdot d_{15}$ was hence taken for the coupling between normal forces and voltage. At perfect alignment, $\sigma_x = \sigma_{xz}$ and $\sigma_z = 0$, and the calculated complex viscosity $|\eta^*| = \frac{C}{d_{15}} \cdot |V_i| \cdot \frac{H}{x_{z,o} 2\pi f \cdot S} \approx 0.97$ Pa·s. With decreasing alignment, σ_{xz} decreases slightly in magnitude while the total shear stress increases due to the presence of gradients of u in the flow direction as well. On the other hand, pressure contributions lead to large normal forces that rise with increasing alignment error. The input voltage was found to deviate significantly from the expected value due to alignment errors $> 5\,\%$ of the measurement gap. The sign of this deviation depends on the direction of the tilt with respect to the relative orientation of the stacks. The simulations hence imply that for measurement gaps $\leq 100\,\mu$m, an alignment accuracy in the order of $\sim \mu$m is required for correct determination of the amplitude. Note that the measured phase angle is expected to be even more sensitive to the level of parallelism.

3.2 Calibration and performance

3.2.1 Signal detection

The method for signal detection and analysis is presented in two parts. The first part describes the signal generation and detection under ideal operation, *i.e.* without any mechanical or electrical losses. In the second part the transfer

function of the electronic circuit is derived for correcting the measured voltage signal near the instrument limits.

Signal generation and detection with a LockIn amplifier under ideal conditions

Figure 3.7 shows a schematic of the electrical components present in the setup. The piezoceramic stack positioned at the bottom is used as the excitation unit and is connected to the low-impedance reference output of a LockIn amplifier (MFLI, Zurich Instruments), which applies a sinusoidal output voltage signal $V_o(t)$:

$$V_o(t) = V_o \cdot e^{(j2\pi ft)}. \tag{3.7}$$

As a result of the inverse piezoelectric effect, the sinusoidal output voltage creates a linear shear deformation $x_{z,o}(t)$ at the bottom substrate surface

$$x_{z,o}(t) = d_{15} V_o(t), \tag{3.8}$$

with d_{15} the shear deformation coefficient of the stack (table 3.4). The maximum output amplitude of the LockIn amplifier equals 10 V, resulting in a displacement amplitude $x_{z,o} = 53.5$ nm. The setup is operated in the gap loading limit so that the deformation wave propagates completely through the sample and induces a shear force $F(t)$ on the top substrate which is directly proportional to the sample properties [20]. The limits of this assumption and the correction applied when operating outside of these limits are discussed in section 3.2.4. Within the gap loading limit, $F(t)$ has the same frequency as the applied motion but differs in phase. The resulting shear movement of the piezoceramic plates hence

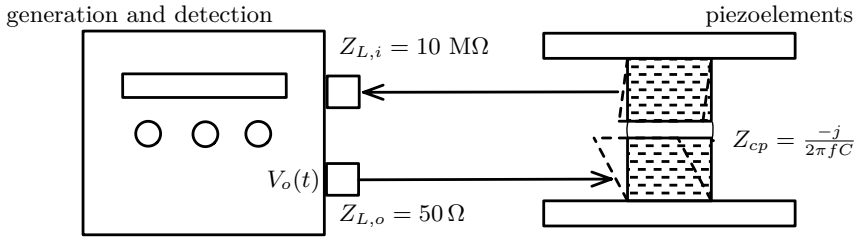

Figure 3.7: Signal generation and detection in the setup: schematic of the electrical components contributing to the signal.

Table 3.4: Parameters of the PICA P-141.05 piezoceramic stacks, consisting of 10 active plates. Values are provided by PI Ceramic.

# active layers	10
width	10 [mm]
height	7.5 [mm]
d_{15} (stack)	$5.35 \cdot 10^{-9}$ [m/V],[C/N]
C (stack)	$2.8 \cdot 10^{-8}$ [C/V]
J	$4.49 \cdot 10^{-11}$ [m^2/N]

generates a sinusoidal voltage signal $V_i(t)$

$$V_i(t) = \frac{1}{d_{15}} x_{z,i}(t) = \frac{C}{d_{15}} F(t), \tag{3.9}$$

which is recorded by the voltage input $V_{Ls}(t)$ of the LockIn amplifier:

$$V_{Ls}(t) = \frac{V_i}{2} \cdot \left[e^{j(2\pi f_{Ls} t + \theta_{Ls})} + e^{-j(2\pi f_{Ls} t + \theta_{Ls})} \right]. \tag{3.10}$$

θ_{Ls} is the measured phase shift with respect to the reference. Note that equations 3.8 − 3.9 are derived assuming that the compliance of the piezoceramic stack is negligible compared to that of the sample, which is a valid assumption for most soft materials. If this is not the case, the effect of the shear stress on the output displacement has to be accounted for (equation 3.2). The input impedance of the LockIn amplifier is kept at the maximum value of 10 MΩ to avoid voltage losses. Figure 3.8 shows the raw voltage input signal for a highly viscous PDMS standard measured at $f = 1$ kHz. The measured input voltage is a clean sinusoidal signal without noticeable hysteresis, similar to the simulated output voltage (figure 3.3). Although the displacement curves of voltage-controlled piezo actuators often show hysteresis [109], this mainly occurs at large electric field strengths. Within the applied output voltage amplitude of 10 V, which is small compared to the accessible range of the stacks (+/- 250 V), the level of hysteresis appears to be small.

Depending on the sample properties, the magnitude of the input voltage can be below 1 μV. The influence of environmental electric noise, with magnitudes as high as 500 μV, can be removed by careful setting of the LockIn amplifier's parameters. The input signal is multiplied with the complex reference signal $V_{ref}(t) = \sqrt{2} e^{(-j2\pi f t)}$ and allows both amplitude and phase detection:

$$V_{Ls}(t) \cdot V_{ref}(t) = \frac{V_i}{\sqrt{2}} \left(e^{j[2\pi(f_{Ls} - f)t + \theta_{Ls}]} + e^{-j[2\pi(f_{Ls} + f)t + \theta_{Ls}]} \right). \tag{3.11}$$

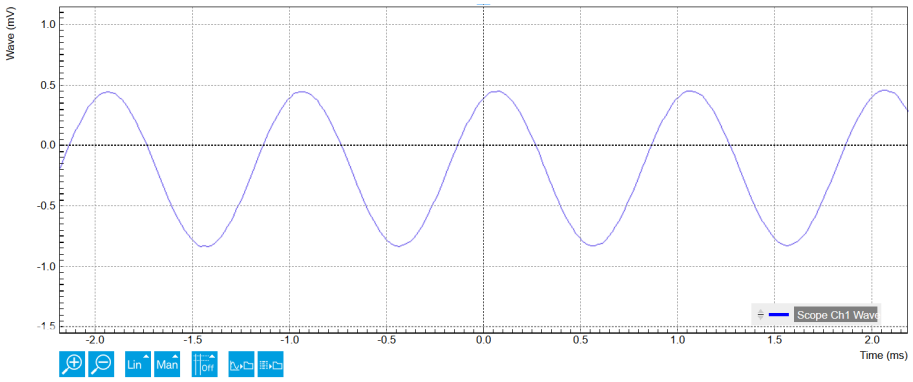

Figure 3.8: Raw voltage input signal measured by the oscilloscope of the LockIn amplifier at a frequency of 1 kHz. The sample is a highly viscous PDMS standard, chosen for a large signal-to-noise ratio at the input.

The signal of interest, resulting from the first term, is a slow component with a frequency $f_{Ls} - f$. In order to remove higher frequency components, the demodulated signal is subsequently sent through a low-pass RC filter $\langle\cdot\rangle$. The bandwidth setting of the filter is crucial and determines the frequency window that is considered around the reference frequency. Lowering the filter bandwidth results in enhanced noise cancellation and accuracy, but increases the filter time. Depending on whether the accuracy or speed needs to be optimised, the filter bandwidth is varied between $0.05 - 0.5$ Hz for measurements at demodulation frequencies higher than 10 Hz. In addition, the filter order is maximised to enhance the suppression of noise on the phase angle. The sampling rate is kept high (~ 100 kHz) to enhance the A/D conversion. At such narrow bandwidths, $2\pi(f_{Ls} - f)t < \theta_{Ls}$ for all cases, so that the filtered signal can be reduced to

$$\left\langle V_{Ls}(t) \cdot V_{ref}(t) \right\rangle = \frac{V_i}{\sqrt{2}} \cdot e^{j\theta_{Ls}}. \tag{3.12}$$

The resulting signal can be decomposed in an in-phase and out-of-phase signal:

$$X_i = \frac{V_i}{\sqrt{2}} \cdot \cos(\theta_{Ls}), \tag{3.13a}$$

$$Y_i = \frac{V_i}{\sqrt{2}} \cdot \sin(\theta_{Ls}), \tag{3.13b}$$

which can be corrected further after calibration.

Transfer function of the electric circuit

The schematic of the electronics displayed in figure 3.7 contains contributions of the piezoelectric stacks and the impedances of the LockIn amplifier, and both the output and input circuit consist of 2 elements in series. The actual output voltage at the piezoelement $V_{cp,o}$ is reduced by losses from the output of the LockIn:

$$V_{cp,o} = V_o - V_{L,o} = \frac{V_o}{\left(1 + \frac{Z_{L,o}}{Z_{cp}}\right)}, \tag{3.14}$$

with $Z_{L,o} = 50\,\Omega$ the output impedance of the LockIn and $Z_{cp} = \frac{-j}{2\pi f C}$ the capacitive impedance of the piezoelement. The relationship between the shear-induced voltage $V_{s,i}$ and measured voltage at the input of the LockIn amplifier V_i is given by:

$$V_{s,i} = V_{c,i} + V_i = V_i\left(1 + \frac{Z_{cp}}{Z_{L,i}}\right). \tag{3.15}$$

$Z_{L,i} = 10$ MΩ is the input impedance of the LockIn amplifier. The resulting force-displacement relationship in the sample, related to $V_{s,i}$ and $V_{cp,o}$ through equations 3.2 and 3.4, can then be written as a function of the measured input and output voltages V_i and V_o via the transfer function of the electric circuit:

$$\frac{F}{x_{z,o}} \propto \frac{V_{s,i}}{V_{cp,o}} = \frac{V_i}{V_o} \cdot \left(1 - \frac{j}{2\pi f C Z_{L,i}}\right) \cdot \left(1 + j2\pi f C Z_{L,o}\right). \tag{3.16}$$

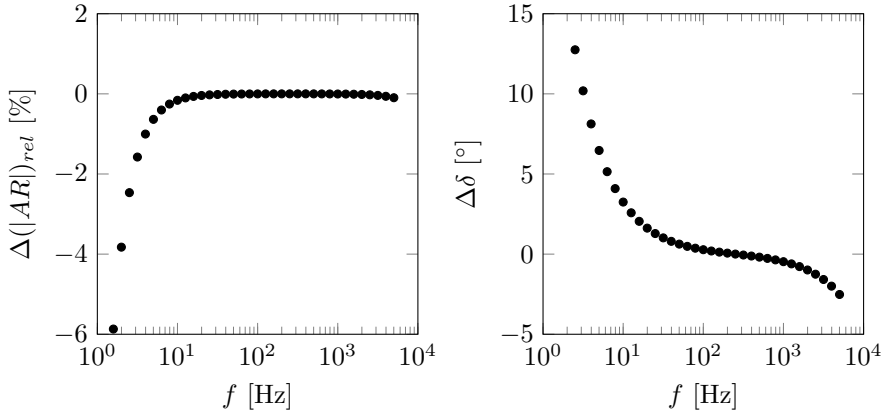

Figure 3.9: Effect of the transfer function of the electric circuit on the measured amplitude ratio ($(\Delta|AR|)_{rel}$, left) and phase shift ($\Delta\delta$, right) as a function of frequency.

Figure 3.9 shows the effect of the transfer function on the measured amplitude ratio and phase. At a frequency range between $10 - 2000$ Hz, $|Z_{cp}|$ varies between $570 - 2.8$ kΩ. Hence, at frequencies ≤ 10 Hz, the assumption that $Z_{cp} \ll Z_{L,i}$ is no longer valid, resulting in an underestimation of the amplitude due to electrical losses and an overestimation of the phase angle. On the other hand, at frequencies > 1 kHz, Z_{cp} decreases in magnitude and $Z_{L,o}$ affects the signal, leading to a decrease in $x_{z,o}$ and an underestimation of both amplitude and phase. Note that the effect in the intermediate frequency range is negligible. However, for accurate phase angle measurements in the low- or high-frequency limits, the detected signal V_i needs to be corrected.

3.2.2 Calibration

The amplitude ratio and phase angle of a sample can be determined from the input $V_i(t)$ via $\frac{F}{x_{z,o}} \propto \frac{V_i}{V_o} \cdot \frac{C}{d_{15}^2}$ and $\delta \propto \theta_{Ls}$. However, the measured signal is influenced both by the electric circuit (equation 3.16) and by potential mechanical contributions from the instrument itself. The latter include effects due to elasticity, damping and inertia of the mechanical components. These instrumental parameters were determined via a 2nd-order mechanical model for the force-displacement relationship:

$$F(t) = m\frac{d^2x_{z,o}}{dt^2} + \xi\frac{dx_{z,o}}{dt} + K_s x_{z,o}, \tag{3.17}$$

with m, ξ and K_s the mechanical system constants for inertia, damping and stiffness. The frequency response is obtained by applying the Laplace transform and taking the short-term frequency behaviour. The transfer function of the instrument in the frequency domain is given by

$$\frac{F}{x_{z,o}} = -m(2\pi f)^2 + \xi j(2\pi f) + K_s, \tag{3.18}$$

and contains both in- and out-of-phase components.

The parameters were determined by simultaneously fitting the raw data for PDMS standards of different viscosity. The following conclusions could be drawn from the calibration:

(i) There was no conclusive evidence of mechanical contributions stemming from damping or elasticity within the detectable limit over a frequency range $f = 10 - 2000$ Hz. However, strong inertial resonance effects appear above 2000 Hz. Since these resonance modes are uncontrolled, they were not further analysed.

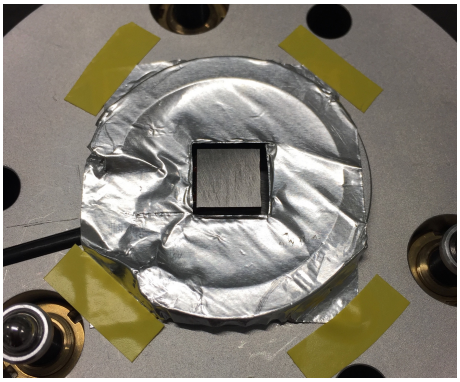

Figure 3.10: Shielding of the piezoceramic stack and connections used for detection with aluminium tape.

(ii) Electrical cross-talk between the excitation and detection units created a low-frequency plateau value. Although predominantly in-phase, the phenomenon is complex in nature and changes with frequency. The unshielded magnitude equals $\approx 10\,\mu$V and is of opposite sign compared to the actual input signal, which is negative due to the opposite polarisation direction of the two stacks. The cross-talk mainly acts on the electrodes/cables of the detection element and could be removed almost completely by proper shielding of the detector (figure 3.10). Two parameters $(K_{c,X}, K_{c,Y})$ were introduced for correcting the residual in- and out-of-phase values: $K_{c,X} = 12$ N/m, $K_{c,Y} = 2$ N/m.

(iii) The uncertainty on the material parameters provided by PI Ceramic (table 3.4) was accounted for by applying a (constant) correction factor A for the magnitude of the force-displacement relationship. An optimal value $A = 1.03$ was determined.

Taking into account the calibration results and contributions from the electric circuit (equation 3.16), the in- and out-of-phase moduli (with $|G^*| = \frac{H}{S} \cdot |AR|$) can be calculated via:

$$G' = \frac{H}{S} \cdot \left[\left(\frac{F}{x_{z,o}} \right)_X + \left(\frac{F}{x_{z,o}} \right)_Y \cdot \left(\frac{1}{2\pi f C Z_{L,i}} - 2\pi f C Z_{L,o} \right) \right], \tag{3.19a}$$

$$G'' = \frac{H}{S} \cdot \left[\left(\frac{F}{x_{z,o}} \right)_Y + \left(\frac{F}{x_{z,o}} \right)_X \cdot \left(- \frac{1}{2\pi f C Z_{L,i}} + 2\pi f C Z_{L,o} \right) \right], \tag{3.19b}$$

with

$$\left(\frac{F}{x_{z,o}}\right)_X = \frac{-\sqrt{2}X_i}{V_o} \cdot \frac{A \cdot C}{d_{15}^2} + \left(K_{c,X}\right), \tag{3.20a}$$

$$\left(\frac{F}{x_{z,o}}\right)_Y = \frac{-\sqrt{2}Y_i}{V_o} \cdot \frac{A \cdot C}{d_{15}^2} + \left(K_{c,Y}\right). \tag{3.20b}$$

X_i and Y_i are the measured in- and out-of-phase voltages (equations 3.13a − 3.13b). C and d_{15} are the capacitance and coupling coefficient of the piezoelectric stacks, $K_{c,X}$ and $K_{c,Y}$ the contributions of the electric cross-talk, A is a fitting parameter and $Z_{L,i}$ and $Z_{L,o}$ are the impedances of the LockIn amplifier. Note that in the equations above the corrections are applied to the in- and out-of-phase values, which are the direct outputs of the demodulated signal in the LockIn amplifier. However, it would be equally correct to apply the transfer functions to the composed complex values $X_i + jY_i$. The moduli in equations 3.19a − 3.19b are related to the complex modulus and phase via:

$$|G^*| = \sqrt{G'^2 + G''^2}, \tag{3.21}$$

$$\delta = \tan^{-1}\left(\frac{G''}{G'}\right). \tag{3.22}$$

It must be realised that the correction for the electric cross-talk (equations 3.20a − 3.20b) is dominantly in-phase and is critical only for low-viscous samples. On the other hand, the transfer function of the electric circuit (equations 3.19a − 3.19b) mainly affects the measured phase angle near the limits of the frequency window considered here (figure 3.9). Only the 1st order contributions of the transfer function (equation 3.16) are accounted for, since the 2nd order contribution is negligible. As a result, it can be concluded that the correction factors in equations 3.19b − 3.20a are important when measuring near the operating limits of the device, either in $|AR|$ or in f. In the extreme case of very strong samples ($|G^*| > 10^8$ Pa), the compliance of the piezoceramic stack should be accounted for as well (equation 3.2).

3.2.3 Performance and limits of the device

The accessible frequency range of the PSR relevant for extending that of commercial devices is between 10 − 2000 Hz. Above 2000 Hz resonances dominate the response. The setup can be used below 10 Hz when accounting for the transfer function of the electric circuit. The operating gap H is usually kept within 200 μm to ensure a complete filling and to reduce deviations from the gap loading limit (see section 3.2.4). Smaller gaps increase the maximum

strain and hence the sensitivity in case of low-viscous materials, but alignment becomes more crucial. The setup is operated at room temperature in a controlled laboratory environment. Note that the applied voltages are small; therefore the potential dissipation of energy during operation remains limited. No measurable effects of heating were monitored during longer operation even at $f = 2$ kHz.

Figure 3.11 shows the $|AR|$ and δ for 3 PDMS grades of different viscosities, measured at a gap of 200 μm. Measurement values were corrected based on equations 3.19a − 3.20b. The results are in good agreement with predictions based on the Newtonian (zero-shear) viscosity values and illustrate the onset of viscoelastic responses at higher frequencies, where the slope of the amplitude ratio starts to decrease and the phase angle deviates from 90°. The sensitivity limit of the amplitude ratio was determined from the random noise value on the input of the LockIn amplifier, which is specified by the manufacturer as $|V_{noise}| = 7\sqrt{f}$ nV. Taking a safety factor of 10, this corresponds to a frequency dependent minimum amplitude ratio of $|AR|_{\min} \approx 7.1\sqrt{f}$ m/V. The upper limit is set by the compliance of the piezoceramic stack relative to that of the sample.

The low-frequency range of the PSR overlaps with the accessible frequency range of a commercial device. By direct comparison of the measured phase angle with that of a commercial stress-controlled rheometer, the phase resolution of the PSR was determined to be $\delta_{err} \approx 2°$. Note that the phase angle of the least viscous calibration standard is scattered at low frequencies and shows large deviations from 90°. In this region the amplitude ratio falls below the noise limit, hence reducing the accuracy on the measured phase as well.

3.2.4 Gap loading effects

In the gap loading limit the deformation wave propagates completely through the sample without a change in amplitude or phase. The propagated wave induces a shear force $F(t)$ on the top substrate directly proportional to the sample properties. In order to operate in this limit, the measurement gap H must be much smaller than the shear wavelength λ_s [20, 111]:

$$H \ll \lambda_s = \frac{1}{f\sqrt{\frac{\rho}{|G^*|}}\cos(\frac{\delta}{2})}. \tag{3.23}$$

λ_s decreases with frequency and depends on the properties of the sample: the density ρ, complex modulus $|G^*|$ and phase δ. As an illustration, figure 3.12 plots the limiting complex viscosity for a viscous fluid ($\rho = 1000$ kg/m^3, $\delta = 90°$) for which $\lambda_s = 10H$ as a function of frequency f and gap height H [20]. Detection from the stationary wall is presumed. Below this curve, the measured

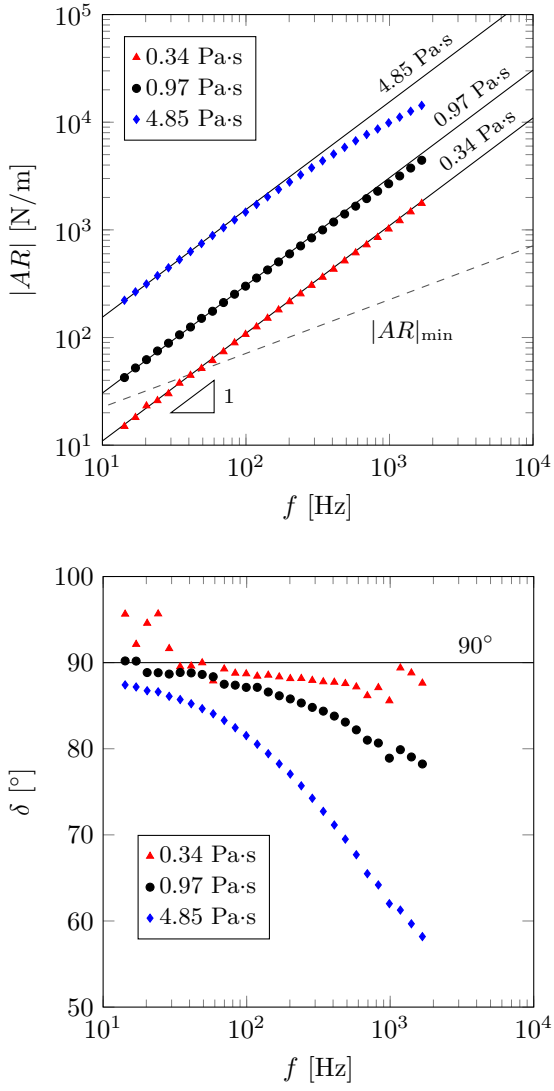

Figure 3.11: Measurements of 3 PDMS grades of different viscosities, showing the frequency dependency of the amplitude ratio $|AR|$ (top) and phase angle δ (bottom). The solid lines are the low-frequency Newtonian limits. The dashed line on the amplitude ratio graph represents the lower sensitivity limit.

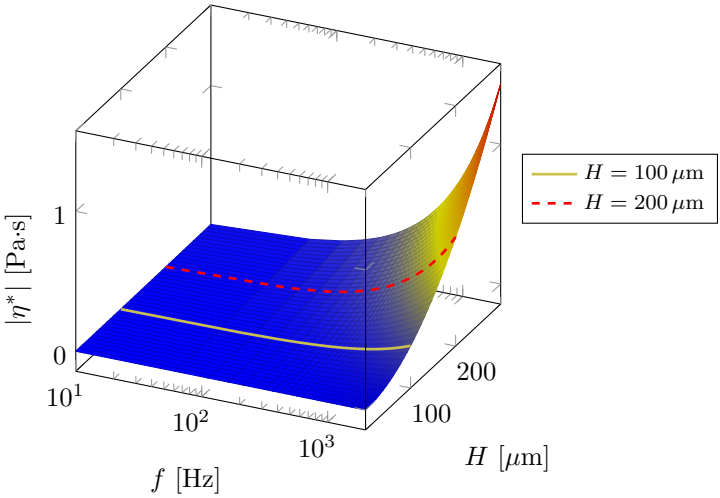

Figure 3.12: Limit of the complex viscosity for which the shear wavelength equals $\lambda_s = 10H$ as a function of the frequency f and gap height H. The surface plot presents the limit for a Newtonian fluid ($\delta = 90°$) with density $\rho = 1000$ kg/m^3. Yellow (full) and red (dashed) lines highlight the limits at gaps of 100 and 200 μm.

properties deviate substantially from those of the actual sample because the assumption of operation in the gap loading limit no longer holds true. For a viscous PDMS standard of 0.34 Pa·s measured at $f = 1$ kHz, λ_s equals ∼2 mm, so that important deviations occur at $H > 200\,\mu$m. The highlighted curves at $H = 100$ and 200 μm demonstrate that decreasing the gap drastically increases the accessible viscosity range. Note that for elastic samples, for which the phase angle $\delta = 0°$, limiting complex viscosity values increase by a factor 2 (equation 3.23).

In order to correctly analyse fluids with low complex viscosities, the measured moduli need to be corrected further. The propagation of a shear wave in complex fluids is a non-trivial problem to solve due to its strong dependency on the viscoelastic properties of the sample [17, 18, 112]. Schrag [20] calculated the role of wave propagation effects on rheological measurements and provided expressions for correcting the measured viscoelastic properties in case of a shear wave travelling between two walls. For measurements at the stationary wall, the expressions for correcting the measured modulus $|G^*_m|$ and phase δ_m reduce

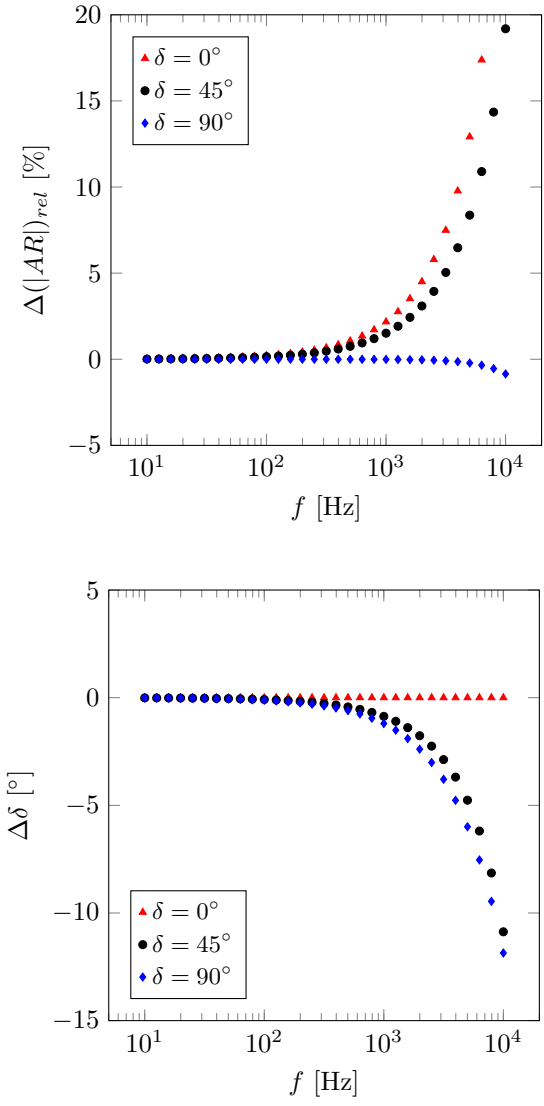

Figure 3.13: Influence of shear wave propagation effects on the measured amplitude ratio ($(\Delta|AR|)_{rel}$, left) and phase shift ($\Delta\delta$, right) as a function of frequency. The calculations are executed at the stationary wall ($H = 100\,\mu$m) on a sample with $\rho = 1000$ kg/m^3 and $|\eta^*| = 0.5$ Pa·s.

to:

$$\frac{|G_m^*|}{|G_{cor}^*|} = \beta H \cdot \left[\tan^2\left(\frac{\delta_{cor}}{2}\right) + 1\right]^{1/2} \left[\frac{1}{\cosh\left(\tan\left(\frac{\delta_{cor}}{2}\right) \cdot 2\beta H\right) - \cos(2\beta H)}\right]^{1/2}, \tag{3.24}$$

$$\delta_m - \delta_{cor} = -\left(\frac{\delta_{cor}}{2}\right) + \tan^{-1}\left(\frac{\tanh(\alpha H)}{\tan(\beta H)}\right), \tag{3.25}$$

with factors $\alpha = 2\pi f\left(\frac{\rho}{|G_{cor}^*|}\right)^{1/2}\sin(\delta_{cor}/2)$ and $\beta = 2\pi f\left(\frac{\rho}{|G_{cor}^*|}\right)^{1/2}\cos(\delta_{cor}/2)$. $|G_{cor}^*|$ and δ_{cor} are the corrected amplitude and phase, respectively, and are equal to $|G_m^*|$ and δ_m only in the gap loading limit. Note that both functions are coupled and need to be solved together. Shear wave propagation effects on the measured amplitude ratio and phase are compared in figure 3.13 for different phase angles ($|\eta^*| = 0.5$ Pa·s) at a measurement gap of 100 μm. The effect strongly depends on the phase angle of the sample: with decreasing phase angle, the influence on the amplitude increases whereas that on the phase becomes less important. Furthermore, while the phase shift is always negative, the shift in $|AR|$ evolves from negative to positive with decreasing phase angle, eventually even leading to an overestimation of the modulus.

The calculations in figure 3.13 indicate that correcting for wave propagation effects is indeed important for samples with a low modulus of the complex viscosity. As an illustration, figure 3.14 compares the complex viscosity and phase angle of a viscous sample ($|\eta^*| \approx 0.084$ Pa·s), measured at $H = 100\,\mu$m, before and after correction (equations 3.24 − 3.25). Results of the correction confirm the calculations in figure 3.13 and present mainly a shift in phase for the viscous fluid. The corrected viscosity and phase are, within experimental accuracy, constant and at their expected values. Note that the input voltage is close to the detection limit for such a low-viscous sample, hence explaining the substantial scatter. Furthermore, resonances are more strongly visible due to a reduced viscous damping.

3.3 Validation

3.3.1 Overlap with a commercial device: viscous, viscoelastic and elastic samples

The accessible frequency range of commercial rotational rheometers and that of the PSR overlaps at frequencies around 10 Hz, hence allowing for direct comparison of measurement data. Low-frequency measurements were generally

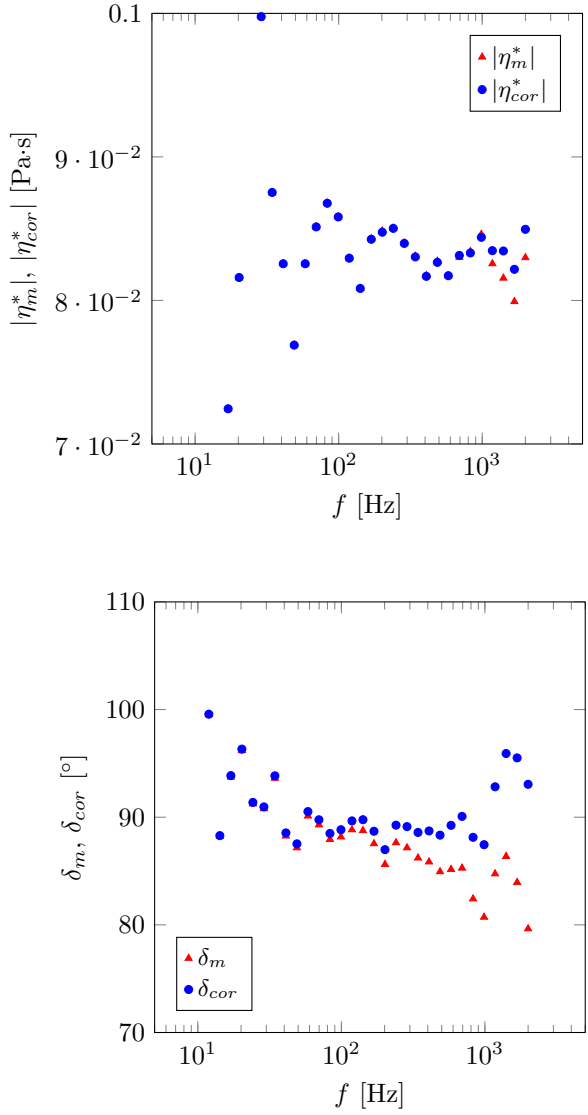

Figure 3.14: Comparison before and after shear wave propagation correction for a low-viscous fluid ($|\eta^*| \approx 0.084$ Pa·s, $\rho = 960$ kg/m^3).

performed on a stress-controlled rheometer (DHR-3, TA Instruments) with a cone-and-plate geometry of 40 mm diameter (1° cone angle). High-frequency measurements were carried out at a gap of 200 μm.

The frequency dependent behaviour and overlap of a 0.34 Pa·s PDMS grade is plotted in figure 3.15. The phase angle is most sensitive to errors and non-idealities. Measurement data from the PSR at lower frequencies (10-20 Hz) show scattering due to the sensitivity limit (figure 3.11). Furthermore, at high frequencies ($>$ 1 kHz), the phase angle is prone to small resonances. The results are also compared with measurement data obtained with a piezo rheometer at MPI Mainz [25]. The setup has a similar operation principle as the PSR, using 2 stacks of piezo shear elements, but signal detection is performed by means of a charge amplifier. Furthermore, the alignment is carried out optically before sample loading. Although both measurement sets are qualitatively similar, the PSR appears more sensitive and accurate, particularly in terms of the phase angle δ. On the other hand, the MPI device has a temperature control unit with an operation range up to 50 °C.

Figures 3.16 − 3.18 respectively show the extended frequency sweeps ranging from a high-viscous PDMS grade (η_0 = 291 Pa·s) to a viscoelastic standard (11.8 wt% PIB in pristane) and an elastic film (cured PDMS). Measurement data on the viscous and viscoelastic samples display good overlap between low- and high-frequency data in amplitude as well as in phase. Comparing the high-frequency data between figures 3.15 − 3.16 also illustrates the increased accuracy over a larger frequency range in case of samples with higher moduli. The measured voltage is well above the sensitivity limit over the entire frequency range, while viscous damping reduces the effect of resonances. Elastic materials are generally more difficult to measure due to a stronger mechanical coupling in the absence of damping. The phase angle measured with both devices shows remarkably good overlap. However, the amplitude differs by an order of magnitude. An important difference between the cured PDMS and the other viscoelastic samples is that the cured film is an elastic material for which stresses do not relax over time. A potential cause could therefore be the difference in applied normal stress, which cannot be controlled in the PSR and which plays an important role in case of a solidlike sample. The PDMS film was cured before loading and substantial residual stresses can still exist in the material during measurement.

3.3.2 Comparison with TTS data

In the frequency range probed by the PSR, validation is more difficult as measurement results can only be compared with those of other homebuilt devices. For rheologically simple materials with a single dominant relaxation mechanism,

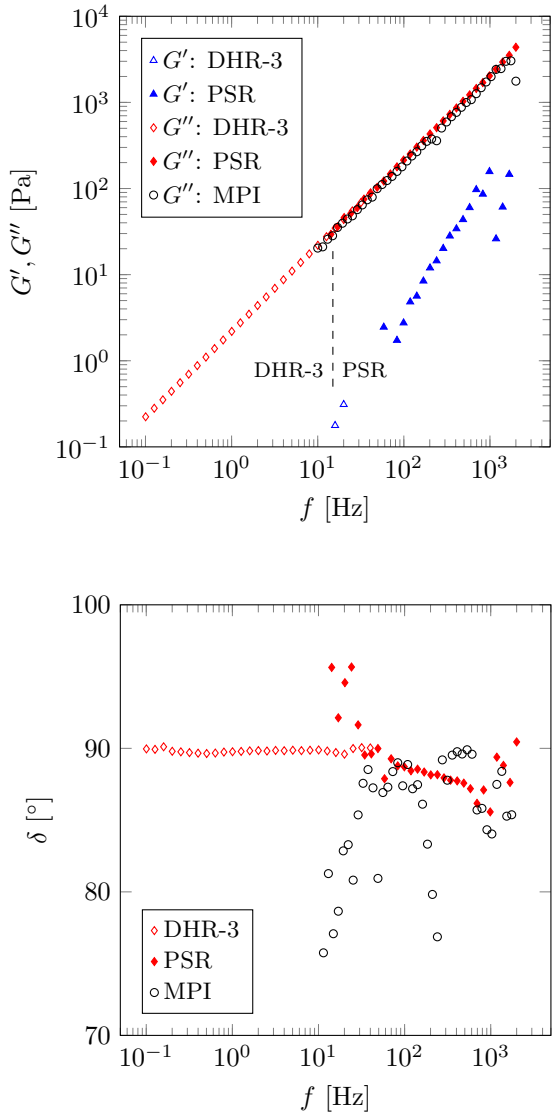

Figure 3.15: Behaviour of a 0.34 Pa·s PDMS grade over an extended frequency range. Low-frequency data were obtained with the DHR-3 (open symbols) and high-frequency data with the PSR (closed). The data are compared with measurements performed at MPI Mainz [25].

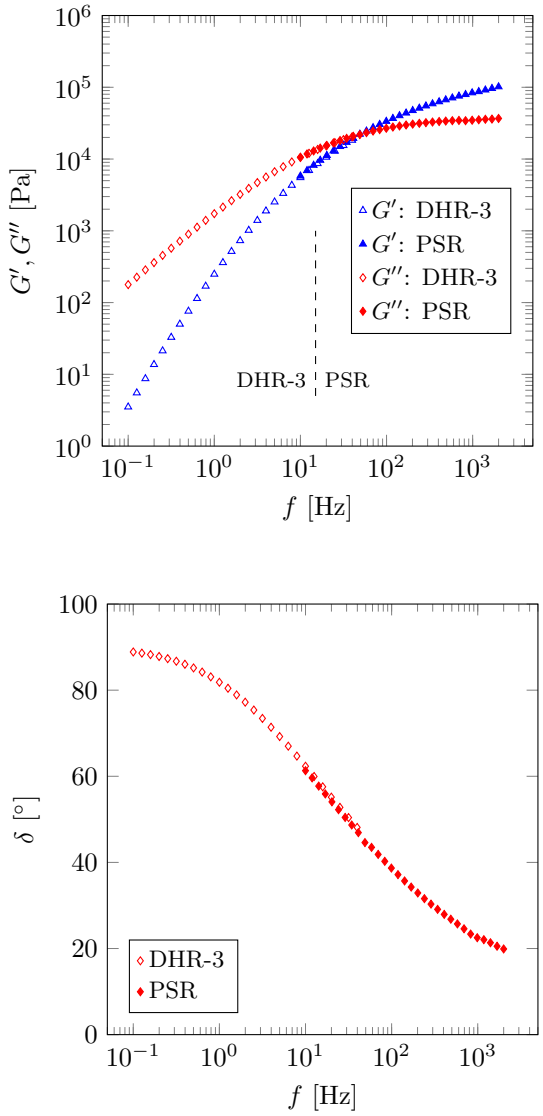

Figure 3.16: Comparison of the linear viscoelastic behaviour of a high-viscous PDMS grade ($\eta_0 = 291$ Pa·s) at low (open symbols) and high frequencies (closed).

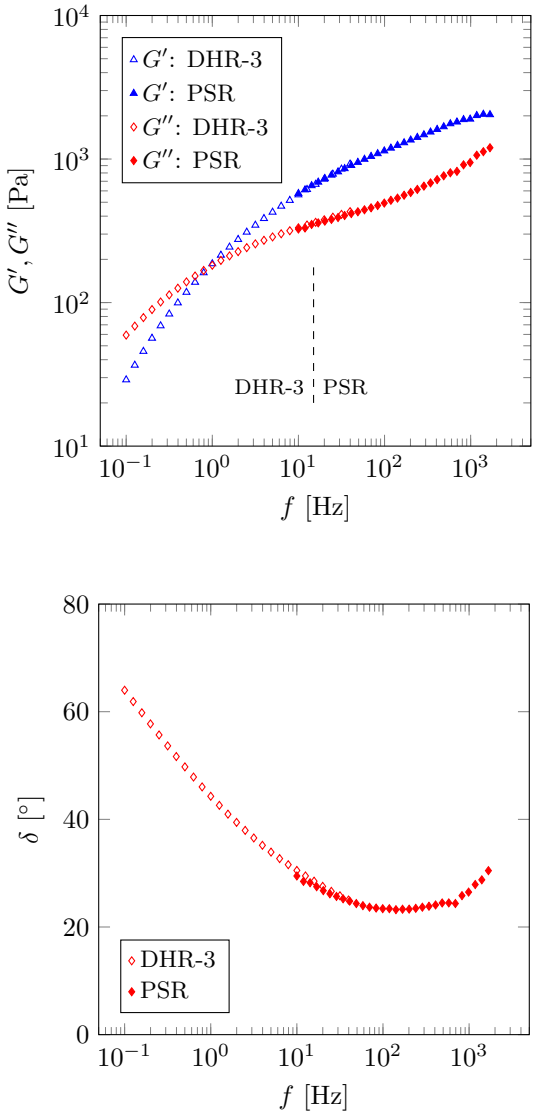

Figure 3.17: Linear viscoelastic behaviour of a solution of 11.8 wt% PIB in pristane (NIST standard).

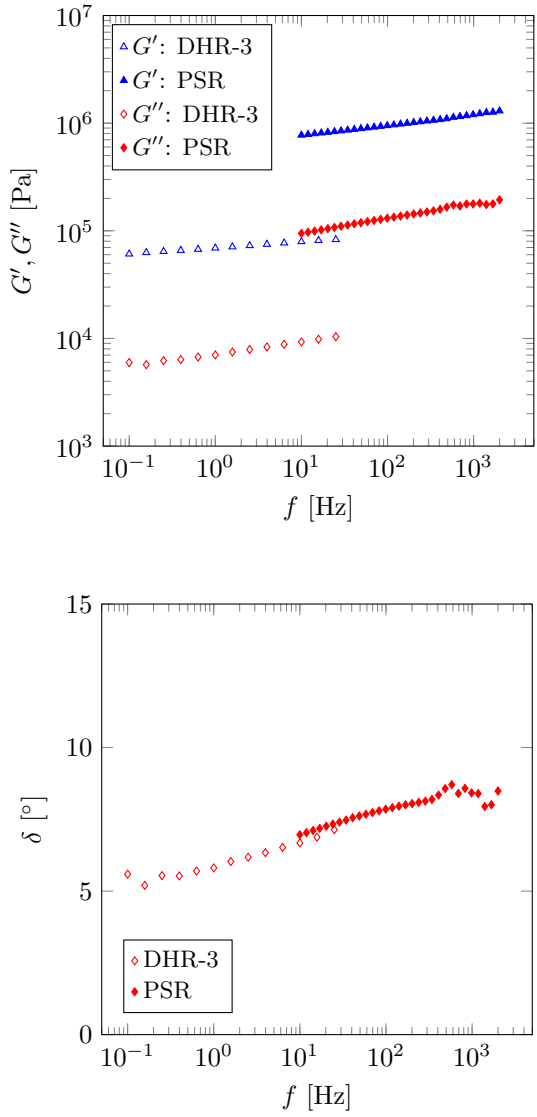

Figure 3.18: Cured PDMS film of 1 mm thickness measured at low and high frequencies.

the principle of time-temperature superposition (TTS) can be applied to validate the measurement data [15]. Figures 3.19 (a) − (b) compare measurement results with data obtained via TTS for 2 different linear polyisobutadienes (PBD) of increasing molecular weight. Both the synthesis of the PBD as well as the construction of the TTS curves were performed at FORTH in Crete. Qualitatively, the results agree for both samples. For the lowest molecular weight (PBD-L3, figure 3.19) the phase angles measured by the PSR deviated from the TTS data. This could be caused by errors in the TTS data as well, since the accuracy of the shifts was found to decrease at lower molecular weights. For the highest molecular weight (PBD-L12, figure 3.19), phase angle data agree within $< 2^\circ$ over the entire frequency range. However, the measured amplitude was overall overestimated by the PSR measurements. This was unexpected since generally the phase angle is most prone to errors, and it is yet unclear whether this was caused by the PSR or TTS data. However, since this overestimation was not observed for other viscoelastic samples (section 3.3.1), and since the phase angle data agreed, this was not investigated further.

3.4 Conclusions

A piezo shear rheometer was developed for measurements on soft materials at frequencies above 10 Hz. Although piezo rheometers are inherently most suited for materials with higher moduli, the design is optimised for accurate measurements on lower viscous fluids as well. A three-point mechanical alignment method, consisting of nano-positioning screws and inductive proximity sensors, was installed for accurate gap control between $0 - 400\,\mu$m. Furthermore, the signal analysis was carried out by means of a LockIn amplifier with narrow filter settings for sensitive detection. The electromechanical behaviour of the rheometer was simulated in COMSOL MP and used for optimising the design of the setup in terms of the 1st resonance frequency. Simulations of the displacement and force detection of the piezoelectric stacks were in line with simple theoretical predictions based on a pure shear deformation profile under perfect conditions. The 1st resonance frequency was determined by means of an eigenfrequency study and occurs at ~ 2.9 kHz for the current setup; the mechanical design was optimised to approach this limit as much as possible. In addition, the influence of errors in parallelism on the measured amplitude was simulated, showing important deviations at errors $> 5\%$.

The viscoelastic properties of a material confined in between both piezoelectric stacks can be determined from the measured input voltage. However, the measured signal is influenced by factors other than the response of the sample as well. The impedances of the LockIn amplifier interfere with those of the

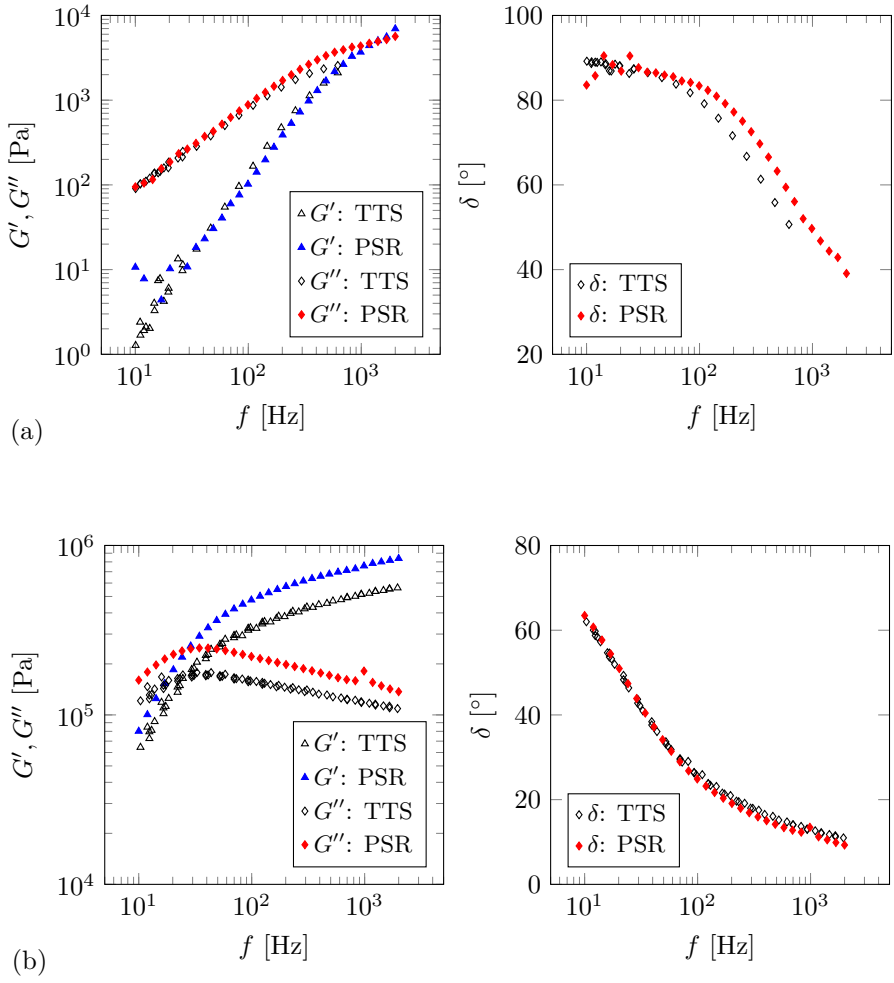

Figure 3.19: Linear viscoelastic behaviour of PBD-L3 (a) and PBD-L12 (b) compared with TTS results.

piezoelectric stacks both at low (< 20 Hz) and high (> 1 kHz) frequencies. Small amounts of electric cross-talk between the electrodes of the piezoelectric stacks further influence the signal. Mechanical contributions of the setup, stemming either from inertia, damping or elasticity, were not detected except for high frequencies (> 2 kHz), when resonances dominate the response. The setup was calibrated by taking the cross-talk and transfer function of the electric circuit into account, resulting in accurate amplitude and phase detection at frequencies between $10 - 2000$ Hz. The setup is generally operated in the gap loading limit, indicating that the shear wave propagates completely through the sample. For low-viscous fluids measured at higher frequencies, an additional correction factor is required that accounts for deviations from this limit. Ultimately, the setup was validated by comparing measurements on viscous and viscoelastic samples with data obtained with a commercial device (using the overlap region) and time-temperature superposition data, showing good overall agreement.

-

Chapter 4

Stress contributions in colloidal suspensions: influence of the surface topology

The surface characteristics of colloidal particles in a dispersion strongly influence the stress contributions that arise near the particle surface. These contributions are responsible for specific phenomena in colloidal suspensions, such as shear thickening or the occurrence of considerable normal stress differences. In this chapter, we employ our piezo shear rheometer (see chapter 3) to study the high-frequency response of colloidal suspensions. Different model particles are used, ranging from sterically stabilised colloids with various stabilisation layer thicknesses to raspberry-like particles with controllable surface roughness. By probing the suspensions at frequencies higher than their characteristic frequencies, or at fast time scales, the local stress contributions at length scales near the particle surface can be derived. Doing so, we reveal an intricate interplay between different contributions depending on the surface characteristics in which lubrication stresses, repulsive interactions and topological features play a role.

The following chapter is written in a format of a manuscript to be submitted:

B. Schroyen, C.-P. Hsu, L. Isa, P. Van Puyvelde, J. Vermant. Stress contributions in colloidal suspensions: influence of the surface topology

B. Schroyen designed and executed the rheological experiments, performed the data post-processing and wrote the manuscript.

4.1 Introduction

Colloidal suspensions are an interesting class of materials that are encountered in a wide range of natural and synthetic applications. Their behaviour is inherently complex due to the Brownian nature of the constituents, and is further governed by hydrodynamic and thermodynamic interactions [113]. This interplay between different interaction forces brings about a rich behaviour under flow. A fundamental understanding is of critical importance, for instance for the effective design of product formulations or enhancement of process operations.

Surface characteristics of the colloidal particles play a crucial role and alter the response both directly through the interparticle interactions and indirectly via the microstructure [3]. While characteristics such as surface charges can create long-range interactions, topological features mainly play a role on the local scale. A prominent example is their influence on the extent of shear thickening, the increase in viscosity that can be seen when the suspensions are sheared at high stresses or shear rates [114]. The phenomenon was shown to originate from strong lubrication forces that arise between particles being pushed together [3]. These forces occur in a very thin boundary layer between the surfaces of two particles, and are hence strongly influenced by local scale stresses and surface topology [115, 116]. For instance, the role of surface roughness and frictional interactions in the shear thickening behaviour of colloidal suspensions has been the subject of several recent studies [117–120].

Colloidal probe techniques such as AFM can be used for direct and quantitative measurements of surface topology and interaction potentials [121–124]. Although highly useful, such methods do not take into account the hydrodynamic interactions between particles which act through the suspending medium, and hence do not completely describe the complex behaviour in suspensions that arises from the intricate interplay between the different stress contributions [125]. Here, rheology is adopted as a method to directly study the stress response of particles in suspension. Rheology, and small amplitude oscillatory measurements in particular, allows to study the behaviour of colloidal suspensions at different

structural length scales. The total deviatoric stress in a suspension $\boldsymbol{\Sigma}$ can be written as [126, 127]

$$\boldsymbol{\Sigma} = 2\eta\dot{\boldsymbol{\epsilon}} + \boldsymbol{\Sigma}_p = 2\eta\dot{\boldsymbol{\epsilon}} + \left(\boldsymbol{\Sigma}^H + \boldsymbol{\Sigma}^B + \boldsymbol{\Sigma}^P\right). \tag{4.1}$$

Here, $\dot{\boldsymbol{\epsilon}}$ is the bulk rate of strain tensor so that $2\eta\dot{\boldsymbol{\epsilon}}$ represents the suspending fluid stress. The particle contribution to the stress $\boldsymbol{\Sigma}_p$ can be further decomposed into hydrodynamic ($\boldsymbol{\Sigma}^H$), Brownian ($\boldsymbol{\Sigma}^B$) and interparticle ($\boldsymbol{\Sigma}^P$) contributions. Except for the hydrodynamic term, which is purely dissipative in nature, particle contributions contain both elastic and viscous components. Experimental studies indicated the sensitivity of the high-frequency rheological response to the local scale interactions between particles [11, 103, 128, 129]. The effect of the surface characteristics on hydrodynamic and thermodynamic stress contributions was further quantified by theoretical and numerical work [126, 127, 130].

In this chapter, we apply this theoretical framework to identify the rheological stress contributions caused by differences in the surface topology of colloidal particles. The topological features of the colloids were varied in two distinctive manners by using different particle types. Sterically stabilised particles with varying grafted layer thicknesses were employed to study the effect of a polymer brush on local scale interactions [131]. Furthermore, the role of distinct asperities was investigated by using raspberry-like particles with controlled surface roughness [124, 132]. The stress response is analysed over an extended frequency range. In doing so, we aim at probing frequencies that are high compared to the characteristic frequencies of relaxation processes in the suspension, or inversely, at probing small structural length scales near the particle surface [102]. As an additional application, the shear thickening behaviour of the different suspensions is investigated.

4.2 Experimental

4.2.1 Model systems

PMMA-*g*-PHSA suspensions

Sterically stabilised PMMA particles have been used since long for model colloidal suspensions [3]. Their synthesis was recently revisited by Palangetic et al. [131] for an improved control over the chain length of the polyhydroxystearic acid (PHSA) stabiliser. In this work, PMMA-*g*-PHSA particles are used as model colloids with a tuneable grafting layer. A full description of the synthesis can be found elsewhere [131]. Three different model particles were used with varying

Table 4.1: Experimental parameters of the PMMA-*g*-PHSA particles. a_c is the core particle radius determined via SEM images, h_{co} the layer thickness based on the contour length, h_h the hydrodynamic layer thickness from DLS measurements, DP the degree of polymerisation and R_g the estimated radius of gyration for a good solvent [131].

	a_c [nm]	h_{co} [nm]	h_h [nm]	R_g [nm]	DP
PMMA-3.8	850	6	6	2.3	3.8
PMMA-5.5	365	8.5	8	2.8	5.5
PMMA-46	360	60	20	10.7	46

grafted layer thicknesses and core radius a_c. The grafting density s_p is high, with an average area ~ 0.75 nm^2 per grafted molecule. The core size of the particles was determined via SEM micrographs (appendix A.1.1, figure A.1), while the hydrodynamic size was inferred from multi-angle dynamic light scattering (DLS) measurements (ALV/CGS-3 Goniometer, ALV-Gmbh). DLS measurements were executed in the same medium as for the rheological measurements to allow comparison. Table 4.1 summarises the results for the different particles; they are organised based on increasing amount of monomer units in the stabiliser (PMMA-3.8→PMMA-5.5→PMMA-46). Two different measures for the grafted layer thickness are given: a value h_{co} based on the contour length from the number of monomer units [131], and a hydrodynamic thickness h_h adopted from DLS results. With increasing chain length, discrepancies can be seen between the calculated contour length and the effective hydrodynamic layer thickness. The density of the grafted polymer layer reduces with increasing radial distance. Differences can hence be caused by the occurrence of solvent flow in the outer regions of the layer or, to some extent, by the release of constraints on the stiff polymer chains. Note that the PMMA-*g*-46PHSA particles were more polydisperse (figure A.1). Polydispersity will broaden the distribution of relaxation times in the suspension or may alter the non-linear response. However, within the observed range, it is not expected to strongly affect the local interactions near the particle surface.

Particles were dispersed in diisodecyl phthalate (DidP, VWR International), a higher order phthalate with a medium viscosity $\eta_m = 0.084$ Pa·s. The medium was chosen for its compatibility with PMMA-*g*-PHSA and for its rather high viscosity, at least compared to traditional solvents, which benefits the signal strength. Although lower order phthalates were observed to dissolve or swell PMMA particles [133], the model particles were found to be stable in DidP for a long period of time. Furthermore, PMMA particles are not expected to be charged in DidP, and measurements with and without organic salt (TBAC, Sigma-Aldrich) gave similar results. Dispersions of different particle volume fractions were created from stock suspensions by subsequent centrifugation and

redispersion steps. The particles were redispersed through ultrasonication and vortex mixing. Samples of different particle types were compared based on an effective hydrodynamic volume fraction rather than their actual volume fraction; the concentration range that was studied is discussed in section 4.3.2.

Silica suspensions

Silica particles with varying surface roughnesses were used as a second model system. The multi-step synthesis is described in detail by Zanini et al. [132]. Oppositely charged silica nanoparticles are electrostatically adsorbed onto smooth 'core' particles. A smoothing silica layer is additionally grown onto the surface of the raspberry-like particles to fix the asperities and create a homogeneous charge. The roughness can be tuned by varying the extent of the final smoothing layer. Three different particle types were used, ranging from smooth (silica-SM) to increasingly rough (silica-RO). The core size of the bare particles was determined via SEM and information on the asperities was obtained via AFM measurements (NanoWizard NanoOptics, JPK Instruments AG) and analysis of the surface topography [124]. Experimental details of the particles are given in table 4.2; SEM micrographs are shown in appendix A.1.1 (figure A.2). Reducing the thickness of the final smoothing layer enhanced the height of the asperities (silica-RO.4→silica-RO.5) and increased the dimensionless roughness parameter h_a/d_a, the ratio between the height of and distance between the asperities [124]. ζ potential measurements (Zetasizer Nano ZS, Malvern Instruments) were performed on the silica particles dispersed in water and revealed a negative surface charge with a magnitude that agreed with typical values in literature [134].

The silica particles with well-defined surface roughness were dispersed in a mixture of glycerol-water (86 vol% glycerol) with a medium viscosity $\eta_m = 0.144$ Pa·s. The exact composition was matched with the equilibrium composition

Table 4.2: Experimental parameters of the silica particles. a_c is the core particle radius (SEM imaging), h_a the height of the asperities (AFM), and h_a/d_a is the ratio between the height of and distance between asperities. ζ is the zeta potential of the particles in water.

	a_c [nm]	h_a [nm]	h_a/d_a [-]	ζ [mV]
Silica-SM	330	/	/	−52
Silica-RO.4	305	22	0.43	-
Silica-RO.5	300	26	0.54	−56

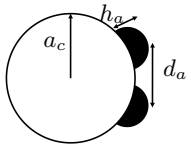

of glycerol-water at the environmental lab conditions to avoid effects of water uptake or drying during the measurements. Note that the ζ potential value in water (table 4.2) can only be used as an indication since the actual surface charge in glycerol-water mixtures may be lower due to a reduced dissociation. Similar to the PMMA-*g*-PHSA dispersions, batches of different concentration were created by subsequent centrifugation and redispersion (see section 4.3.2 for concentration range).

4.2.2 Rheological measurements

Oscillatory rheological experiments were performed over an extended frequency range from $0.001 - 2000$ Hz. A commercial stress-controlled rheometer (MCR 302, Anton Paar) was used to measure the response at frequencies < 20 Hz. Measurements were carried out with 2 different geometries: a 40 mm plate-plate geometry operated at a gap of 150 μm, and a 40 mm cone-and-plate geometry (2° cone angle). Results were the same for both geometries. The strain amplitude was varied between $0.1 - 5\,\%$ to ensure operation within the linear viscoelastic region while maximising the response. Applying a pre-shear did not alter the response for the Brownian suspensions. Both for the low- and high-frequency measurements, the sample was allowed to rest for 5 min after loading. High-frequency measurements were carried out between $20 - 2000$ Hz with our homebuilt piezorheometer (described in chapter 3: figure 3.1). Measurements were carried out at an operating gap of 100 μm and strain amplitude of 0.054 %.

In addition, the rotational stress-controlled instrument was used in combination with a cone-and-plate geometry for non-linear rotational measurements. Stress ramps were performed between $0.01 - 10^4$ Pa, and both the resulting shear rates and normal stresses were recorded. The measurement time was varied over the ramp so that the equilibrium structure could be probed at each value of stress.

4.3 Results and discussion

4.3.1 Rheological behaviour of the model system

This section serves to illustrate the rheological behaviour of the model systems. Two examples are given: a suspension of PMMA-*g*-5.5PHSA particles and of smooth silica particles, both evaluated at $\phi_{eff} = 0.43$. Note that ϕ_{eff} is based on the effective hydrodynamic volume fraction of the particles in the suspension, and is clarified in section 4.3.2.

Figures 4.1 − 4.2 show the linear viscoelastic moduli, phase angle and real part of the complex viscosity ($\eta' = G''/2\pi f$) over an extended frequency range for a PMMA-5.5 and silica-SM suspension, respectively. The prepared dispersions generally displayed a Maxwellian-like behaviour, and distinct regions can be identified in the frequency response. The location of these regions depends on the characteristic relaxation time or distribution of relaxation times, and is governed by the diffusive response of the particles (equation 1.13). Generally, for the suspensions considered, the microstructure is able to relax completely at very low frequencies and the dispersions inherently behave as fluids. Elastic contributions are negligible and the phase angle is close to 90°. However, the applied deformation has to work against the relaxation mechanism and full potential, resulting in an increased energy dissipation and low-frequency viscosity η'_0. In this terminal region, the moduli scale with $G' \propto f^2$ and $G'' \propto f$. At increasing frequency, when approaching the characteristic frequencies of relaxation processes, the suspensions are increasingly unable to relax under the applied oscillation. On one hand, this leads to elastic contributions or a decrease in phase angle while on the other, the resulting reduction in energy dissipation induces a thinning behaviour or decrease in η'. The phase angle goes through a minimum before increasing again towards 90° at even higher frequencies. A 2nd terminal region can be identified in which the energy dissipation through the medium dominates the response. The slope of G'' evolves to 1, parallel to that of the medium, while the elastic modulus G' only contains direct contributions from the interparticle interactions [3].

For both types of suspensions, a relatively high medium viscosity was chosen. This has two important consequences. Relaxation processes are slowed down, and the low-frequency terminal regime is generally outside of the frequency window probed here (figures 4.1 − 4.2). The relevant characteristic relaxation times for the concentrated suspensions is discussed in section 4.3.3. Furthermore, viscous contributions generally dominated the response at frequencies > 1 Hz, resulting in phase angles close to 90° and a reduced accuracy on the elastic stress contributions (section 3.2.3). The examples shown here are representative for the behaviour of the other batches as well. It must be realised that the exact magnitude of the moduli depends on the concentration and interaction forces present in the suspensions. For instance, low-frequency moduli were somewhat higher for the PMMA-3.8 suspensions compared to PMMA-5.5 and -46 batches, potentially due to a reduced shielding of attractions for thin stabilisation layers.

The high-frequency viscosity evolves to a constant limiting value η'_∞ (figures 4.1 − 4.2, for $f > 10^2$ Hz) which arises from hydrodynamic contributions only. The presence of particles distorts the flow field and increases the energy dissipation. Hence, η'_∞ only depends on the medium viscosity η_m and the effective hydrodynamic volume fraction occupied by the particles. Note that

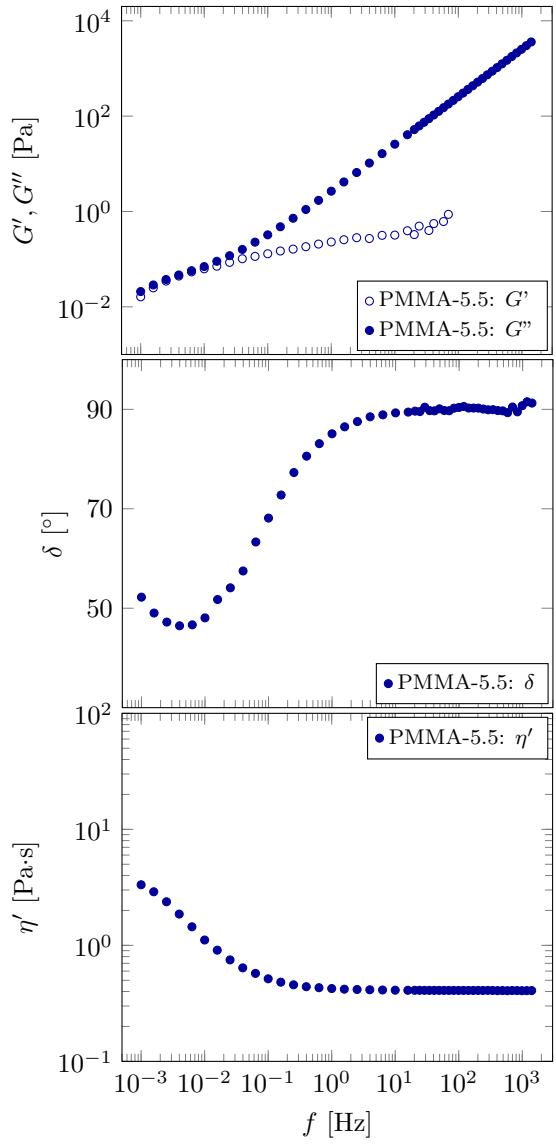

Figure 4.1: Examples of linear viscoelastic moduli, phase angle and complex viscosity for PMMA-*g*-5.5PHSA dispersed in diisodecylphthalate ($\phi_{eff} = 0.43$).

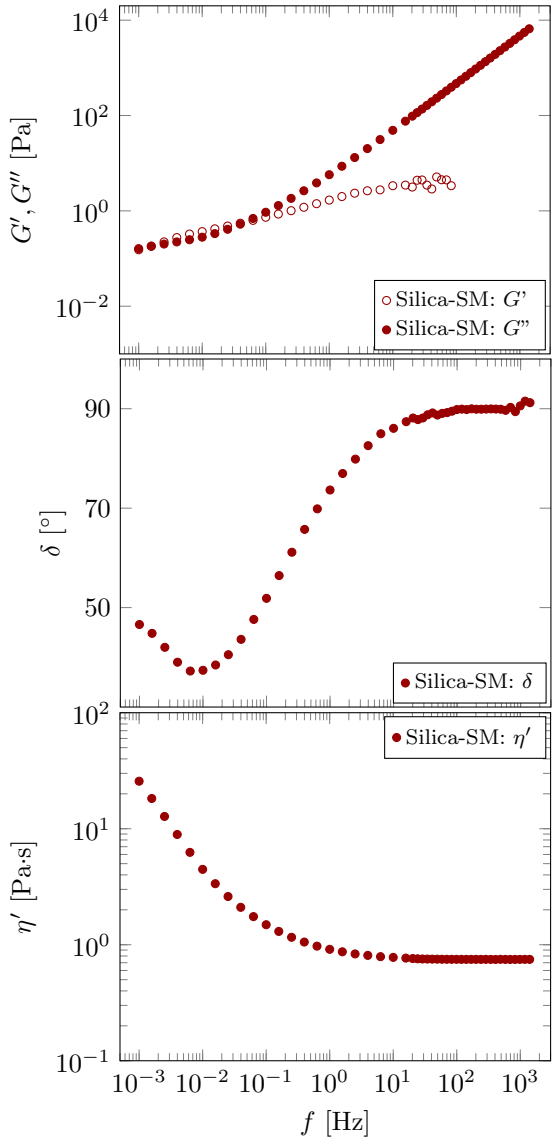

Figure 4.2: Examples of linear viscoelastic moduli, phase angle and complex viscosity as a function of frequency for smooth silica particles dispersed in glycerol-water ($\phi_{eff} = 0.43$).

this volume fraction is not necessarily based on geometric aspects of the particles, but relates to the amount of immobilised volume within the suspension. In chapter 5, this term will be used to obtain structural information on the colloidal building blocks in a dispersion.

4.3.2 Comparison based on ϕ_{eff}

Both the PMMA and silica suspensions were measured at different volume fractions. The suspensions were generally prepared based on the sample weight and core density of the particles. However, since the surface topologies of both particle types were varied in different manners, choosing the relevant volume fraction for comparison is less trivial. Using the volume fraction based on the core density ignores the effect of the various surface characteristics. Taking into account specific topological parameters, such as the thickness of the grafted polymer layer or height of the asperities (tables 4.1 − 4.2), is an option but might fail to describe the subtle differences in hydrodynamic interactions near the surfaces. In this work, the effective volume fraction ϕ_{eff} is derived from the limiting HF viscosity η'_{∞} (figures 4.1 − 4.2). The resulting effective hydrodynamic volume fraction directly relates to the hydrodynamic stresses induced by the added particles, and is hence more suited as a basis for comparing the stress contributions in different suspensions.

Figure 4.3 illustrates the proposed method for the PMMA and silica suspensions. The relative HF viscosities $\eta'_{rel,\infty} = \eta'_{\infty}/\eta_m$ are plotted as a function of the (core density) volume fraction for the different particle types. Measured values are compared with a hydrodynamic viscosity model derived by Sierou and Brady [135], which takes into account both long-range interactions and lubrication effects. An analytical fit to the model was provided by Cheng et al. [136] and is plotted in figure 4.3:

$$\eta'_{rel,\infty} = \frac{1 + \frac{3}{2}\phi[1 + \phi(1 + \phi - 2.3\phi^2)]}{1 - \phi[1 + \phi(1 + \phi - 2.3\phi^2)]}\,. \tag{4.2}$$

Experimental values for the PMMA-3.8 and silica-SM suspensions agree well with predicted values. When increasing the thickness of the grafted polymer layer or size of the asperities, the measured high-frequency viscosities become increasingly underestimated. The reason for this discrepancy is an underestimation of the effective size of a particle. Hence, the effective hydrodynamic volume fraction ϕ_{eff} for the different suspensions is determined by shifting the measured values horizontally towards the model fit, as indicated by the arrows in figure 4.3.

As an illustration, figure 4.4 compares the evolution of $\eta'_{rel,\infty}$ when using an effective volume fraction based on topological parameters of the particle

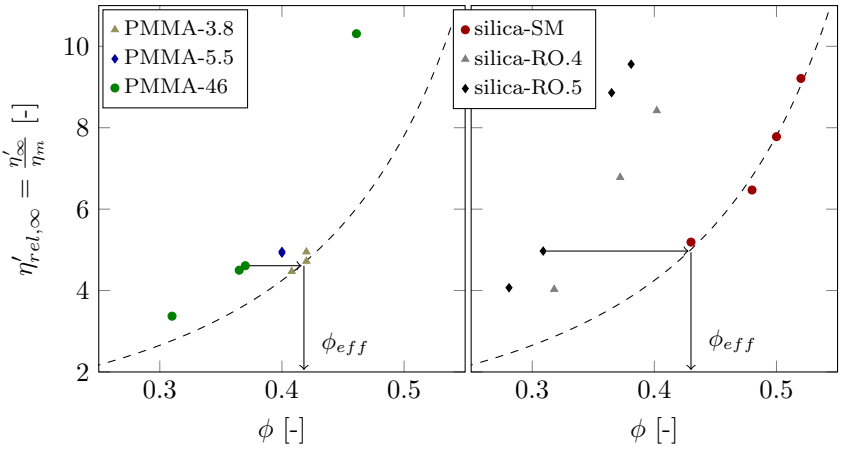

Figure 4.3: Relative viscous moduli in the high-frequency limit as a function of the volume fraction ϕ. (left) PMMA suspensions; (right) silica suspensions. The dashed line represents a model fit valid for suspensions undergoing purely hydrodynamic interactions [135].

surfaces $\phi_{eff,h}$. In case of the PMMA suspensions, $\phi_{eff,h}$ was calculated based on $\phi_{eff,h} = \phi(1 + \frac{h_h}{a_c})^3$ [3], with a_c the core radius and h_h the hydrodynamic thickness of the grafted layer obtained from DLS measurements (table 4.1). The rescaled data agree well with the model fit. DLS probes a hydrodynamic size of the particles through their diffusivity at infinite dilution, and relates to the HF hydrodynamic volume fraction. It must be realised that for the softer PMMA-46 particles, this relationship is not necessarily valid over a larger concentration range. For the silica suspensions, $\phi_{eff,h}$ was calculated from $\phi_{eff,h} = \phi(1+\frac{h_a}{a_c})^3$, with h_a the height of the asperities. By using $\phi_{eff,h}$, experimental values are shifted closer to the predicted values but are still underestimated by the model. A simple rescaling based on the geometrical size of the asperities does not fully capture the complex changes in hydrodynamic stresses that are induced by the asperities. Note that in the following sections, measurements on different particle types are compared based on ϕ_{eff} as proposed in figure 4.3.

4.3.3 Method for rescaling the stresses

The previous section introduced a framework to effectively compare volume fractions for different types of suspensions. However, their rheological behaviour is determined by the interaction potential as well as by the concentration, and in

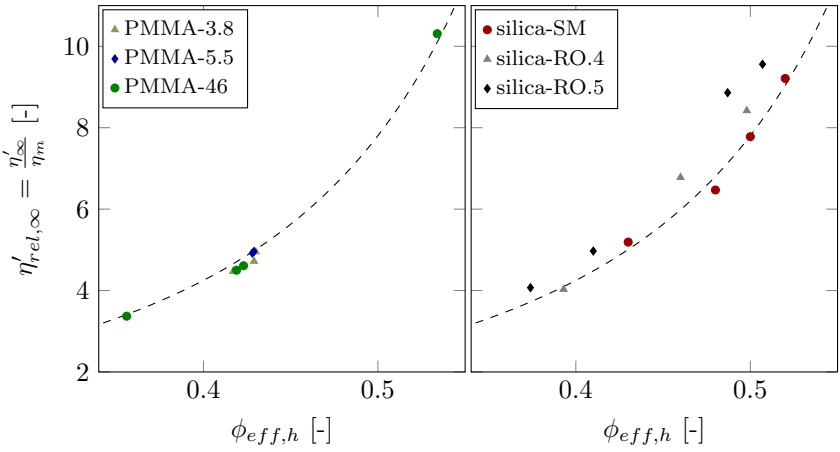

Figure 4.4: Relative viscous moduli in the high-frequency limit as a function of an effective volume fraction based on topological aspects of the particles for PMMA and silica suspensions. The dashed line represents a model fit valid for suspensions undergoing purely hydrodynamic interactions [135].

order to compare the stress contributions for the various suspensions on the same basis, the rheological data (figures 4.1 − 4.2) needs to be rescaled. The rescaling is demonstrated for the silica-SM suspensions at varying concentrations.

The transition between different regimes in the frequency response of the suspensions depends on their respective relaxation times. A first rescaling aims at evaluating the stresses within the characteristic frequency window of the material rather than the absolute measurement frequency. The relevant diffusional relaxation time τ_p for concentrated colloidal suspensions has been the subject of several investigations [103, 126, 137]. The particle mobility is reduced compared to infinite dilution, and τ_p was found to scale best with the short time self-diffusion coefficient $\mathcal{D}_{ss}$:

$$\tau_p = \frac{a^2}{\mathcal{D}_{ss}} = \frac{6\pi\eta'_\infty a^3}{k_B T} = \frac{1}{2\pi f_{char}}, \tag{4.3}$$

with $k_B T$ the thermal energy scale and f_{char} the characteristic relaxation frequency. This expression is similar to that for infinite dilution, but uses the effective hydrodynamic viscosity η'_∞ rather than the medium viscosity η_m. Non-idealities such as polydispersity or local density differences broaden the relaxation spectrum. Furthermore, colloidal interactions inherently alter the viscoelastic response and time scales in the suspension. Electrostatic repulsive interactions were observed to complicate the scaling between $\mathcal{D}_{ss}$ and η'_∞, leading

to an overestimation of τ_p [137]. Attractive interactions can add additional relaxation mechanisms and shift the entry into the high-frequency region to larger values [138]. Despite these complexities, equation 4.3 delivers the most physically relevant basis for rescaling the frequency, and stress contributions are plotted here as a function of the dimensionless variable $\alpha = 2\pi f \cdot \tau_p$. The particle radius a was approximated by taking into account the topological parameters of the surface, with $a = a_c + h_h$ for the PMMA suspensions and $a = a_c + h_a$ for the silica suspensions (tables 4.1 − 4.2). Equation 4.3 also sets the length scale under investigation, since τ_p describes the time needed for a particle to travel a distance similar to its own size. This diffusional boundary layer decreases further with frequency, so that localised stresses around the particle surface are probed.

Second the rescaling of the stress contributions, given by the measured moduli G' and G'', is considered. The total deviatoric suspension stress was given by equation 4.1. The hydrodynamic terms $(2\eta\dot{\boldsymbol{\epsilon}} + \boldsymbol{\Sigma}^H) = 2\eta'_\infty\dot{\boldsymbol{\epsilon}}$ are responsible for the high-frequency viscosity and only represent dissipation from the applied flow. Hence, to highlight the particle contributions in the diffusional boundary layer around the surface, the purely hydrodynamic contributions must be subtracted from the measured loss modulus G''. In addition, the stresses are non-dimensionalised by dividing the measured moduli with the medium viscosity η_m evaluated at $\alpha = 1$, resulting in reduced moduli that contain contributions of both the particle size a and effective volume fraction ϕ_{eff}.

Figure 4.5 respectively shows the resulting reduced loss (a) and elastic (b) moduli for the silica-SM suspensions at different ϕ_{eff}. The suspensions display a similar behaviour over the concentration range considered, and different regions can be identified. The low-frequency terminal region, occurring at dimensionless frequencies $\alpha < 1$ and for which $G'' \propto \alpha^1$ and $G' \propto \alpha^2$, was outside of the accessible frequency window. In the thinning regime (figure 4.1), the slopes decrease and at measurement frequencies $\alpha < 10^4$, both contributions can be seen to increase only weakly with frequency. The high-frequency terminal regime is only reached here for $\alpha \geq 10^4$, while simulations on Brownian particles predicted a limiting HF behaviour from $\alpha > 1$ [127]. Potential discrepancies can be caused by the presence of charges, attractive van der Waals interactions or local density differences. In the HF region, the displacement decreases to an extent that the diffusional boundary layer falls within the lubrication layer between the particles. The asymptotic behaviour indicates a regime for which lubrication stresses dominate: the loss contributions suddenly drop and scale with $O(\alpha)^{-1}$ while the elastic contributions reach a plateau value. These results are in good agreement with experimental data from Shikata and Pearson [103] on silica particles dispersed in ethylene glycol, who reported a similar scaling behaviour at $\alpha > 10^2 - 10^3$.

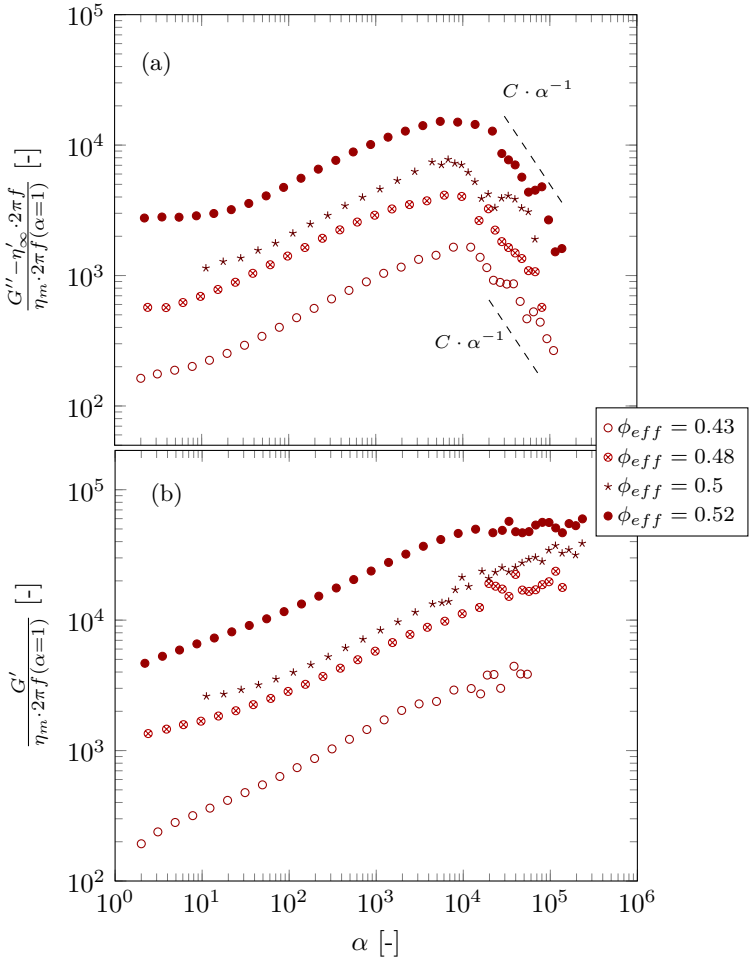

Figure 4.5: Reduced viscous (a) and elastic (b) moduli of silica-SM suspensions at different concentrations. The high-frequency asymptotic loss moduli are fitted with the hydrodynamic function $C \cdot \alpha^{-1}$; the fitting parameter C varies between $2.5 - 25 \cdot 10^7$ from the lowest ($\phi_{eff} = 0.43$) to the highest ($\phi_{eff} = 0.52$) concentration.

The reduced moduli in figure 4.5 only contain Brownian and interparticle contributions (equation 4.1). Their behaviour is generic, but the magnitude increases with concentration. In general, the particle induced stresses depend on the concentration and interparticle interactions in a non-trivial manner, and further rescaling is required to allow direct comparison between the different suspensions. The low-frequency limiting viscosity η_0' contains information on the total interparticle potential and is typically used to rescale the stresses [127] but is outside the measurable frequency range for the suspensions considered. Instead, a rescaling based on the reduced modulus in the high-frequency asymptotic region is suggested. The local particle interactions govern the asymptotic response of both the elastic and viscous stress components [126]. Since the measured phase angle was close to 90° at higher frequencies (figures 4.1 − 4.2), the more accurately measured loss modulus G'' was used here for the rescaling. The approach is illustrated in figure 4.5 (a). Experimental values in the HF region are fitted with the function $C \cdot \alpha^k$, with k the exponent of the asymptotic viscous stresses. In this case $k \approx -1$, indicating a purely hydrodynamic lubrication function. The prefactor C is subsequently used to rescale the viscous and elastic components, resulting in the reduced stresses $\Sigma_{v,r}$ and $\Sigma_{e,r}$:

$$\Sigma_{v,r} = \frac{1}{C} \cdot \frac{G'' - \eta_\infty' \cdot 2\pi f}{\eta_m \cdot 2\pi f(\alpha = 1)}, \tag{4.4}$$

$$\Sigma_{e,r} = \frac{1}{C} \cdot \frac{G'}{\eta_m \cdot 2\pi f(\alpha = 1)}. \tag{4.5}$$

The prefactor C only influences the magnitude without affecting the actual shape of the curve. Results for the different types of suspensions are discussed in section 4.3.4.

4.3.4 Analysis of the stress contributions

PMMA suspensions

The reduced elastic and viscous stresses are presented in figure 4.6 for the PMMA-3.8 (a), PMMA-5.5 (b) and PMMA-46 (c) suspensions at $\phi_{eff} \approx 0.43$. For $\alpha < 200$ the PMMA suspensions behave similar to the silica-SM samples at intermediate frequencies (figure 4.5), with stresses increasing weakly with frequency. However, the entry into the high-frequency terminal regime occurs at lower frequencies ($\alpha > 200$ vs $\alpha > 10^4$), which may be attributed to the presence of electrostatic interactions in the silica suspensions [137]. At frequencies $\alpha > 200$, the PMMA suspensions in figure 4.6 show a remarkably

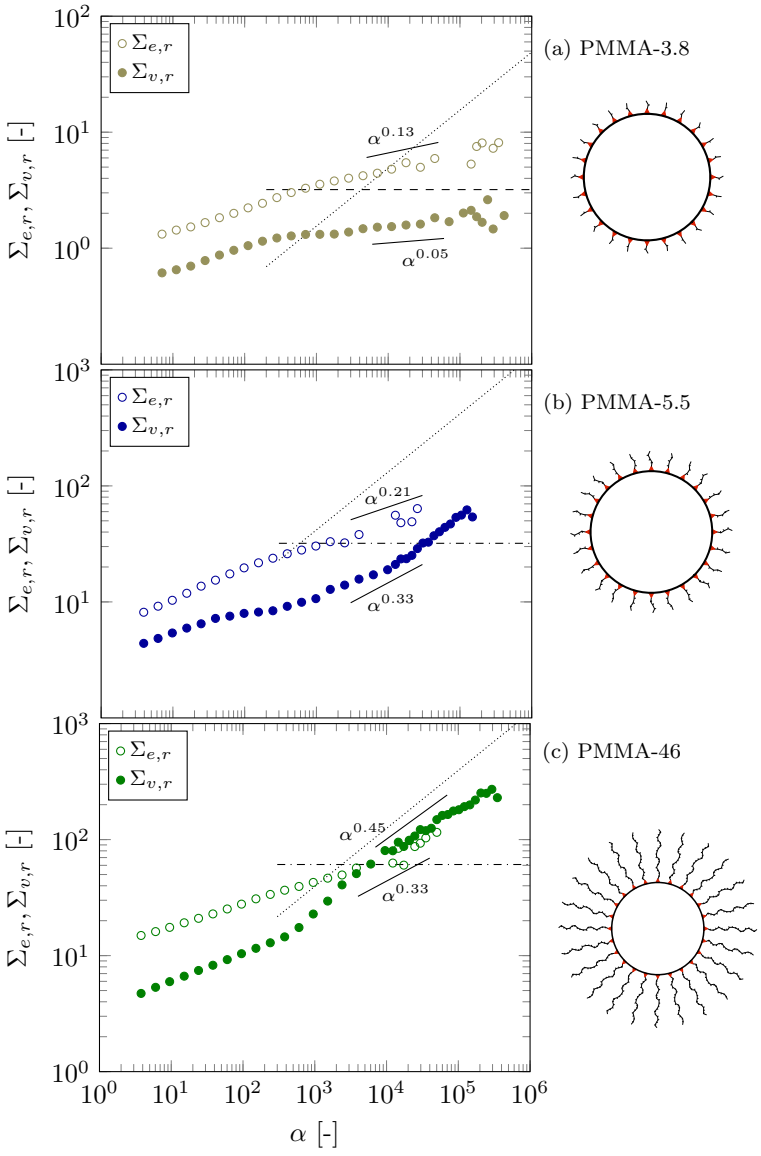

Figure 4.6: Reduced stresses for PMMA particles with different stabilisation layer thicknesses dispersed in DidP. Comparison of viscous and elastic stress contributions at $\phi_{eff} \approx 0.43$ for PMMA-3.8 (a), PMMA-5.5 (b) and PMMA-46 (c). The experimental high-frequency scaling is indicated by full lines. Dashed, dotted and dashed-dotted lines present model predictions for $\Sigma_{e,r}$ based on lubrication, hard-sphere and polymer-polymer interactions, respectively.

different asymptotic behaviour depending on the thickness of the stabilisation layer. The reduced stresses reveal the complex interplay between hydrodynamic lubrication interactions and repulsive interactions between the grafted polymers. With increasing stabilisation layer thickness, the scaling exponent of the reduced stresses steadily rises, indicating an increased shielding of the lubrication interactions through the polymer layer and an enhanced relative particle diffusivity.

It is insightful to compare the results in figure 4.6 with numerical data from Swan et al. [127], in which the effect of lubrication shielding was simulated at semi-dilute conditions by means of an excluded annulus model. Lubrication interactions slow down the relative motion of particles and lead to smaller stresses. Hence, in the limit where lubrication interactions dominate the HF response, the diffusional boundary layer was found to decay rapidly ($O(\alpha^{-1})$), resulting in decreasing viscous stresses ($\Sigma_{v,r} \propto O(\alpha^{-1})$) and an elastic stress plateau ($\Sigma_{e,r} \propto O(\alpha^{0})$). On the other hand, in the absence of lubrication forces, particles only interacted through a hard-sphere repulsion at contact, leading to normal modes and a similar scaling for both in- and out-of-phase stress components: $\Sigma_{v,r}$, $\Sigma_{e,r} \propto O(\alpha^{1/2})$. The deviation from the lubrication scaling was found to be very sensitive to the size of the excluded annulus, especially in the presence of even small attractions [138]. These findings confirm the experimentally observed reduction in lubrication interactions with increasing stabilisation layer thickness. Interestingly even for the PMMA-3.8 suspensions the scaling deviates from the lubrication regime, which was for instance observed for the silica-SM suspensions (figure 4.5).

Although the excluded annulus model is useful to identify the limits of lubrication shielding, it does not capture the actual behaviour in the stabilisation layer. The hydrodynamic interactions inside the polymer brush are complex functions of the radial distance and are influenced by parameters of the grafted layers, such as the chain length and permeability [130, 139]. Furthermore, the change of potential between polymer layers upon compression must be accounted for [140]. This complex interplay is illustrated when plotting the reduced viscous stresses $\Sigma_{v,r}$ for the PMMA-46 suspensions at different ϕ_{eff} (figure 4.7). Unlike the silica-SM suspensions (figure 4.5), PMMA-46 batches at different concentrations do not show a generic behaviour. The slope of the asymptotic behaviour decreases with particle concentration and implies a change in the stress mechanism. With increasing volume fraction, the grafted chains become more compressed, leading to a reduced permeability inside the brush. As shown by simulations from Elliott and Russel [140], reducing the permeability enhances the hydrodynamic stresses near the brush surface, and hence decreases the slope of $\Sigma_{v,r}$. Note that at very high frequencies, the softness of the brush itself might come into play as well. The 1st relaxation mode of a 46PHSA strand in free suspension

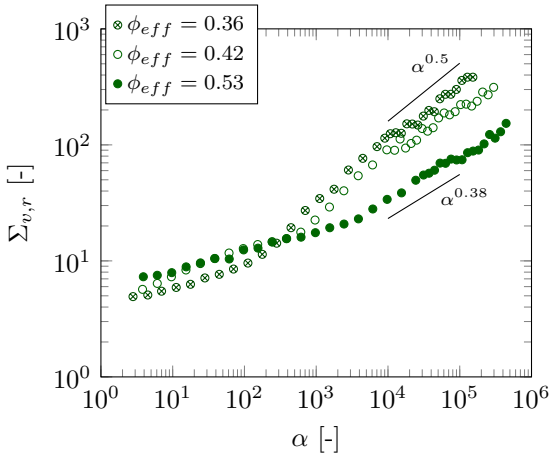

Figure 4.7: Failure of the universal scaling behaviour of the reduced viscous stress $\Sigma_{v,r}$ for the PMMA-46 suspensions at different volume fractions. The scaling exponent varies from ~ 0.38 to ~ 0.5.

can be approximated via the Rouse relaxation time and occurs at ~ 50 kHz, which is higher than the frequency window considered here. The results for the different concentrations illustrate the sensitivity of the high-frequency response to the subtle differences in the local stresses arising near the particle surface.

The magnitude of G'_∞ is directly related to the interparticle potential and can for instance be used to obtain information on the strength of interaction [11]. Here, the relationship is used in a reverse manner to predict and validate the measured values. Model predictions were determined by taking into account single mechanisms either from lubrication stresses, hard-sphere repulsions or repulsive interactions between polymer brushes. The different models are reported in appendix A.1.2. The reduced elastic stresses $\Sigma_{e,r}$ were determined from the calculated high-frequency moduli G'_∞ in the same manner as for the experimental values and are shown in figure 4.6. The magnitude of the predicted HF stress contributions agree qualitatively with measured values. Calculations based on lubrication interactions or interactions between polymer brushes predict a plateau modulus, while the hard-sphere repulsive model predicts a HF modulus that scales with $\propto \alpha^{1/2}$. Important to realise is that the hard-sphere repulsive interaction only presents a theoretical limit: effectively shielding lubrication interactions by a thick grafted layer also results in a softer polymer brush which will change the nature of the repulsive interaction. Evidently, the actual behaviour in the grafted polymer layer is much more complicated and in order to accurately calculate the high-frequency asymptotic stresses, more rigorous

numerical simulations are required. Nonetheless, predictions based on these single-mechanism models prove good indicators to delineate the asymptotic behaviour.

Silica suspensions

Figure 4.8 compares the reduced viscous stresses for the smooth and rough silica suspensions at different concentrations. As discussed in section 4.3.3, the silica-SM samples display a generic behaviour and reducing the stresses based on the asymptotic HF region ($\alpha > 10^4$) shifts the curves on top of each other over the entire range. For the rough particle suspensions, this is no longer the case: there exists a concentration dependent intermediate region ($\sim 10^4 - 10^5$) for which $\Sigma_{v,r}$ increases and scales with $\propto \alpha^1$. Hence, in this region, the decrease in diffusional boundary layer does not influence the stress response. Eventually, the stresses reach a peak value and drop to a lubrication scaling ($\Sigma_{v,r} \propto O(\alpha^{-1})$) in an asymptotic regime at even higher frequencies. This hydrodynamic scaling occurs when the diffusional boundary layer falls within the lubrication layer between the particles, indicating that the intermediate regime, at slightly larger length scales, probes the added topological effect of the asperities. This is confirmed by the dependency of the scaling on both roughness and concentration. The prefactor of the hydrodynamic function $C \cdot \alpha^{-1}$, used to reduce the stresses via equation 4.4, is inserted in figures 4.8 (a) − (c) and generally increases as a function of ϕ_{eff}. Comparing C for the different suspensions indicates that the peak value shifts to larger α and stresses as a function of roughness, while the intermediate regime becomes broader. Furthermore, with increasing concentration, the extent of this regime decreases and is shifted to larger α as well. Rescaling the viscoelastic spectrum based on the asymptotic regime and single characteristic relaxation process is not able to capture the additional length scale from the asperities. Both with increasing roughness and concentration, interparticle length scales decrease and result in larger α.

A similar trend can be observed for the reduced elastic stresses $\Sigma_{e,r}$ (figure 4.9). However, they display more scattering due to the reduced accuracy of G' at large phase angles (figure 4.2). For the silica-SM samples, $\Sigma_{e,r}$ evolves towards a high-frequency lubrication plateau at $\alpha > 10^4$. Both silica-RO samples evolve towards a lubrication plateau as well but the onset is shifted to higher α, while an intermediate regime appears to be present at $\alpha \sim 10^4$ where stresses rise, corresponding to $\Sigma_{v,r}$. Figures 4.9 (b) and (c) imply that the temporary increase of the elastic stresses is again more extended with increasing roughness. Plateau values are compared with model predictions for G'_∞ based on the lubrication approximation of Lionberger and Russel [102] (equation A.1),

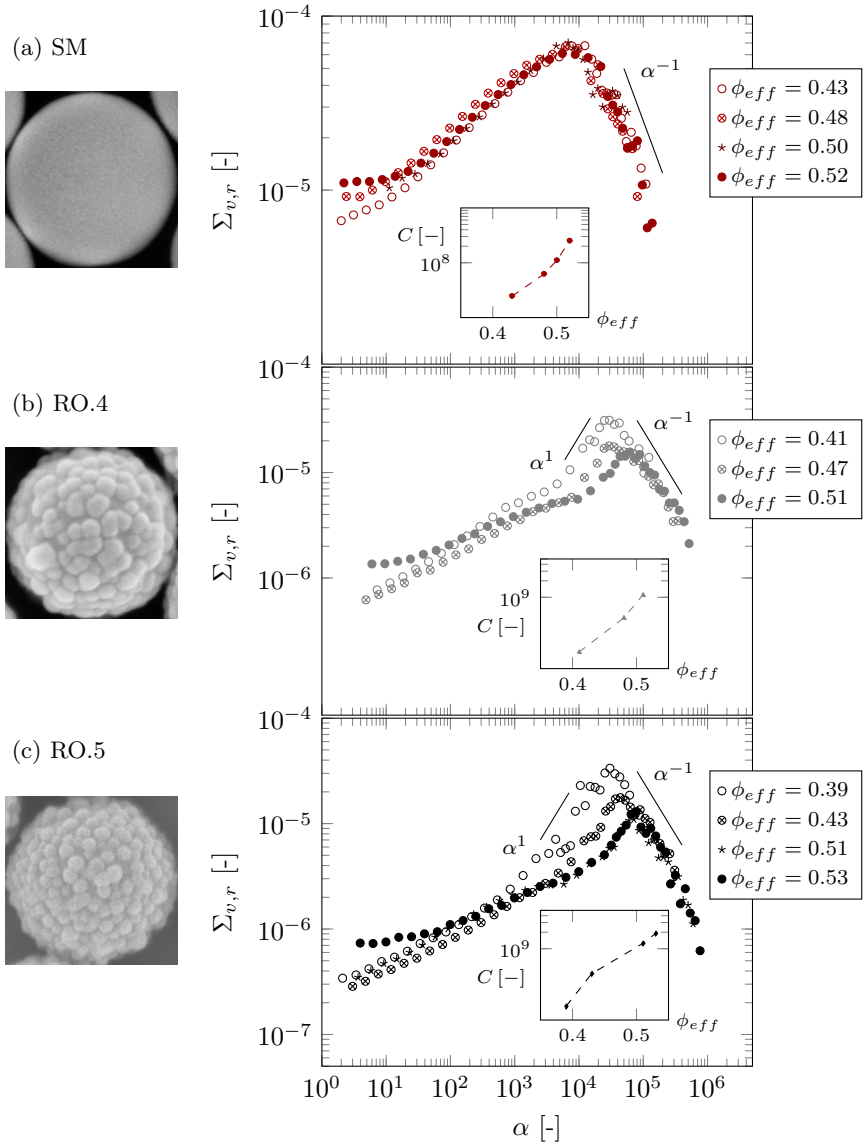

Figure 4.8: Volume fraction dependency of the reduced viscous stresses as a function of reduced frequency for silica particles with increasing roughness: from smooth (a) to $h_a/d_a \approx 0.43$ (b) and $h_a/d_a \approx 0.54$ (c). Inserted figures show the evolution of the prefactor C for the hydrodynamic scaling with concentration ϕ_{eff}.

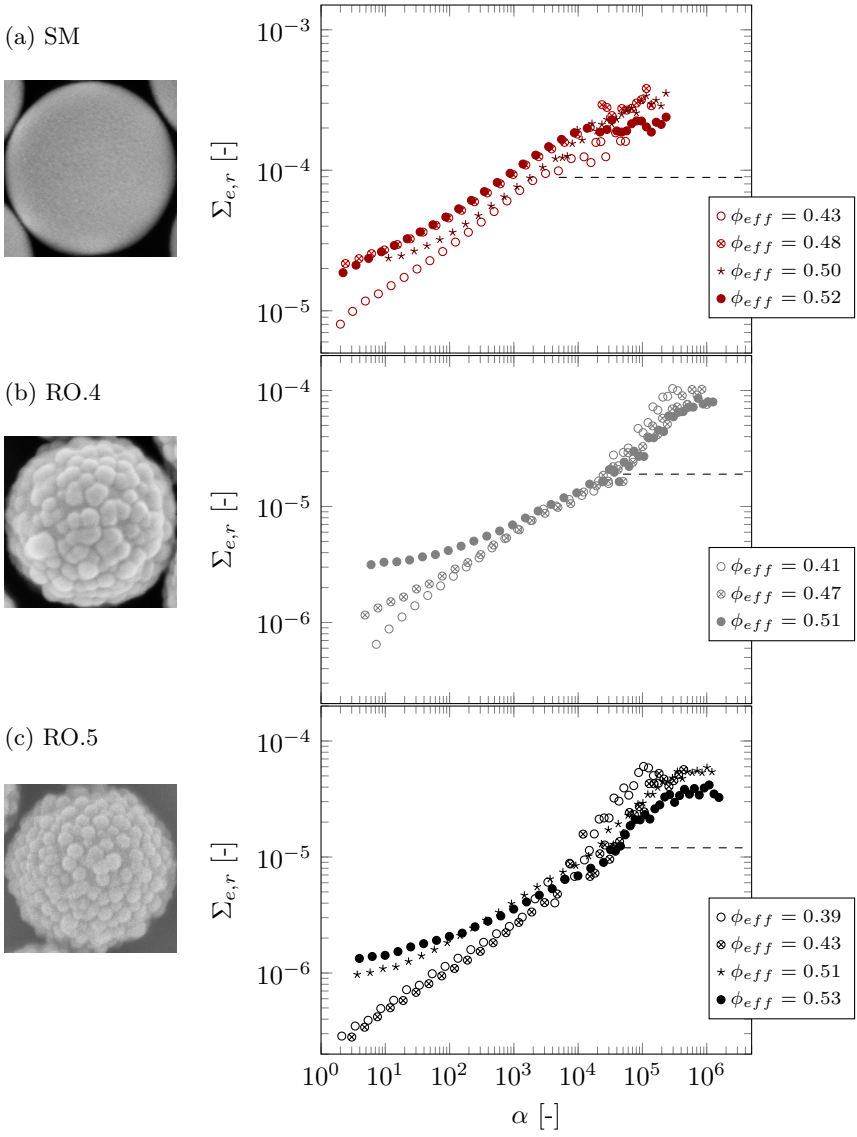

Figure 4.9: Volume fraction dependency of the reduced elastic stresses as a function of reduced frequency for silica particles with increasing roughness: from smooth (a) to $h_a/d_a \approx 0.43$ (b) and $h_a/d_a \approx 0.54$ (c). The dashed lines indicate model predictions for the plateau value of $\Sigma_{e,r}$ in the lubrication regime (equation A.1).

which somewhat underestimate the measured values for all suspensions. The reason might stem from uncertainties in the data or model predictions, but can also be caused by the added presence of electrostatic repulsive interactions. The HF modulus stemming from electrostatic interactions can be calculated based on the interaction potential in a similar manner as for sterically stabilised spheres [11, 141] (appendix A.1.2). The modulus can only be guessed due to the uncertainty on the exact surface charge in glycerol-water (table 4.2), and fits with experimental values for a surface potential $\zeta \approx -20$ mV and for larger Debye lengths ($\kappa^{-1} \approx 50$ nm).

4.3.5 Shear thickening behaviour

The discussion above elaborated on the stress contributions when suspensions are near-equilibrium. In this section the non-linear response, and more specifically the shear thickening behaviour, is presented. Although the behaviour is expected to be influenced by the surface topology as well, suspensions are far away from their equilibrium structure and the effects are not necessarily the same.

PMMA suspensions

Figure 4.10 (a) compares the shear thickening behaviour of the different PMMA suspensions at $\phi_{eff} \approx 0.43$. The viscosity, reduced with the critical onset value η_{cr}, is plotted against the reduced stress $\sigma_r = \frac{\sigma a^3}{k_B T}$, which removes the effect of particle volume and rescales with the thermal energy [3]. Below the critical stress $\sigma_{r,cr}$ ($\eta/\eta_{cr} = 1$), suspensions show a thinning region. The reduced stress does not rescale the data universally in this region and viscosities are significantly higher for the PMMA-3.8 suspensions. As noted in section 4.3.1, low-frequency values of the linear viscoelastic moduli were found to be higher as well and a potential cause may be the reduced shielding of attractive interactions [142].

Above $\sigma_{r,cr}$, the viscosity increases and suspensions display shear thickening. An important observation is the reduction in the viscosity increase for the PMMA-46 suspension compared to the PMMA-3.8 and -5.5 samples. The difference originates from the nature of shear thickening in colloidal suspensions, which occurs as a result of strong lubrication forces that arise in the thin boundary layer between particles that are in close proximity [115, 143]. This hydrodynamic nature can be confirmed via the first normal stress difference: $N_1 = \sigma_{xx} - \sigma_{yy}$, which represents the difference between stresses in the flow and gradient directions. Lubrication forces act to keep particles within close proximity in the extensional quadrant of the flow [144], resulting in a contraction and negative N_1. This can indeed be observed in figure 4.10 (b) for larger stress

levels, with $N_1 < 0$ and an increased probability of finding particles towards the aft direction in the boundary layer. Similar to the high-frequency response in figure 4.6, the shear thickening behaviour is sensitive to the properties of the polymer brush [116]. For long brushes, these are not necessarily constant at high stress levels. However, it can be concluded that by effectively shielding the lubrication interactions between colloidal particles the extent of shear thickening can be reduced.

Silica suspensions

The local near-equilibrium stress contributions studied in section 4.3.4 (figures 4.8 − 4.9) showed an influence of the topological effects from well-defined asperities, but illustrated that lubrication interactions cannot be ignored at very small length scales near the particle surface. Here, the effect of the asperities on the non-equilibrium properties and shear thickening behaviour is studied. Figure 4.11 compares the behaviour for varying roughnesses at two distinct effective volume fractions: $\phi_{eff} \approx 0.42$ and ≈ 0.52. Smooth particle suspensions generally showed an increased thinning behaviour, which is in accordance to findings by Hsu et al. [124]. Note that for the lower volume fractions, the onset of shear thickening occurred at higher reduced stresses compared to the PMMA suspensions (figure 4.10), owing to the presence of surface charges which act to prevent particles from approaching closely [115]. The viscosity curves in figure 4.11 (a) show that with increasing ϕ_{eff}, the shear thickening behaviour changes from a continuous shear thickening state, with only a few fold increase in viscosity and weak scaling with σ_r, to a discontinuous thickening state, for which the viscosity increases orders of magnitude and is found to scale with $\eta \propto \sigma_r^1$ [119].

Although these results show that a discontinuous state can be reached both for smooth and rough particles, the stress mechanisms causing the shear thickening behaviour appear to change. For silica-RO.4 and -RO.5 suspensions, the critical onset stress for shear thickening $\sigma_{r,cr}$ decreases to lower values with concentration (figure 4.11 (a)). This was attributed to the presence of strong tangential interactions that are responsible for the viscosity increase [120]. Furthermore, N_1 switches from negative to positive values (figure 4.11 (b)), which indicates a transition to a dilatant suspension and a shift in the pair probabilities towards the fore direction. The suspension tries to expand in order to find direct flow paths for the particles. Hence, at sufficiently high ϕ_{eff}, the surface asperities give rise to strong tangential forces and increase the probability of finding particles in the compressional quadrant of the flow. It must be realised that figure 4.10 compares the behaviour based on the effective volume fraction, while the actual volume fraction of rough particles is much lower [124].

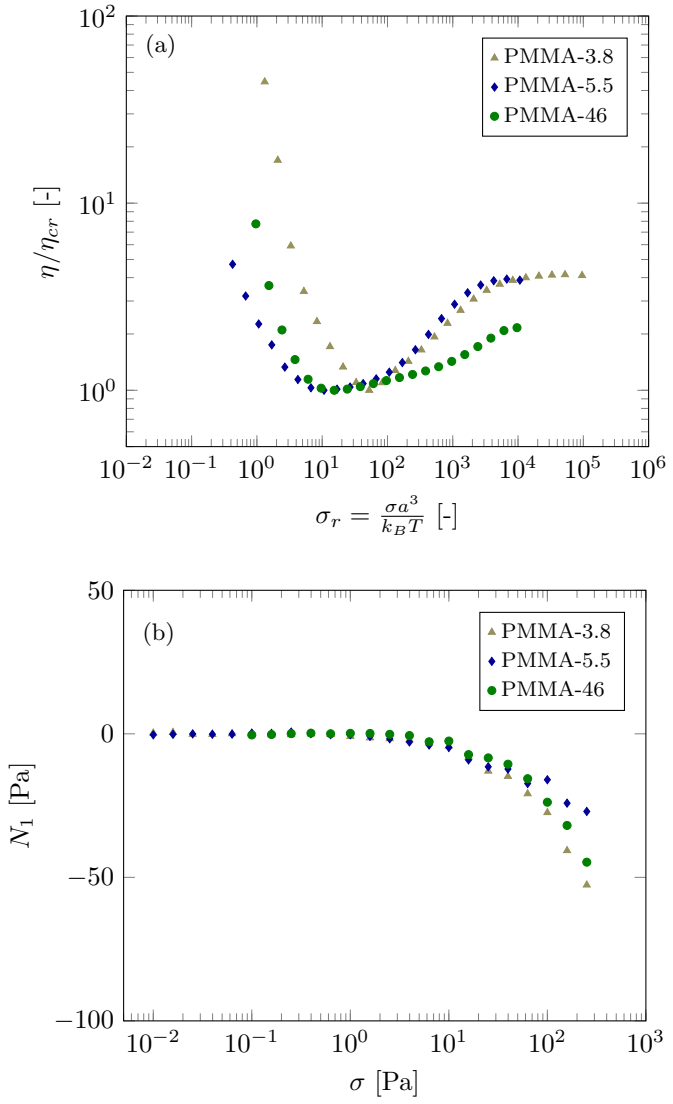

Figure 4.10: Shear thickening behaviour during stress ramps at $\phi_{eff} = 0.43$ for the different PMMA suspensions. (a) Reduced viscosity as a function of reduced stress. (b) First normal stress difference as a function of stress.

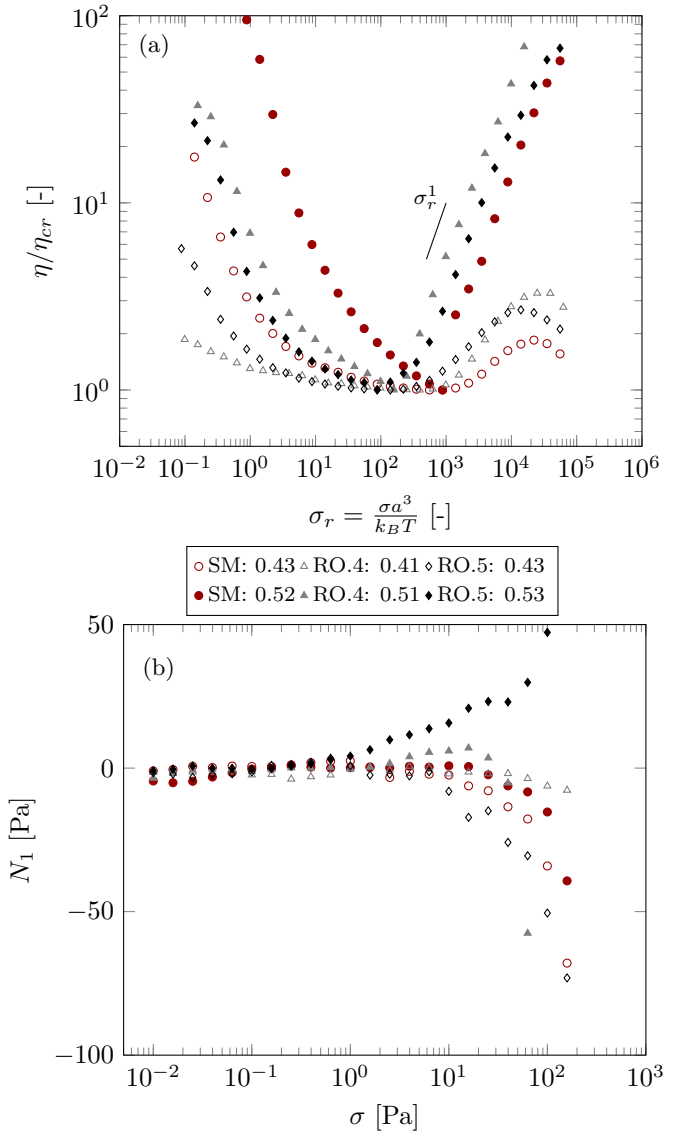

Figure 4.11: Shear thickening behaviour during stress ramps at different ϕ_{eff} for the different silica suspensions. (a) Reduced viscosity as a function of reduced stress. (b) First normal stress difference as a function of stress.

4.4 Conclusions

In this chapter, an experimental study was presented on the interplay between particle surface topology, interaction forces and local stress contributions acting in suspensions. High-frequency rheology was used to probe the suspensions directly at length scales near the particle surface. Different types of model particles were used, ranging from sterically stabilised PMMA particles with a grafted polymer brush to raspberry-like silica particles with well-controlled surface roughness. For particles with varying surface topology, choosing the relevant volume fraction for comparison is not trivial. In this study, the suspensions were compared based on an effective volume fraction from the high-frequency limiting viscosity, or based on their direct effect on the hydrodynamic stresses. A subtle interplay between surface topology, nature of interaction forces and local stress contributions was revealed. For instance, for the PMMA suspensions, the thickness and permeability of the polymer brush dictated the interplay between lubrication interactions and repulsions between polymer layers. Smooth silica suspensions were found to interact through lubrication forces at very small length scales. In case of rough particles, the topological effect of the asperities was observed to play a role: the lubrication regime was pushed towards higher frequencies and stresses increased in an intermediate regime. Moreover, the concentration dependency of the behaviour was related to the presence of an additional, independent length scale.

An important question to ask is to what extent these findings at near-equilibrium conditions can be used to understand non-linear phenomena. As a specific application, the shear thickening behaviour of the different suspensions was considered. At such high stress levels, the confined suspensions undergo considerable normal stresses as well. A similar interplay between surface topology and local scale stresses was established. When effectively shielding the lubrication interactions between colloidal particles by means of a polymer brush, the extent of shear thickening could be reduced. The use of the effective hydrodynamic volume fraction was able to capture the transition between a continuous and discontinuous shear thickening state both for the smooth and rough silica suspensions. However, the topological features of the raspberry-like particles altered the mechanism behind the shear thickening behaviour, as they were responsible for the occurrence of strong tangential interactions.

Generally, the results in this chapter endorse high-frequency rheology as a probe for determining the subtle nature of the local scale stresses or interactions. The measured response was highly sensitive to changes in the surface topology at different length scales. In addition, contributions can be directly probed in suspension up to high particle loadings, while measured properties are statistically averaged over a larger sample.

Chapter 5

Dispersion quality of partially aggregated colloidal dispersions

An important parameter for the performance of nanomaterials is the degree by which the nanoparticles are dispersed in a medium. In this chapter it is investigated how rheological measurements can be used for characterising the state of dispersion in partially dispersed suspensions at intermediate to higher particle loadings, even for highly viscous matrices. The previous chapter illustrated that the scaling behaviour of colloidal dispersions towards the high-frequency limit reveals useful information on the local scale stress contributions. In this chapter, we focus on the high-frequency limit itself. Although the contribution of the particles is particularly visible in the low-frequency linear viscoelastic behaviour, the aim is to derive a more direct relationship between rheological properties and degree of dispersion from the loss modulus at high frequencies. To this end, we use our homebuilt piezo shear rheometer which was described in chapter 3. Measurements on spherical colloids with a varying degree of dispersion are used to demonstrate how high-frequency rheometry can be used to quantify dispersion quality. In addition, the derived concepts are used to follow the evolution of the dispersion during high shear mixing.

The following chapter appeared in published format and is adapted to shape this dissertation:

B. Schroyen, J. W. Swan, P. Van Puyvelde, J. Vermant. Quantifying the dispersion quality of partially aggregated colloidal dispersions by high-frequency rheology. *Soft Matter*, 13:7897, 2017.

B. Schroyen designed and executed the experiments, performed the data post-processing and wrote the major part of the manuscript.

5.1 Introduction

Considerable efforts have been devoted to the design and processing of nanomaterials to exploit novel functionalities associated with the nanoscale. Inorganic particles have been used to improve the physical properties of materials such as ceramics, elastomers or polymer films [145–147]. More recent applications include the usage in construction materials, *e.g.* to improve concrete durability, or in biomedical applications and advanced drug delivery [148, 149]. The final properties of nanocomposites depend on the characteristics of particles and matrix and their interactions. However, an additional factor that strongly affects the material performance is the degree of filler dispersion achieved during mixing [150]. For instance in coating and printing applications, high degrees of pigment dispersion are crucial for the final product quality [151, 152]. The performance of polymer nanocomposites is greatly influenced by the dispersion quality as well [153, 154]. The mechanical properties of clay-polymer nanocomposites for example are found to increase with increasing degree of dispersion due to a higher degree of exfoliation of the clay platelets [155].

Due to the colloidal nature of nanoparticles, dispersion methods need to overcome the van der Waals or other attractive forces, necessitating complex or energy-intensive processes [156, 157]. Having efficient tools to monitor the dispersion quality during processing are hence worthwhile [158]. However, quantifying the degree of dispersion is not always trivial. Electron microscopy offers sufficient resolution in the nanoscale, but sampling and sample preparation are often laborious and it is not always possible or cost effective to carry out a sufficient number of measurements to obtain statistically relevant data. Furthermore, not all liquid dispersions can be solidified or used in cryo-preparation. Scattering methods offer statistically averaged data, but samples may either have too much or too little contrast. Depending on the particle size distribution, any q-dependent analysis can be strongly influenced by outliers in the aggregate size distribution. For turbid systems advances have been made using multiple scattering techniques, either removing the multiple scattered light in techniques such as 3D-dynamic light scattering or fully exploiting it in

diffusing wave spectroscopy [159–161]. But still these techniques are performant only when the nanocomposites fulfil certain constraints, regarding for example scattering contrast, ergodicity and light absorption. An alternative is to turn our attention to methods which probe the dispersion quality indirectly, for example looking at macroscopic mechanical properties such as the viscosities or linear viscoelastic properties. Earlier work has illustrated the potential of rheological methods to assess the dispersion quality in either polymeric matrices [155, 162, 163] or low-viscous resins [164, 165]. Linear viscoelastic properties are very sensitive to changes in the microstructure. Moreover, the use of rheology and small amplitude oscillatory measurements in particular allows to study dispersions in the undiluted fluid state, even up to very high concentrations, without interfering with the dispersion process or state, hence offering potential for in-situ monitoring. The potential of tuning the frequency of the oscillation makes it possible to vary the length scale on which the structure is excited, from large scale structures at low frequencies, to local phenomena at high frequencies.

Information on the dispersion state from rheological data is often inferred qualitatively from the low-frequency elastic modulus G' as its behaviour is mainly dictated by the particle contribution [154, 162, 164, 166]. However, this contribution is not straightforward to analyse quantitatively without a priori knowledge on the interactions and on the details of the large scale structures formed, ranging from the packing of aggregates to the fractal dimensions of sample spanning networks [3, 167]. Low-frequency measurements probe the collective microstructure and are much more influenced by thixotropic and ageing effects [168]. At higher frequencies however, the observed structural length scale becomes localised, eventually to the scale of the colloidal building blocks which make up the dispersion [102]. Under certain conditions, the high-frequency limit is dominated by the hydrodynamic contributions, which are purely dissipative and will be different from the limit set by well dispersed individual particles [126, 137]. In this region the individual building blocks can be probed even when being part of a global network which allows for a quantitative approach to interrogate the nature of the local scale microstructure of the dispersion [155, 164]. In case of spherical fillers, the presence of aggregates or agglomerates leads to an increase in the effective volume fraction due to the particles being packed in inefficient structures [169]. The influence is less trivial for anisotropic particles as an improved dispersion quality can lead to larger aspect ratios and increased frictional interactions [155, 166].

In order to probe the high-frequency limit, the time scale of the applied oscillation must be much smaller than the time scale of diffusive colloidal motion [11]. For

Brownian hard spheres, the relevant frequency range is given by [102, 170]

$$\frac{k_B T}{a^3 12\pi^2 \eta_m} \ll f \ll \frac{\eta_m}{2\pi\rho_m a^2}, \tag{5.1}$$

with f the frequency in Hz, a the particle radius, $k_B T$ the thermal energy scale [3] and η_m and ρ_m on both sides the matrix viscosity and density, respectively. The upper limit of the hydrodynamic regime is when fluid and particle inertial contributions come in to play and when hydrodynamic interactions can no longer be considered to act instantaneously. Both effects occur at a similar frequency, depending on the respective densities of particles and matrix [102]. In case of hard spheres of 50 nm radius dispersed in a Newtonian medium of 0.1 Pa·s, the resulting frequency range is 10 Hz $\ll f \ll 10^9$ Hz. Note that for more concentrated dispersions, the diffusive response scales with the short-time self-diffusivity at the given concentration, so that η'_∞ enters in the left term of equation 5.1 (section 4.3.3). Colloidal interactions alter the force balance in equation 5.1, for instance due to an increase of the effective radius at contact stemming from repulsive interactions [127]. In the presence of attractive interactions, the characteristic time scale was found to scale with the range of the interaction potential through the thermodynamic stresses and the structure's response to flow [138]. In addition the hydrodynamic properties of the aggregates will be different from those of the individual particles [171, 172].

As discussed in chapter 4, the frequency dependency of the high-frequency moduli reveals in a subtle manner the interplay between the colloidal and hydrodynamic interactions, and their effects on the microstructure. In particular, the behaviour depends on the relative size of the hydrodynamic lubrication layer with respect to the range of the structural interaction forces. The high-frequency rheology can be further influenced by the presence of attractive interactions, and both direct contributions of the interaction force as well as changes in the hydrodynamic contributions are introduced as the particle spacing changes [102, 126, 127, 138]. It was observed that the existence of both repulsive and attractive colloidal interactions can shift the entry into the high-frequency region towards higher frequencies and alter the asymptotic behaviour towards the hydrodynamic limit [127, 138, 173]. Experimentally, in the hydrodynamic high-frequency limit, the curves of the loss moduli are expected to become parallel with that of the suspending medium.

High-frequency rheometry is proposed as a technique to quantify the degree of dispersion of partially dispersed colloidal suspensions, for intermediate to high volume fractions. The homebuilt piezo shear rheometer, described in chapter 3, is used for this purpose. In order to create samples of varying states of dispersion, spherical nanoparticles are dispersed in a low-viscous matrix by different mixing techniques and mixing times. The dispersion quality is quantified by subjecting

the high-frequency rheological data to a hydrodynamic analysis, after having identified the relevant scaling regime. As an application the evolution of the dispersion state during mixing is monitored by using the rheological dispersion quality index. Note that in this chapter, the term 'aggregate' is used for the building blocks of the dispersion created during the dispersion process. Although the size of these building blocks depends on the intensity and duration of mixing, and describing them according to the IUPAC nomenclature as 'agglomerates' may be more appropriate, the assumption in the measurement is that the linear response regime is probed and the structure is not affected by the measurement.

5.2 Experimental

5.2.1 Preparation of silica dispersions

Dispersions of colloidal silica particles in a low-viscous polydimethylsiloxane (PDMS) matrix (350 cSt Silicone oil, Sigma-Aldrich) were used as model systems. Partially hydrophobic silica particles were kindly provided by Nissan Chemical (MEK-ST-ZL, Nissan Chemical Industries, Ltd.) as a 30.7 wt% stock suspension in MEK. Multi-angle dynamic light scattering (DLS) measurements (ALV/CGS-3 Goniometer, ALV-GmbH) provided an average particle size of $d_h = 130$ nm, which was confirmed by SEM pictures.

Batches of 10 g were prepared with particle concentrations varying between 4.4 and 22.2 vol%. PDMS was added to a stock suspension of silica particles in MEK and mixed. This procedure was used to avoid the creation of large and irreversible aggregates during drying. The sample was placed in a Rotavap (R-214 Rotavapor, Büchi) at controlled conditions of 243 mbar and 50 °C to evaporate MEK near its critical point. Sample families of varying dispersion quality were prepared by mixing for 15 min with different techniques of increasing energy input. Particles were dispersed by magnetic stirring at 750 rpm (S) as to create a low intensity, global mixing. Note that at concentrations higher than 15 vol%, the samples were solid-like prior to mixing so that magnetic stirring was no longer possible. High shear mixing (UT) was employed as a second method by means of an Ultra-Turrax rotor-stator disperser (Ultra-Turrax T25 S25N-10G, IKA-Werke GmbH) run at 8000 rpm. The highest dispersing intensity was obtained by subjecting the samples to ultrasonic pulses (US). A finger shaped sonicator (UP400S, Hielscher) was operated at 60 % intensity and 50 % duty cycle at a frequency of 24 kHz. All samples were stored under vacuum for 15 min after dispersing to remove entrained air bubbles. Measurements were carried out immediately after this sample preparation to rule out potential effects of sedimentation or ageing.

5.2.2 Rheological measurements

Information on the dispersion quality was obtained by performing dynamic rheological measurements within the linear region over an extended frequency range. Commercial rotational stress-controlled rheometers (MCR 302, Anton Paar - Austria ; DHR-3, TA Instruments - USA) were used for oscillatory experiments in a frequency range between 0.01 - 20 Hz. In order to compare the measurement data quantitatively with the high-frequency results, tests were performed with a 40 mm diameter plate plate geometry at 200 μm gap distance. The strain amplitude was varied between $0.1 - 5\,\%$ to maximise the response while operating below the linear limit. A pre-shear of 25 s^{-1} was applied for 300 s after which the sample was allowed to recover for 300 s, until a reference structure at rest was obtained.

High-frequency oscillatory measurements were performed over a range of 20 - 2000 Hz with our homebuilt piezo shear rheometer. Figure 3.1 (chapter 3) showed a schematic view of the instrument together with pictures of the frame and measurement cell. The measurement cell consists of two piezo-ceramic stacks (PICA P-141.05 Shear Actuators, PI Ceramic GmbH) that operate in a simple shear mode, similar in design to Roth et al. [25]. Samples are placed in between parallel titanium substrates (10 mm side length) attached to both piezo stacks. The operating gap was kept at 200 μm as well, and a strain amplitude of $0.027\,\%$ was applied. The sample was allowed to rest for a period of 300 s after loading before starting measurements. All measurements were carried out at room temperature.

5.2.3 Monitoring a dispersion process

The evolution of the dispersion state during high shear UT mixing was monitored at rotor speeds of 4000, 8000 and 12400 rpm. Samples were taken at discrete moments in time for HF rheological measurements. In addition, multi-angle DLS measurements were performed to determine the equilibrium state of the aggregates after high shear mixing, and offer independent information on the hydrodynamic size of the colloidal building blocks. The dispersions were diluted to 0.01 vol% and subjected to gentle stirring in order to homogenise the samples without influencing the dispersion state. The aggregates are hence assumed to remain unchanged during dilution and homogenisation. Measurements were carried out at angles ranging from $20° - 90°$ with a $5°$ angle step size and a measurement time of 500 s per angle to obtain sufficient data averaging. Sedimentation was not observed over the course of the measurements. The mean aggregate size was determined by fitting the autocorrelation curves as a

function of the decay time τ with a cumulant expansion [174]:

$$g_2(\tau) - 1 = b\left[e^{-c\tau}\left(1 + \frac{d}{2}\tau^2\right)\right]^2. \tag{5.2}$$

The parameter b is defined by the intercept. c contains information on the average decay $\bar{\Gamma}$ of the exponential function and relates to the average diffusivity and therefore particle/aggregate size in the dilute suspension. The expansion assumes a monomodal distribution; polydispersity is accounted for by means of d, the second moment of the expansion.

5.3 Results and discussion

5.3.1 Rheological behaviour of the model system

The data obtained with the rotational and the piezo rheometer for samples produced by UT mixing are shown in figure 5.1 for different silica volume fractions and pure PDMS. Only higher volume fractions are compared for which interparticle effects were more pronounced. The measurements are representative of samples obtained via other dispersion methods as well. Due to the large matrix viscosity, the linear viscoelastic response is largely dominated by the hydrodynamic interactions among the particles. At high frequencies, the magnitude of the loss modulus is proportional to that of the suspending PDMS matrix, as shown in earlier work [167]. The loss moduli are plotted in figure 5.1 (top) for the UT samples, showing a general increase with increasing volume fraction. When judging the quality of rheological data, it is insightful to look directly at the phase angle, shown at the bottom in figure 5.1. At low frequencies, the angle deviates form 90°. This deviation is more pronounced with increasing volume fraction and reflects contributions from relaxation of stresses among large aggregates. At the highest frequencies measured with the rotational device the effects of instrument inertia lead to minor deviations (not shown here). For the PSR the phase angle at low frequencies is less precise due to signal to noise issues, in particular for the matrix and lower filler loading. At high frequencies, the matrix viscoelasticity dictates the phase angle in the suspensions, and the effect of particle volume fraction on the phase angle decreases.

The loss modulus normalised by the matrix contribution: $G''_{rel} = G''/G''_m$, shows more clearly how contributions to viscoelasticity from colloidal and hydrodynamic interactions change with concentration and frequency (figure 5.2). At low frequencies, the formation of large aggregates or a volume spanning network structure causes G''_{rel} to increase significantly with volume fraction,

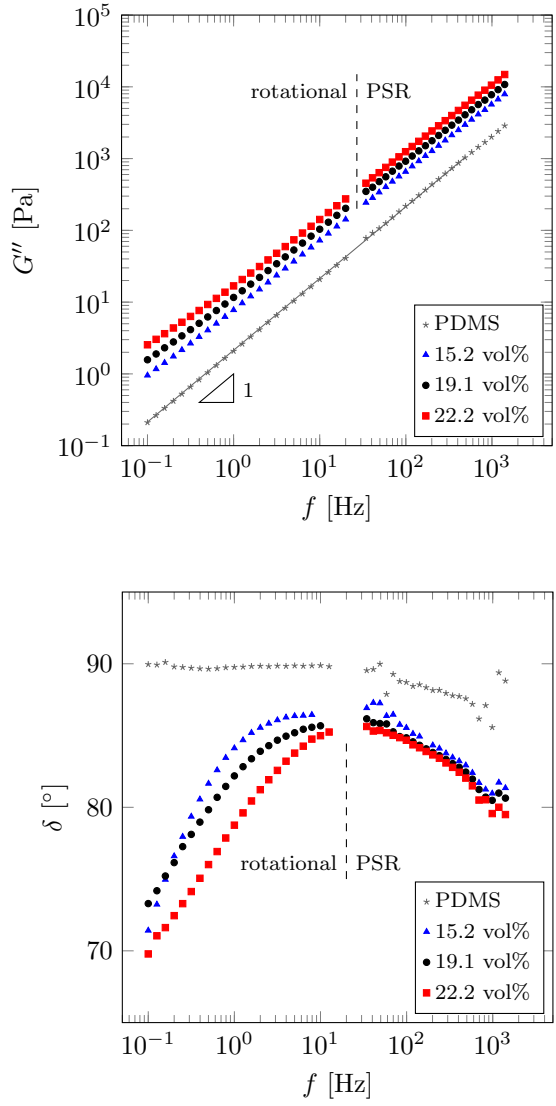

Figure 5.1: Linear viscoelastic loss modulus (top) and phase angle (bottom) of the UT samples measured at different volume fractions, compared to those of the matrix. Only the 3 highest concentrations displayed an elastic contribution that was detectable above the instrument limits.

which is also seen in figure 5.1. The relative loss moduli level off at high frequencies to a constant value. For the dilute suspensions, G''_{rel} is constant over the entire range. The evolution of G''_{rel} with frequency shows the value of the extended frequency range in the PSR, and in particular for more concentrated suspensions. The low-frequency behaviour stems from a complex interplay between colloidal and hydrodynamic interactions, whereas at high frequencies the constant value of the moduli can be attributed to a purely hydrodynamical regime, where only the effective volume fraction of the aggregates and inter-aggregate structure matter. The relative HF modulus $G''_{rel,\infty}$, calculated as the average value in the HF limit (figure 5.2), will be used for further analysis to characterise the dispersion quality [137].

5.3.2 Frequency scaling

Varga and Swan presented calculations of the stress response of a semi-dilute colloidal dispersion in the presence of attractive depletion interactions. Whereas their calculations are a virial expansion in the particle volume fraction, and hence not necessarily valid up to the volume fractions studied here, it is useful to compare their predictions and scalings to the experimentally observed quantities.

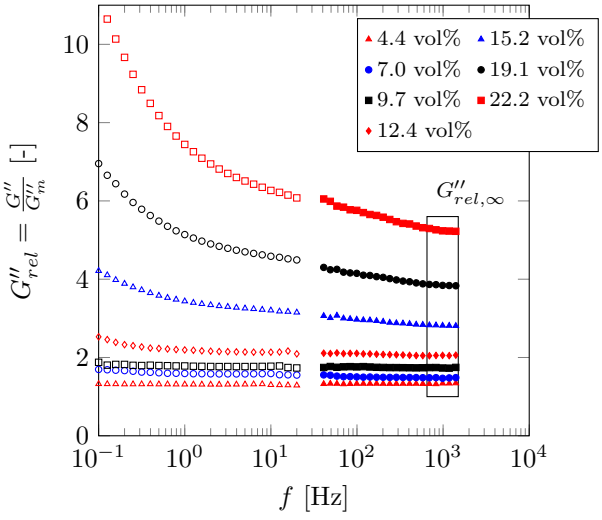

Figure 5.2: Relative loss moduli $G''_{rel} = \frac{G''}{G''_m}$ of the UT samples at different concentrations. High-frequency moduli (closed symbols) are again compared with moduli obtained from a commercial device (open symbols). The box indicates the frequency window used for the calculation of $G''_{rel,\infty}$.

They observed a transition between two viscoelastic regimes: one dominated by colloidal interactions among the particles, and the other at high frequencies, which is dominated by hydrodynamic interactions. The hydrodynamic regime exhibits a particular power law behaviour at high frequencies for the reduced real part of the complex viscosity:

$$\eta'_r = \frac{\eta' - \eta'_\infty}{\eta'_0 - \eta'_\infty}\,, \tag{5.3}$$

where η'_0 and η'_∞ respectively are the low- and high-frequency limits of η'. This quantity can be used to detect the emergence of the hydrodynamically dominated regime. The nominator removes the purely hydrodynamic component from the measured viscosity, whereas the denominator rescales the values but does not change the actual scaling behaviour. Note that a similar rescaling was used in chapter 4 to analyse the different stress contributions (section 4.3.3). Because the suspending PDMS is intrinsically viscoelastic (figure 5.1), a plateau value for η'_∞ is not necessarily reached over the measured frequency range. This renders direct rescaling of the measured stresses, such as in equation 4.4, invalid. Instead, an equivalent reduced viscosity for the experimental dispersions is constructed from the relative complex viscosities by replacing η' in equation 5.3 with $\eta'_{rel} = G''_{rel}$. This removes the effect of matrix viscoelasticity but still enables examination of frequency dependent variations in the loss modulus resulting from colloidal and hydrodynamic interactions among the suspended particles.

After this substitution, the value of $\eta'_{rel,\infty}$ is just the measured relative high-frequency modulus $G''_{rel,\infty}$ (figure 5.2). The quantity $\eta'_{rel,0}$ is arbitrarily chosen as the value of G''_{rel} measured at the lowest sampled frequency, as no zero shear viscosity is obtained for the concentrated, strongly attractive suspensions studied here. Yet, this arbitrary choice affects only the magnitude of the numerator without affecting the slopes of the reduced viscosity on a log-log plot. Another useful rescaling results from a consideration of the matrix viscoelasticity, and an increase of the internal shear rate as a result of part of the volume being occupied by non-deformable fillers. Because the PDMS matrix can be considered to be an isotropic fluid, a simple 'Gleissle' shift factor B can be used to renormalise the frequency [10]. This shift factor reflects the increase of the internal shear rate at constant stress, which in the hydrodynamic regime and well below the relaxation time of the matrix is proportional to the real part of the relative complex viscosity at high frequencies; hence,

$$B = \eta'_{rel,\infty} = G''_{rel,\infty}. \tag{5.4}$$

B successfully shifts the curves of G'' based on the limiting hydrodynamic value, as shown in appendix A.2.1, and allows comparison at equal internal shear rates.

Figure 5.3 compares the resulting real part of the reduced relative viscosity $\eta'_{rel,r}$ for the 3 highest concentrations as a function of the rescaled frequency, $B \cdot f$. Scaling the reduced relative viscosity and frequency in this way provides a comparative basis for dispersions of different particle loadings and matrix viscoelasticity. The rescaled viscoelastic response of all three suspensions is the same, which can be explained by the fact that the local aggregate microstructures probed at these high frequencies are similar across a range of primary particle volume fractions [126]. Two different scaling regimes can be observed. At rescaled frequencies below 1 kHz, the reduced relative viscosities decay with a power law. A slope of $\sim f^{-1/2}$ is shown for reference. This power law scaling suggests relaxation of small deformations in the aggregate microstructure dominated by colloidal interactions. In the second regime, above 1 kHz, the power law slope increases in magnitude such that the reduced relative viscosities decay as f^{-2}. In this regime, the internal aggregate structure is frozen. Hydrodynamic forces generate microstructural perturbations among aggregates and their collective diffusion relaxes the resulting entropic stresses [127]. The transition between regimes marks the entry into the HF limit of viscoelasticity, in which hydrodynamic forces as opposed to colloidal forces dominate the response. The reduced frequency at which this transition happens is expected and observed to be independent of the volume fraction.

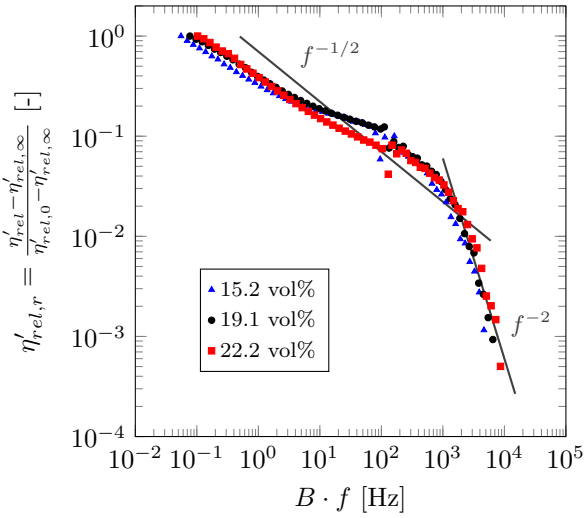

Figure 5.3: Real part of the relative complex viscosity reduced by the high- and low-frequency values as a function of the shifted frequency for 3 different volume fractions of the UT samples. Solid lines illustrate the limiting slopes in both regimes.

5.3.3 Derivation of a dispersion quality index

A quantification of the degree of dispersion can be determined from the relative loss modulus measured in the hydrodynamic regime. The measurement principle is illustrated in figure 5.4. In the high-frequency or hydrodynamic limit, the linear viscoelastic properties are dominated by matrix contributions and by hydrodynamic interactions between aggregates. The presence of particles distorts fluid streamlines [3, 175]. Such distortions of the flow field increase the energy dissipation during flow and hence the HF loss modulus. The magnitude of this effect depends on the effective hydrodynamic volume taken up by the partially dispersed silica particles and increases with aggregate size.

Figure 5.5 shows the evolution of $G''_{rel,\infty}$ as a function of primary particle volume fraction for the UT samples. The degree of dispersion can be quantified by comparing the measured high-frequency viscosity to the HF viscosity of a fully dispersed suspension of Brownian hard spheres at the same volume fraction. This quantity is purely hydrodynamic. It reflects only the structure of the suspension and not the relaxation processes resulting from colloidal interactions among primary particles. Results in figure 5.5 also illustrate that a hydrodynamic analysis based on G'' at 20 Hz, a frequency accessible by a standard rotational device, is valid for dilute suspensions for which G''_{rel} is constant over the entire frequency range (figure 5.2). However, important deviations occur for more concentrated samples due to increased colloidal interactions.

Different semi-empirical relationships have been derived for describing the viscosity of hard-spheres in the hydrodynamic limit [130, 135, 176]. Practically, these relationships differ mainly in their approach to the hard-sphere limit and

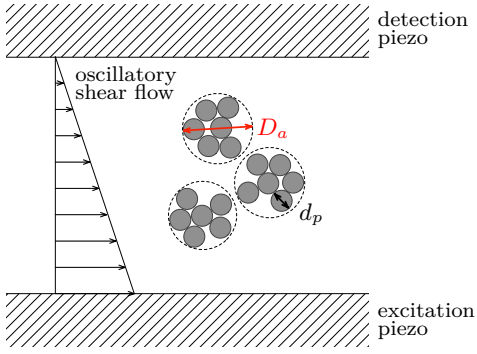

Figure 5.4: Schematic of the measurement principle: aggregates of colloidal particles ($d_p \approx 130$ nm) subjected to an oscillatory shear flow in a plate-plate geometry. D_a represents the hydrodynamic aggregate size.

for the concentrations considered here, variations in predicted values are small. However, the simulations of Sierou and Brady [135], which provide a complete description of the hydrodynamic interactions incorporating both long-range many-body interactions and near-field lubrication effects, yield the most rigorous data set available. Based on these results an analytical form for the HF limit of the relative loss modulus was derived [136]:

$$G''_{rel,\infty} = \frac{1 + \frac{3}{2}\phi_{eff}[1 + \phi_{eff}(1 + \phi_{eff} - 2.3\phi_{eff}^2)]}{1 - \phi_{eff}[1 + \phi_{eff}(1 + \phi_{eff} - 2.3\phi_{eff}^2)]}, \tag{5.5}$$

which is valid for random suspensions of colloidal or non-Brownian suspensions up until volume fractions $\phi_{eff} \leq 0.56$ or $G''_{rel,hf} < 12.6$. The volume fraction ϕ_{eff} is the effective volume fraction based on the hydrodynamic radius of the freely suspended particles. $G''_{rel,hf}$ based on equation 5.5 for ϕ_{eff} equal to the primary particle volume fraction is plotted in figure 5.5 as a dotted line and represents the viscosity of the suspensions in their most dispersed state. When aggregates are present, the effective volume fraction will be higher, and hence the high-frequency loss moduli are expected to grow more quickly. This is indeed what is observed in figure 5.5. Furthermore, figure 5.6 compares the divergence of $G''_{rel,\infty}$ as a function of ϕ for samples of different mixing families, *i.e.* U, UT and US samples. It can be observed that as the mixing intensity

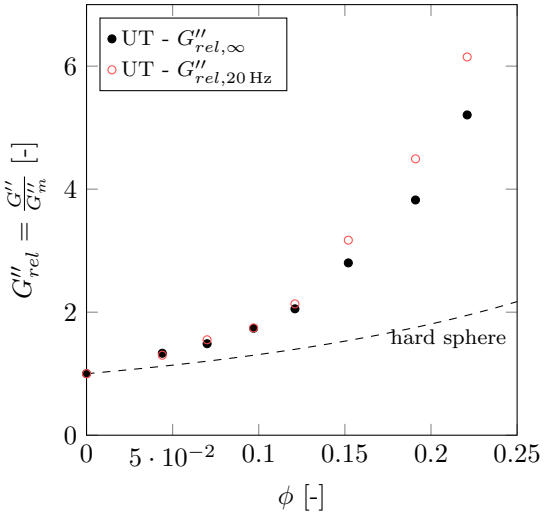

Figure 5.5: Evolution of the relative loss moduli of the UT samples obtained in the HF limit or at 20 Hz (figure 5.2) as a function of primary volume fraction. The hard-sphere case (dashed line) is shown as a reference.

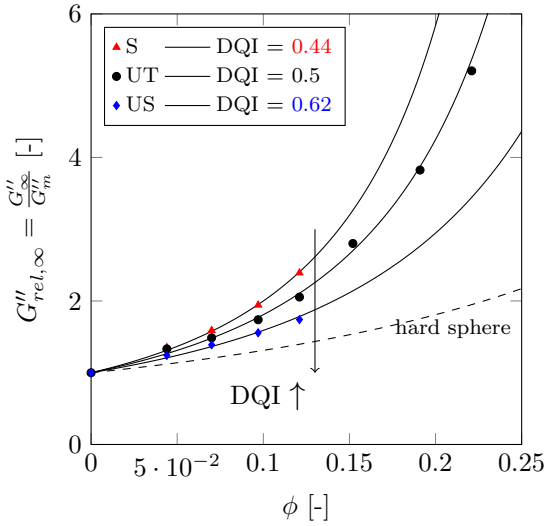

Figure 5.6: Evolution of the relative high-frequency loss moduli as a function of volume fraction for three different dispersion methods: magnetic stirring (S), high shear mixing (UT) and ultrasonication (US). Solid lines correspond to the fits of equation 5.5 with ϕ_{eff} whereas the dashed line represents the hard sphere case.

is increased (S→UT→US), the measured moduli decrease, which is consistent with an improved dispersion quality in response to more vigorous mixing.

For aggregated suspensions, the effective volume fraction can be defined as the ratio of the primary particle volume fraction: ϕ, to a dimensionless quantity termed the dispersion quality index: DQI,

$$\phi_{eff} = \frac{\phi}{\mathrm{DQI}}. \tag{5.6}$$

The dispersion quality index indicates the distance from a fully dispersed state in which the HF viscosity is well described by equation 5.5 with $\phi_{eff} = \phi$ and DQI = 1. The DQI quantifies the reduction in volume accessible to the suspending media for flow around suspended aggregates. Thus, DQI is a measure of the effect of hydrodynamic interactions among aggregates only. This modification of equation 5.5 results in a single-parameter model for $G''_{rel,\infty}$. The measured relative HF viscosity is fitted for the DQI for each of the sample families, and the calculated fits are plotted in figure 5.6. The fits agree well with all the experimental measurements. In principle, the maximum value that can be obtained is 1 and represents the case of fully dispersed hard spheres. The minimum value that is possible depends on the actual volume fraction ϕ, since

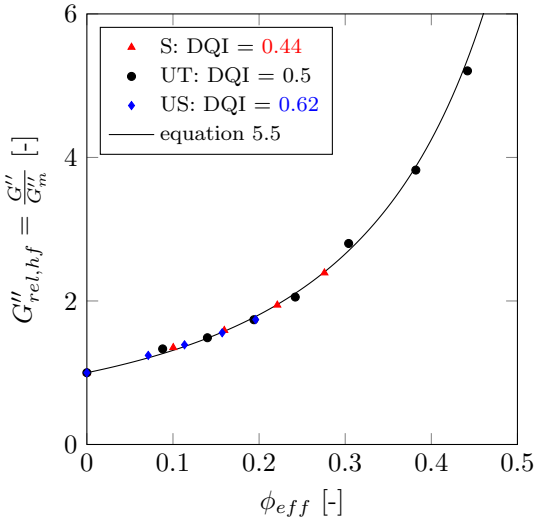

Figure 5.7: Evolution of the relative high-frequency loss moduli as a function of the effective volume fraction, obtained by fitting via the DQI.

equation 5.5 is only valid for $\phi_{eff} \leq 0.56$ and since the high-frequency viscosity diverges when approaching maximum packing. Furthermore, the analysis implies that the local building blocks of the dispersion remain unchanged, even at higher volume fractions at which these structures interact more strongly (figures 5.1 – 5.2). The fitting is therefore valid until when the dispersion becomes dense and aggregate formation is hindered. When plotting $G''_{rel,\infty}$ as a function of ϕ_{eff}, the data for the different sample families can be reduced to a single mastercurve (figure 5.7). The DQI improves (grows) when increasing the mixing intensity with a value of 0.44 for simple magnetic stirring and 0.62 for ultrasonicated samples. This confirms that aggregates persist in these suspensions even with high mixing intensities. Note that the absolute value of the effective volume fraction is influenced by the internal aggregate structure [177]. The DQI should be interpreted in relative terms as it probes the global structure of the dispersion and not the internal structure of the aggregates. However, since the proposed index is unaffected by Brownian motion and colloidal interactions, it enables the quantification of the dispersion quality of colloidal suspensions in a well-defined manner.

5.3.4 Monitoring a dispersion process

Dispersion processes are used to break up larger aggregates into dispersed and uniformly distributed particles. The derived DQI can be applied to monitor the evolution of the dispersion state during mixing operation. Here, it is used to monitor the performance of the high shear UT mixer as a function of mixing time and intensity. In order to obtain more insight into the fluid flow behaviour, the mixer was modelled in COMSOL. Simulations were carried out in 2D on a Newtonian fluid; the results are shown in appendix A.2.2. The combination of a high rotational speed and thin gap between rotor and stator yields strong shear flows and jets that continue radially outwards through the slits of the stator. The break-up forces will hence be the largest near the walls between the rotor and stator. The flow profile in the gap occurs primarily in the tangential direction, and a "maximum" shear rate can be calculated (table 5.1). It must be realised that this is only an estimation: the actual 3D flow profiles for a shear thinning suspension are far more complex than considered here for the simple model.

Figure 5.8 displays the evolution of the DQI during high shear mixing as a function of mixing time for different rotor speeds. For all samples, the DQI evolved in time, gradually improving and reaching a terminal, equilibrium

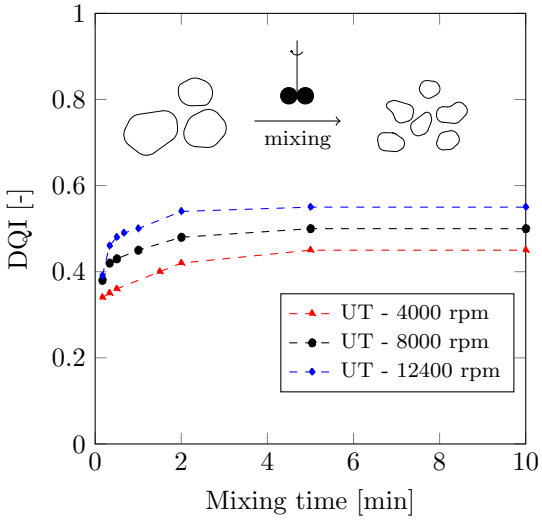

Figure 5.8: Evolution of the DQI as a function of mixing time for a dispersion of 15.2 vol% silica particles. Particles are dispersed by Ultra-Turrax mixing at 3 different intensities.

Table 5.1: Simulated shear rate in the gap $\dot{\gamma}$, equilibrium DQI and average aggregate diameter D_a for different mixing velocities N. Aggregate sizes were determined via DLS measurements (equation 5.2). Primary particles have a diameter $d_p \approx 130$ nm.

N [rpm]	$\dot{\gamma}$ [1/s]	DQI [-]	D_a [nm]	N_p/N_a
4000	11700	0.45	445	18.0
8000	23100	0.5	365	11.1
12400	36500	0.55	275	5.21

value after several minutes. In addition, at all times, the measured DQI increased with increasing mixing intensity. The evolution towards an equilibrium state is somewhat faster with increased mixing intensities as well. Note that the time resolution of the DQI measurements is restricted by sampling limitations. However, improved sampling rates might be achieved through in-situ measurements. These results are in agreement with previous findings on hydrodynamic stress induced dispersion and fragmentation [178], which reported that with sufficient mixing, an equilibrium aggregate size emerges at each imposed shear rate.

The equilibrium hydrodynamic aggregate sizes are also calculated from DLS measurements on dispersed and diluted samples via the Stokes-Einstein equation and compared with the equilibrium DQI in table 5.1 [178, 179]. The average aggregate size varies between 2-4 times the primary particle diameter. Both high-frequency rheology and DLS measurements show an improvement in the dispersion quality with increasing mixing intensity. Furthermore, DLS results confirm that small aggregates consisting of a few particles continue to exist at high mixing intensities. Note that the cumulant analysis (equation 5.2) assumes a monomodal distribution of spherical aggregates. However, since both high-frequency loss moduli and DLS data probe the hydrodynamic aggregate size, results from both methods can be compared [137]. When comparing the results of the two methods in table 5.1, the evolution of the DQI and D_a agree with each other. It must however be emphasised that, although the aggregates are assumed to remain unchanged during dilution and homogenisation, changes in size or structure cannot be ruled out completely.

Sonntag and Russel derived a relationship between the applied shear rate and average number of primary particles per aggregate N_p/N_a for the break up of aggregates subjected to hydrodynamic stresses [180]:

$$\frac{N_p}{N_a} = A \cdot (\eta'_\infty \dot{\gamma})^n. \tag{5.7}$$

Here, η'_∞ is used as a measure for the suspension viscosity, which represents the actual hydrodynamic stress in the suspension at a given volume fraction and at

higher shear rates more closely. Assuming that the shear applied in the gap (figure A.4) is the dominant break-up mechanism, experimental N_p/N_a (table 5.1) can be fitted with equation 5.7, resulting in an exponent $n = -0.7$ and prefactor $A = 1.26 \cdot 10^4$. Furthermore, by using structural information of the aggregates, equation 5.7 can be applied to relate the average aggregate size D_a to the shear rate [177]. As the dispersion quality index is proportional to the effective hydrodynamic volume fraction of aggregates in the dispersion, it can be used in combination with a measurement of d_a to determine N_p/N_a:

$$\mathrm{DQI} = \phi/\phi_{\mathrm{eff}} \approx \frac{N_p}{N_a} \cdot \left(\frac{d_p}{D_a}\right)^3. \tag{5.8}$$

When assuming that the aggregates are fractal-like, a power law relationship $N_p/N_a = (D_a/d_p)^{d_f}$ suggests an aggregate fractal dimension: $d_f \approx 2.25$, which corresponds with a reaction-limited aggregation process. Using these same relations, *a priori* knowledge of the aggregate fractal dimension and measurement of the DQI can be used to estimate the average aggregate size: $D_a/d_p \approx \mathrm{DQI}^{1/(d_f-3)}$. Note that this analysis neglects the polydispersity of the aggregates and assumes a mass-fractal-like structure. This assumption is not necessarily valid, since other types of aggregate structures have been reported for colloidal dispersions as well [181, 182], and the aggregate structure may be altered during the dispersion process. In addition, fractal models are generally not applicable to aggregates that consist only of relatively few particles. Nonetheless, the analyses described in this paragraph serve as an illustration. For certain systems, these can be of practical engineering value for connecting the dimensionless dispersion quality index to a physical dimension in the suspension.

5.4 Conclusions

Rheology is of particular interest for assessing the dispersion state of partially dispersed colloidal particles since it is highly sensitive to the microstructure. Whereas obtaining information about the state of dispersion from the low-frequency rheology would necessitate assumptions about the interplay between the microstructure and the colloidal interactions, high-frequency rheology offers a more elegant method to quantify the degree of dispersion. For this purpose a homebuilt piezorheometer was constructed that operates in linear shear flow. The mechanical design of the setup, detection method and alignment sensitivity were optimised to perform accurate measurements at frequencies between 20 - 2000 Hz. Measurements on model dispersions of colloidal silica particles showed that in the high-frequency limit, obtained by the piezorheometer, the loss

modulus is dominated by matrix contributions and hydrodynamic interactions. The limiting high-frequency modulus G''_{hf} was used to assess the dispersion quality by quantification of the distance to the case of fully dispersed particles through a hydrodynamic viscosity model. The resulting dispersion quality index DQI depends only on the increased effective volume fraction stemming from aggregates. In case of spherical particles, this index varies from 0 to 1 with a value of 1 representing finely dispersed particles. Although the proposed method does not account for the internal aggregate structure, it enables to assess the dispersion state of partially dispersed nanoparticles in a well-defined manner. The derived DQI was used to follow the evolution of the average degree of dispersion during mixing with a high shear mixing device. The degree of dispersion was observed to improve with increasing mixing time and intensity.

Chapter 6

Conclusions and Outlook

The linear viscoelastic signature of a colloidal suspension contains valuable information on the dynamics, microstructure and interactions inside the material. Ideally, to obtain an integrated picture of the dispersion from oscillatory rheometry, the entire relevant frequency range should be covered, ranging from a low-frequency region where slow or collective properties determine the response to a high-frequency region that is governed by the local structure and dynamics. The frequencies which delineate these regions are determined by the characteristic relaxation processes of the microstructure. From an experimental point of view the high-frequency region is more challenging to characterise since conventional devices cannot reach sufficiently high frequencies. In this study, access to this region was obtained by developing and employing a homebuilt piezo shear rheometer. Probing the high-frequency response proves to be a very clear method to quantify local scale properties in colloidal suspensions. The concepts that were derived can be of interest both for fundamental and more applied purposes.

Development of a high-frequency piezo shear rheometer

Piezo shear rheometer

The first part of this thesis considered the development of a piezo shear rheometer. The instrument was designed to directly extend the accessible frequency range of conventional rheometers by 2 orders of magnitude and to allow to continuously study the rheological behaviour of colloidal suspensions towards the high-frequency limit. Inherently, piezo shear rheometers are more suited for materials

with larger magnitudes of the linear viscoelastic moduli. For the applications addressed in this project, the signal detection and alignment method were optimised to enhance both the sensitivity and accuracy. The electromechanical behaviour of the rheometer was simulated in COMSOL and was used for aiding the design of the setup. A three-point mechanical alignment method was installed for efficiently controlling the gap between $0 - 400\,\mu$m with a resolution down to the order of $\sim 1\,\mu$m. The signal analysis was carried out by means of a LockIn amplifier with narrow filter settings for optimal sensitivity.

The piezo shear rheometer only needed a simple calibration, and sample properties can be derived from the measured response in a straightforward manner over a frequency range between $10 - 2000$ Hz. Above 2000 Hz, strong resonances occur which were inherent to the alignment tools. In order to improve the measurement accuracy near the operating limits of the instrument, electromechanical effects need to be taken into account. The transfer function of the electric circuit interferes with the actual signal both at low and high frequencies, and is especially important for accurate phase angle measurements below 20 Hz. Furthermore, although the setup is generally operated in the gap loading limit, an additional correction factor is required for low-viscous fluids measured at higher frequencies which accounts for deviations from this limit. The performance of the setup was evaluated by comparing measurements on different viscous and viscoelastic standards with data obtained from a commercial device, using the overlap region, and time-temperature superposition data.

Applicability

The setup can be used to detect linear viscoelastic properties for amplitude ratios $|AR| > 7.1\sqrt{f}$ with an experimentally determined minimum phase resolution $\delta \approx 2°$. Practically, this means that at a measurement gap of 200 μm, complex moduli $|G^*| > 14.2\sqrt{f}$ can be determined. The upper limit in measurable modulus stems from the compliance of the piezoelectric stack and is generally not an issue for complex fluids. An important limitation in terms of applicability relates to the rather uncontrolled loading conditions in the PSR: the applied forces are not controlled and applying a pre-shear is not possible. This is mainly an issue when the microstructure of the sample under investigation does not relax or is irreversibly altered after loading, as can for instance be the case for gel-like materials. The measurement gap can be varied between $0 - 400\,\mu$m and limits the applicability of the setup to materials for which the microstructural length scales are of order ~ 10 μm or smaller. A final limitation of the present setup is the absence of a temperature control unit, so that it is only possible to carry out measurements at environmental conditions.

The surface topology of particles determines the nature of local stresses in colloidal dispersions

In the second part of this thesis, the interplay between the nature of the interparticle potential, particle surface topology and local stress contributions in a suspension were studied. Conventional rheometry was combined with measurements with the piezo shear rheometer to monitor the transition towards the high-frequency limit. By probing the dispersions at frequencies scales that are high compared to their characteristic diffusional relaxation times, local stress contributions acting at length scales near the particle surface could be identified. The stresses in this thin boundary layer around the particles were strongly influenced by the surface topology, and an intricate interplay between potential, topology and hydrodynamics was revealed.

Influence of a grafted polymer layer

The particle surface topology and potential were varied in different manners. A first type of particles consisted of sterically stabilised PMMA-*g*-PHSA particles with varying grafted layer thicknesses. Results showed that the thickness and permeability of the polymer layer dictate the interplay between different contributions. With increasing grafted layer thickness, the extent of shielding of the hydrodynamic lubrication force increased while repulsive interactions between polymer layers became more prominent. For particles containing thick polymer brushes on the surface, the extent of lubrication shielding varied with concentration and indicated the effect of permeability. The elastic stress contributions were compared with model predictions taking only hydrodynamic lubrication interactions, hard-sphere repulsions or repulsive interactions between polymer brushes into account and showed qualitative agreement.

Influence of roughness via distinct asperities

Secondly, the effect of particle surface roughness was studied by employing charge-stabilised raspberry-like silica particles with distinct asperities. Smooth particles showed a generic behaviour as a function of volume fraction, and the stresses that occurred at very small length scales were found to be governed by hydrodynamic lubrication interactions. For rough particles, the behaviour was no longer generic and topological effects of the asperities were found to play a role. The lubrication regime was pushed towards higher frequencies and stresses increased in an intermediate regime. The behaviour changed with volume fraction owing to the presence of an additional independent length scale.

Shear thickening behaviour

In an additional study, the shear thickening behaviour of the different suspensions was investigated. The forces that govern shear thickening arise in a very thin boundary layer close to the particle surface, and were hence strongly influenced by the surface topology as well. For the sterically stabilised particles, increasing the amount of lubrication shielding by means of a thick grafted polymer layer suppressed the extent of the viscosity increase. Results on the silica particles implied that the presence of asperities can cause strong tangential stresses at sufficiently high volume fractions which change the mechanism behind the shear thickening behaviour.

Quantifying the degree of dispersion in partially aggregated suspensions through the high-frequency response

Colloidal systems often contain strong attractive interactions that lead to aggregation and alter the behaviour of a suspension. Quantifying the degree of dispersion is not always trivial, and can be particularly challenging at higher filler concentrations. The final part of this thesis discussed the applicability of high-frequency rheology as a versatile tool for quantifying the degree of dispersion.

Derivation of a dispersion quality index

Measurements on model suspensions of colloidal silica particles showed that in the high-frequency limit, which could be reached by employing the piezo shear rheometer, contributions of the relaxation processes are negligible and hydrodynamic stresses determine the response. These stresses are dissipative in nature and only depend on the effective volume taken up by particles or aggregates. Hence, by comparison with a hydrodynamic viscosity model, the deviation from a case of fully dispersed particles could be quantified. A dispersion quality index was derived which, in case of spherical particles, varies from 0 to 1 with a value of 1 representing finely dispersed particles. Effectively, this index relates to the colloidal building blocks in the dispersion. The proposed method enables assessment of the dispersion state of partially dispersed nanoparticles in a well-defined manner.

Application towards the monitoring of dispersion processes

The derived dispersion quality index was used to follow the evolution of the average degree of dispersion during mixing with a high shear mixing device. The degree of dispersion was observed to improve with increasing mixing time and intensity. Furthermore, the results were compared with simple simulations of the high shear mixer and with DLS measurements, and could be used to derive relationships between the shear rate, aggregate size and structural parameters of the aggregates.

Outlook

Extensions to the piezo shear rheometer

The medium viscosity η of the suspensions considered in this work was chosen to obtain a sufficiently high signal-to-noise ratio. However, to accurately study the properties for instance of suspensions in lower viscous resins, the sensitivity of the instrument should be improved. An enhanced signal can easily be reached by increasing the surface area S of the substrate. However, this method has geometrical limitations. An alternative method exists in the use of different types of piezoelements: by using longitudinal stacks rather than shear stacks for force detection, the sensitivity can easily improved by a factor 10.

An important extension to the current instrument will be the installation of a temperature control unit. While enabling a better environmental control, it will allow the execution of temperature dependent measurements. An important limitation to this are the piezo shear stacks, which have a maximum operating range until $\sim 100\,^{\circ}\mathrm{C}$. However, in order to study polymeric or composite materials, a temperature range until $\sim 150\,^{\circ}\mathrm{C}$ would be of interest. Although the range can be enlarged by using other types of piezoelements in a different configuration, piezoelectric properties generally change with temperature, which complicates the calibration. The most elegant option for installing a temperature control unit with a sufficiently large range will be to decouple the sample environment from the piezoelements and to heat locally.

The preparation and loading of a sample can affect the microstructure in an-ill defined manner. Applying a pre-shear after loading aims at starting rheological measurements from a well-defined state. The PSR is only able to operate in oscillatory mode and at small strains, and the absence of such an option is an important limitation. For the dispersions considered in this work, this was less of an issue: the Brownian nature of the colloids acts as a randomising force. Furthermore, loading effects mainly affected the collective properties of

the microstructure and hence showed at lower frequencies. Nonetheless, this is not the general case and for many materials a pre-shear is useful. Although few linear shear setups exist that can apply large deformations [108], the most versatile option will be to combine a piezo setup with a commercial rotational instrument. However, this requires large adaptations to the design.

Limits of the gap loading correction

Wave propagation effects impose important design limitations for measurements at higher frequencies. For instance, operation under the gap loading assumption limits the maximum frequency that can be applied as a function of the gap height and sample properties. In this work, when deviating from this limit, the measured properties were corrected via a method proposed by Schrag [20] (equations 3.24 − 3.25). Although this method is of great practical use, no other study could be found that experimentally reports the application of such correction factors. It would be relevant to investigate in a detailed experimental study what the accuracy of the corrections are depending on the deviation from the gap loading limit.

Local stress contributions in colloidal dispersions

Chapter 4 elaborated on the interplay between surface topology and local stress contributions and encourages further research. Experimentally, only a few parameters were varied. Open questions for instance are the role of attractive interactions or the influence of non-spherical particle shapes, which add additional dimensionality to the system. Furthermore, the experimental findings add to a theoretical understanding of the nature of local stresses in a suspension and can aid in the improvement of model predictions. The hydrodynamic stresses that act through the medium are tensorial in nature, and changing the surface topology alters the different stress contributions in a non-trivial manner. Describing such contributions correctly will be key in predicting their behaviour both at near- and non-equilibrium conditions.

Dispersion state in suspensions of anisotropic nanoparticles

In case of partially dispersed suspensions consisting of spherical colloids, the degree of dispersion can be derived in a straightforward manner from the high-frequency loss modulus. Particles that are packed in inefficient aggregate structures lead to an increase in effective volume fraction and will increase the dissipation. For dispersions consisting of anisotropic particles, such relationships

are less straightforward. A crucial parameter is the way that particles assemble to form aggregate structures. For instance, it was found that for composites with platelike nanoclay fillers, a decrease in dispersion quality decreases the extent of exfoliation and actually reduces the energy dissipation [155]. Given the abundant use of anisotropic colloids in synthetic dispersions, deriving similar structure-property relationships as in this work, although less universal, can be of important practical use.

Structural evolution in mixing units

The break-up of agglomerates during mixing results from a complex interplay between different forces. Studying such phenomena at higher particle loadings in particular can be challenging. Advanced rheological techniques such as superposition rheology or rheo-confocal microscopy can be used to investigate the structural evolution of agglomerates during well-defined shear flows, and at relevant volume fractions. Furthermore, the evolution in more complex flow fields can be investigated by means of confocal microscopical techniques. Such studies can further improve the understanding of break-up mechanisms and aid in the development of simulation methods for predicting the behaviour of colloidal dispersions in mixing units.

Dispersion quality in industrial environments

Aggregation in colloidal dispersions poses an issue for many existing applications. For instance, in nanomaterials, nanoparticles often have to be well dispersed to exploit their functionalities. In fact, the method developed in this work for quantifying the degree of dispersion was used to assess the dispersion quality in several industrial materials. These included dispersions of fumed silica particles (typically used as thickeners), titanium dioxide dispersions (used *e.g.* in paints), food formulations, and resins for additive manufacturing. The results were not presented in this thesis due to confidentiality agreements. Nonetheless, this work can be of relevance for many synthetic applications. Critical will be the extent to which the derived DQI can be applied to more complex formulations.

In order to improve process efficiency and product quality, having in-situ tools available for measuring the dispersion quality would be hugely beneficial. The proposed scientific method offers a robust solution for measuring the dispersion quality even for more concentrated suspensions. However, important technological advances will have to be made. The current setup is optimised for lab measurements but is not directly applicable as an in-situ tool. Furthermore, for suspensions in low-viscous resins, resonator methods may be more applicable.

Appendix A

A.1 Appendix to chapter 4

A.1.1 SEM Images

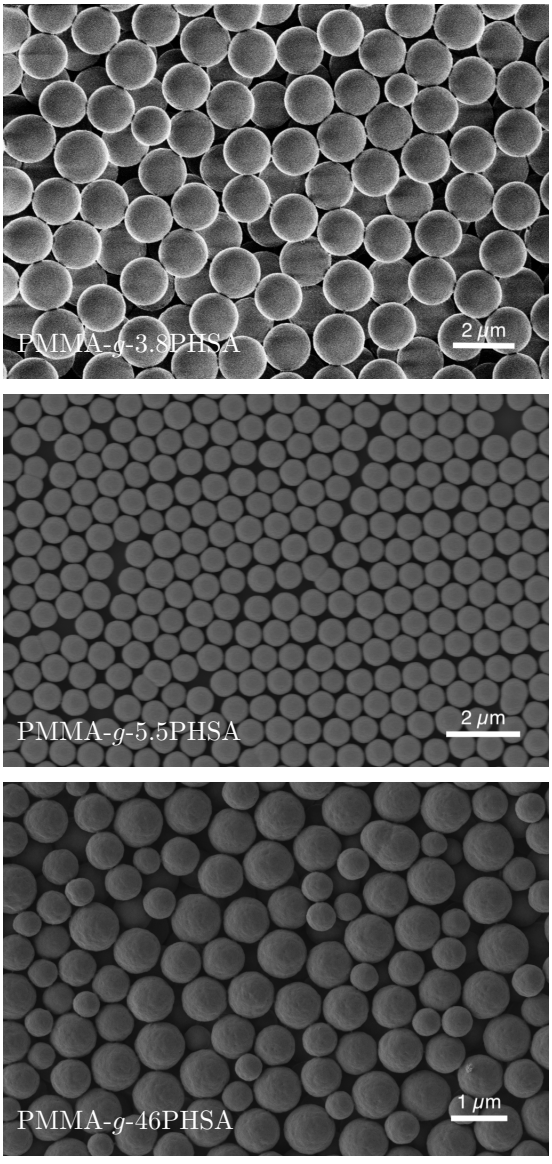

Figure A.1: SEM pictures of different PMMA-*g*-PHSA particles.

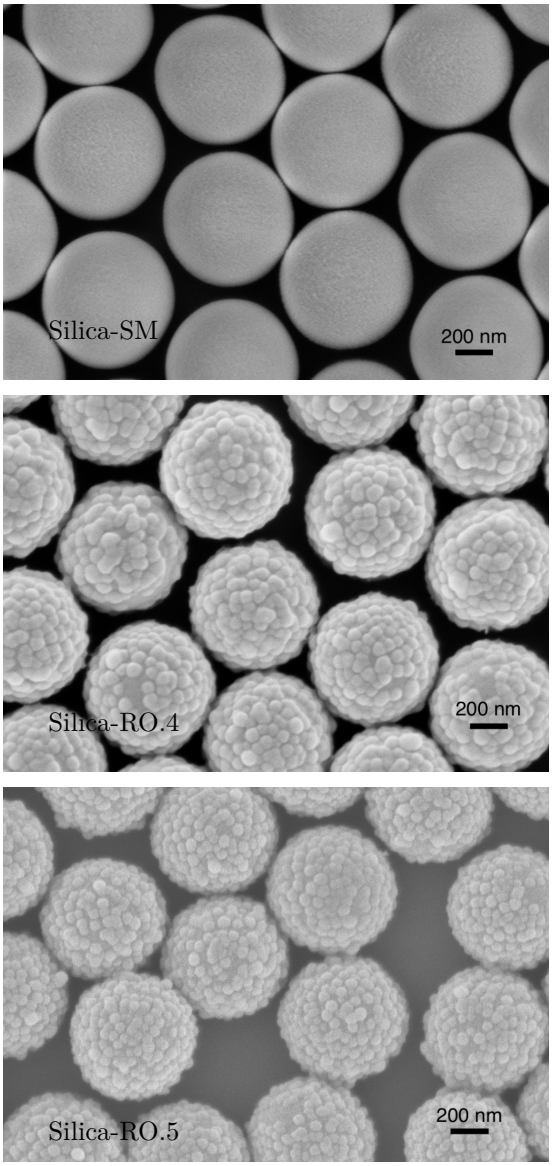

Figure A.2: SEM pictures of different silica particles.

A.1.2 Calculation of the high-frequency elastic modulus

Model calculations of G'_∞ are used to validate the measured elastic stresses. Model predictions were determined by taking into account single mechanisms either from lubrication stresses, hard-sphere repulsions or repulsive interactions between polymer brushes.

Lubrication interactions Analytical expressions were derived for predicting the elastic plateau modulus induced by lubrication interactions [126, 127]. However, these predictions were found to underestimate the modulus, and better fits are generally obtained when using the following expression from Lionberger and Russel [102]:

$$\frac{(2a)^3 G'_\infty}{k_B T} = \frac{24\phi^2}{5\pi} \int_1^{1+\frac{\eta}{8.154\eta'_\infty}} \left[W + s(1-A)\frac{d\ln g}{ds} \right] W g s^2 ds. \tag{A.1}$$

$s = r/2a$ is the dimensionless separation, $g(s)$ the radial distribution function and W and A are respectively the hydrodynamic diffusive and advective functions along the center lines of particles [130]. Numerical results based on equation A.1 together with the lubrication approximation were applied to predict the elastic stress plateau induced by lubrication stresses for different ϕ_{eff}.

Hard-sphere repulsive interactions Determining the response resulting from a hard-sphere repulsion in the absence of lubrication interactions is easier, since it does not require solving complex hydrodynamic functions. The high-frequency modulus could hence be directly calculated via [102]:

$$\frac{a^3 G'_\infty}{k_B T} = \frac{6}{5\pi} \cdot g^{hs}(2a;\phi) \cdot \phi^2 \alpha^{1/2}, \tag{A.2}$$

and scales with $O(\alpha^{1/2})$. The particle radius a is determined via the topological parameters of the surface, as shown in section 4.3.3. The hard-sphere radial distribution function at contact $g^{hs}(2a;\phi)$ was determined via the Carnahan-Starling approximation [183] for $\phi < 0.5$, and from simulations for $\phi \geq 0.5$ [130]:

$$\begin{cases} g^{hs}(2a;\phi) = \frac{1-\phi/2}{(1-\phi)^3}, & \phi < 0.5; \\ g^{hs}(2a;\phi) = \frac{0.78}{0.64-\phi}, & \phi \geq 0.5; \end{cases} \tag{A.3}$$

so that the reduced modulus in equation A.2 only depends on the volume fraction. In the equations above, the volume fraction was again approximated by ϕ_{eff}, and hence via the effective hydrodynamic volume (figure 4.3).

Repulsive interactions from grafted polymer layers The high-frequency modulus stemming from repulsive interactions between grafted polymer layers was calculated using the expression of Zwanzig and Mountain [141]:

$$\frac{a^3 G'_\infty}{k_B T} = \frac{3\phi}{4\pi} + \frac{3\phi_{eff}^2}{5\pi} g^{hs}(2a,\phi) \frac{a}{k_B T} \left[- \frac{d\Phi(r)}{dr} \right]_{r=2a}. \tag{A.4}$$

While the 1st term arises from the thermal kinetic energy of particles and is small, the 2nd term dominates the stress and depends on the repulsive force acting between nearest neighbours. In order to estimate G'_∞, the interparticle potential $\Phi(r)$ near contact hence needs to be derived. Here, $\Phi(r)$ was determined via the entropic theory of Milner et al. [184]:

$$\begin{cases} \Phi(r) = \infty, \;\; r < 2a_c; \\ \Phi(r) = \Phi_0 \Big[- \ln(y) - \frac{9}{5}(1-y) + \frac{1}{3}(1-y^3) - \frac{1}{30}(1-y^6) \Big], \\ \qquad\qquad\qquad\qquad\qquad\qquad 2a_c < r < 2(a_c + h_{co}); \\ \Phi(r) = 0, \;\; r > 2(a_c + h_{co}). \end{cases} \tag{A.5}$$

The dimensionless length $y = \frac{r-2a_c}{2h_{co}}$ and prefactor $\Phi_0 = \left(\frac{a_c \pi^3 \cdot h_{co}^3 \cdot \sigma_p}{12 \cdot DP \cdot l_s^2} \cdot k_B T \right)$, with the segment length $l_s \approx \frac{6R_g^2}{h_{co}}$, were estimated via the properties of the grafted polymer brushes (table 4.1) [185]. In accordance to the dimensionless length y, the radial contact value for calculating the interparticle potential was chosen based on the contour length h_{co} of the polymer rather than the hydrodynamic length.

A.2 Appendix to chapter 5

A.2.1 'Gleissle' shift factor

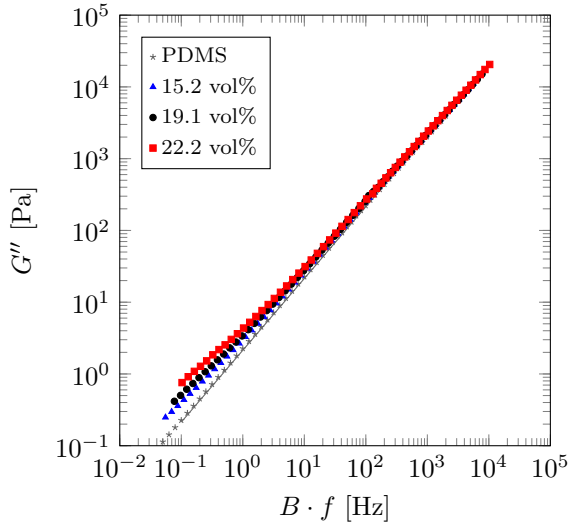

Figure A.3: Loss moduli as a function of the rescaled frequency based on a 'Gleissle' shift factor for the 3 highest volume fractions of the UT samples [10].

A.2.2 Simulations of the Ultra-Turrax mixer

Simulations of the Ultra-Turrax mixer were carried out in COMSOL MP in 2D by employing the 'Rotating Machinery' interface, which combines the Navier-Stokes and continuity equations with rotating meshes. Figure A.4 shows the profiles for a Newtonian fluid, with $\rho = 970$ kg/m^3 and $\eta = 0.34$ Pa·s. The gap in between the rotor and stator is only 0.35 mm and leads to large shear rates: at a rotational speed of 8000 rpm, the maximum estimated shear rate in the gap is $\dot{\gamma} \approx 23100$ 1/s. In reality, the rotor-stator configuration is open from the bottom to facilitate a global mixing. The actual 3D flow profiles are hence more complex than considered here for the simple model.

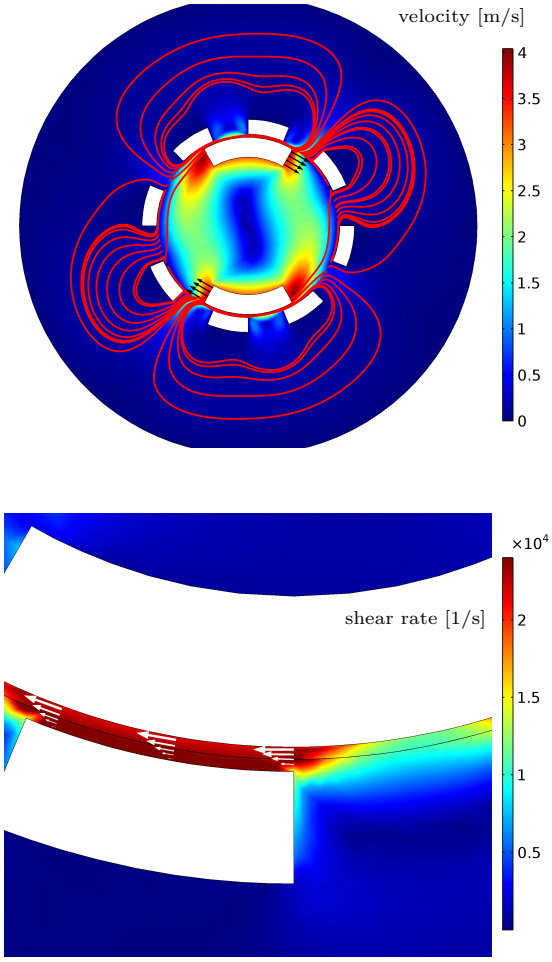

Figure A.4: 2D simulations of the flow in an Ultra-Turrax mixer. (top) Velocity profile at a rotational speed of 8000 rpm. The colour map depicts the velocity magnitude, whereas the flow direction of the rotor is given by the black arrows. Fluid streamlines (red) illustrate the flow profile in and out of the slots of the stator. (bottom) Highlighted area in between the rotor and stator, where the shear rate magnitude (colour map) is the highest. The white arrows present the shear velocity field in between both walls.

Bibliography

[1] T. Graham. X. liquid diffusion applied to analysis. *Phil. Trans. R. Soc. Lond.*, 151:183–224, 1861.

[2] R. J. Hunter. *Zeta Potential in Colloid Science*. London: Academic Press, 1981.

[3] J. Mewis and N. Wagner. *Colloidal Suspension Rheology*. Cambridge University Press, 2012.

[4] A. Einstein. Über die von der molekularkinetischen theorie der wärme geforderte bewegung von in ruhenden flüssigkeiten suspendierten teilchen. *Ann Phys.*, 17:546–560, 1905.

[5] M. von Smoluchowski. Zur kinetischen theory der brownschen molekularbewegung und der suspensionen. *Ann Phys.*, 21:756–780, 1906.

[6] A. Sutherland. A dynamical theory of diffusion for non-electrolytes and the molecular mass of albumin. *Phil Mag.*, 9:781–785, 1905.

[7] R. G. Larson. *The structure and rheology of complex fluids*. Oxford University Press, 1999.

[8] C. W. Macosko. *Rheology: principles, measurements and applications*. Wiley-VCH, 1994.

[9] `https://www.youtube.com/watch?v=f_KAUcRBlWs`.

[10] N. Ohl and W. Gleissle. The characterization of the steady state shear and normal stress functions of highly concentrated suspensions formulated with viscoelastic liquids. *J. Rheol.*, 37:381–406, 1993.

[11] J. Bergenholtz, N. Willenbacher, N. J. Wagner, B. Morrison, D. van den Ende, and J. Mellema. Colloidal charge determination in concentrated liquid dispersions using torsional resonance oscillation. *J. Colloid Interface Sci.*, 202:430–440, 1998.

[12] J.C. van der Werff, C.G. de Kruif, C. Blom, and J. Mellema. Linear viscoelastic behavior of dense hard-sphere dispersions. *Phys. Rev. A*, 39:795–807, 1989.

[13] L. Kirschenmann. *Construction of two piezoelectric probes (PRV/PAV) for the viscoelastic properties of soft substances in frequencies 0.5 Hz - 2 kHz and 0.5 Hz - 7 kHz.* PhD thesis, University of Ulm, 2003.

[14] N. Willenbacher and C. Oelschlaeger. Dynamics and structure of complex fluids from high frequency mechanical and optical rheometry. *Curr. Opin. Colloid Interface Sci.*, 12:43–49, 2007.

[15] J. D. Ferry. *Viscoelastic properties of polymers.* John Wiley and Sons, 1980.

[16] E. M. Furst and T. M. Squires. *Microrheology.* Oxford University Press, 2017.

[17] F. T. Adler, W. M. Sawyer, and John D. Ferry. Propagation of transverse waves in viscoelastic media. *J. Appl. Phys.*, 20:1036–1041, 1949.

[18] G. B. Thurston. Theory of oscillation of a viscoelastic medium between parallel planes. *J. Appl. Phys.*, 30(12):1855–1860, 1959.

[19] W. M. Deen. *Analysis of Transport Phenomena.* Oxford University Press, 1998.

[20] J. L. Schrag. Deviation of velocity gradient profiles from the "gap loading" and "surface loading" limits in dynamic simple shear experiments. *Trans. Soc. Rheol.*, 21(3):399–413, 1977.

[21] M. Cagnon and G. Durand. Mechanical shear of layers in smectic-a and smectic-b liquid crystal. *Phys. Rev. Lett.*, 45:1418–1421, 1980.

[22] J .L. Gallani, L. Hilliou, and P. Martinoty. Abnormal viscoelastic behavior of side-chain liquid-crystal polymers. *Phys. Rev. Lett.*, 72:2109–2112, 1994.

[23] P. Martinoty and D. Collin. Piezo-rheometric measuring cell and corresponding piezo-rheometer. Patent no. US 7,784,329 B2, 2010.

[24] G. K. Auernhammer, D. Collin, and P. Martinoty. Viscoelasticity of suspensions of magnetic particles in a polymer: Effect of confinement and external field. *J. Chem. Phys.*, 124:204907, 2006.

[25] M. Roth, M. D'Acunzi, D. Vollmer, and G. K. Auernhammer. Viscoelastic rheology of colloid-liquid crystal composites. *J. Chem. Phys.*, 132:124702, 2010.

[26] B. Schroyen, J. W. Swan, P. Van Puyvelde, and J. Vermant. Quantifying the dispersion quality of partially aggregated colloidal dispersions by high frequency rheology. *Soft Matter*, 13:7897–7906, 2017.

[27] L. Kirschenmann and W. Pechhold. Piezoelectric rotary vibrator (prv) – a new oscillating rheometer for linear viscoelasticity. *Rheol. Acta*, 41:362–368, 2002.

[28] R. Bartolino and G. Durand. Plasticity in a smectic-a liquid crystal. *Phys. Rev. Lett.*, 39(1346-1349), 1977.

[29] P. Hébraud, F. Lequeux, and J.-F. Palierne. Role of permeation in the linear viscoelastic response of concentrated emulsions. *Langmuir*, 16(8296-8299), 2000.

[30] J. J. Crassous, R. Régisser, M. Ballauff, and N. Willenbacher. Characterization of the viscoelastic behavior of complex fluids using the piezoelastic axial vibrator. *J. Rheol.*, 49:851–863, 2005.

[31] C. P. Chen and R. S. Lakes. Apparatus for determining the viscoelastic properties of materials over ten decades of frequency and time. *J. Rheol.*, 33:1231–1249, 1989.

[32] C. A. M. Verbaan, G. W. M. Peters, and M. Steinbuch. Linear viscoelastic fluid characterization of ultra-high-viscosity fluids for high-frequency damper design. *Rheol. Acta*, 54:667–677, 2015.

[33] G. F. Christopher, J. M. Yoo, N. Dagalakis, S. D. Hudson, and K. B. Migler. Development of a mems based dynamic rheometer. *Lab Chip*, 10:2749–2757, 2010.

[34] W. P. Mason. Measurement of the viscosity and shear elasticity of liquids by means of a torsionally vibrating crystal. *Trans. Am. Soc. Mech. Eng.*, 69:359–370, 1947.

[35] T. M. Stokich, D. R. Radtke, C. C. White, and J. L. Schrag. An instrument for precise measurement of viscoelastic properties of low viscosity dilute macromolecular solutions at frequencies from 20 to 500 khz. *J. Rheol.*, 38:1195–1210, 1994.

[36] G. Fritz, W. Pechhold, N. Willenbacher, and N. J. Wagner. Characterizing complex fluids with high frequency rheology using torsional resonators at multiple frequencies. *J. Rheol.*, 47:303–319, 2003.

[37] J. L. Schrag and R. M. Johnson. Application of the birnboim multiple lumped resonator principle to viscoelastic measurements of dilute macromolecular solutions. *Rev. Sci. Instrum.*, 42:224–232, 1971.

[38] C. Blom and J. Mellema. Torsion pendula with electromagnetic drive and detection system for measuring the complex shear modulus of liquids in the frequency range 80-2500 hz. *Rheol. Acta*, 23:98–105, 1984.

[39] A. I. Romoscanu, M. B. Sayir, K. Häusler, and K. Servais. High frequency probe for the measurement of the complex viscosity of liquids. *Meas. Sci. Technol.*, 14:451–462, 2003.

[40] T. Nakken, K. D. Knudsen, A. Mikkelsen, and A. Elgsaeter. Dynamics of coaxial torsional resonators consisting of segments with different radii, material properties and surrounding media. *Rheol. Acta*, 34:235–247, 1995.

[41] T. Brack, S. Bolisetty, and J. Dual. Simultaneous and continuous measurement of shear elasticity and viscosity of liquids at multiple discrete frequencies. *Rheol. Acta*, 57:415–428, 2018.

[42] Y. Z. Wang, X. M. Xiong, and J. X. Zhang. New method of forced-resonance measurement for the concentrated and large-viscous liquid in the low frequency range by torsion resonator. *J. Rheol.*, 52:999–1011, 2008.

[43] Y.-Z. Wang, G.-H. Wang, X.-M. Xiong, B. Wang, L.-M. Zhang, and J.-X. Zhang. Viscoelastic measurement of complex fluids using forced oscillating torsion resonator with continuously varying frequency capability. *Rheol. Acta*, 49:1117–1126, 2010.

[44] H. J. McSkimin. Measurement of dynamic shear viscosity and stiffness of viscous liquids by means of traveling torsional waves. *J. Acoust. Sot. Am.*, 24:355–365, 1952.

[45] H. Nakajima and Y. Wada. New techniques for measuring complex shear viscosity of dilute polymer solutions at frequencies from 2 to 300 khz. *Polym. J.*, 1:727735, 1970.

[46] G. M. Glover, G. Hall, A. J. Matheson, and J. L. Stretton. A magnetostrictive instrument for measuring the viscoelastic properties of liquids in the frequency range 20-100 khz. *J. Phys. E: Sci. Instrum.*, 1:383–388, 1968.

[47] R. Gaglione, P. Attané, and A. Soucemarianadin. A new high frequency rheometer based on the torsional waveguide technique. *Rev. Sci. Instrum.*, 64:2326–2333, 1993.

[48] A. I. Romoscanu, M. B. Sayir, K. Häusler, and A. S. Burbidge. High frequency parallel plate probe for the measurement of the complex viscosity of liquids. *Rheol. Acta*, 42:462–476, 2003.

[49] T. Retsina, S. M. Richardson, and W. A. Wakeham. The theory of a vibrating-rod viscometer. *Appl. Sci. Res.*, 43:325–346, 1987.

[50] C. C. Hopkins and J. R. de Bruyn. Vibrating wire rheometry. *J. Non-newton. Fluid Mech.*, 238:205–211, 2016.

[51] P. Malara, R. Zullo, G. Filippone, L. Verdolotti, M. Lavorgna, A. Giogini, S. Avino, and G. Gagliardi. Rheology of complex fluids with vibrating fiber-optic sensors. *Sens. Actuators, A*, 264:219–223, 2017.

[52] C. E. Reed, K. Keiji Kanazawa, and J. H. Kaufman. Physical description of a viscoelastically loaded at cut quartz resonator. *J. Appl. Phys.*, 68:1993–2001, 1990.

[53] H. L. Bandey, S. J. Martin, R. W. Cernosek, and A. R. Hillman. Modeling the responses of thickness-shear mode resonators under various loading conditions. *Anal. Chem.*, 71:2205–2214, 1999.

[54] V. Buckin and E. Kudryashov. Ultrasonic shear wave rheology of weak particle gels. *Adv. Colloid Interface Sci.*, 89-90:401–22, 2001.

[55] S. Theobald, P. Schwarzenberger, and W. Pechhold. Measurements of the complex shear modulus of polymers under hydrostatic pressure usina the quartz resonator method. *High Pressure Res.*, 13:133–140, 1994.

[56] W. P. Mason, W. O. Baker, H. J. McSkimin, and J. H. Heiss. Measurement of shear elasticity and viscosity of liquids at ultrasonic frequencies. *Phys. Rev.*, 75:936–946, 1949.

[57] H. T. O'Neil. Reflection and refraction of plane shear waves in viscoelastic media. *Phys. Rev.*, 75:928–935, 1949.

[58] I. Alig, D. Lellinger, J. Sulimma, and S. Tadjbakhsch. Ultrasonic shear wave reflection method for measurements of the viscoelastic properties of polymer films. *Rev. Sci. Instrum.*, 68:1536–1542, 1997.

[59] A. Yoneda and M. Ichihara. Shear viscoelasticity of ultrasonic couplers by broadband reflectivity measurements. *J. Appl. Phys.*, 97:054901, 2005.

[60] I. Dufour, A. Maali, Y. Amarouchene, C. Ayela, B. Caillard, A. Darwiche, M. Guirardel, H. Kellay, E. Lemaire, F. Mathieu, and et al. The microcantilever: A versatile tool for measuring the rheological properties of complex fluids. *J. Sensors*, 2012:1–9, 2012.

[61] E. Lemaire, B. Caillard, M. Youssry, and I. Dufour. High-frequency viscoelastic measurements of fluids based on microcantilever sensing: New modeling and experimental issues. *Sens. Actuators, A*, 201:230–240, 2013.

[62] M. L. Mather, M. Rides, C. R. G. Allen, and P. E. Tomlins. Liquid viscoelasticity probed by a mesoscale piezoelectric bimorph cantilever. *J. Rheol.*, 56:99–112, 2012.

[63] S. L. Wingstrand, N. J. Alvarez, O. Hassager, and J. M. Dealy. Oscillatory squeeze flow for the study of linear viscoelastic behavior. *J. Rheol.*, 60:407–418, 2016.

[64] H. M. Laun, M. Rady, and O. Hassager. Analytical solutions for squeeze-flow with partial wall slip. *J. Non-newton. Fluid Mech.*, 81:1–15, 1999.

[65] G. H. Meeten. Effects of plate roughness in squeeze-flow rheometry. *J. Non-newton. Fluid Mech.*, 124:51–60, 2004.

[66] W. Pechhold, T. Gross, and L. Kirschenmann. Active axialschwingungssystem as viskoelastizitätssonde. Patent no. DE10162838 B4, 2008.

[67] W. Pechhold, U. Mayer, G. B. Raju, and O. Guillon. Piezo rotary and axial vibrator (prav) characterization of a fresh coating during its drying. *Rheol. Acta*, 50:221–229, 2011.

[68] A. M. Sánchez, R. Prieto, M. Laso, and T. Riesgo. A piezoelectric minirheometer for measuring the viscosity of polymer microsamples. *IEEE Trans. on Industrial electronics*, 55:427–436, 2008.

[69] S. Koganezawa, Y. Katsuta, R. Lu, H. Tani, and N. Tagawa. Device for direct measurement of dynamic viscoelastic properties of solid-state materials at frequencies higher than 1 khz. *Rheol. Acta*, 56:477–486, 2017.

[70] W. Bücking, B. Du, A. Turshatov, A. M. König, I. Reviakine, B. Bode, and D. Johannsmann. Quartz crystal microbalance based on torsional piezoelectric resonators. *Rev. Sci. Instrum.*, 78:074903, 2007.

[71] D. van den Ende, J. Mellema, and C. Blom. Driven torsion pendulum for measuring the complex shear modulus in a steady shear flow. *Rheol. Acta*, 31:194–205, 1992.

[72] S. Dinser, J. Dual, and K. Haeusler. Novel instrument for parallel superposition measurements. In *AIP Conference Proceedings*. The Society of Rheology, 2008.

[73] D. Johannsmann. Viscoelastic, mechanical, and dielectric measurements on complex samples with the quartz crystal microbalance. *Phys. Chem. Chem. Phys.*, 10:4516–4534, 2008.

[74] G. Sauerbrey. Verwendung von schwingquarzen zur wägung dünner schichten und zur mikrowägung. *Z. Phys.*, 155:206, 1959.

[75] C. C. White and J. L. Schrag. Theoretical predictions for the mechanical response of a model quartz crystal microbalance to two viscoelastic media: A thin sample layer and surrounding bath medium. *J. Chem. Phys.*, 111:11192–11206, 1999.

[76] H. Muramatsu, M. Kawamura, S. Tanabe, and M. Suda. Basic characteristics of quartz crystal sensor with interdigitated electrodes. *Anal. Chem. Res.*, 7:23–30, 2016.

[77] H. J. McSkimin. Use of high frequency ultrasound for determining the elastic moduli of small specimens. In *National Electronics Conference*, 1956.

[78] Y. Ono, C.-K. Jen, and M. Kobayashi. High temperature integrated ultrasonic shear and longitudinal wave probes. *Rev. Sci. Instrum.*, 78:024903, 2007.

[79] R. Berger, C. Gerber, H. P. Lang, and J. K. Gimzewski. Micromechanics: A toolbox for femtoscale science: 'towards a laboratory on a tip'. *Microelectron. Eng.*, 35:373–379, 1997.

[80] C. Bergaud and L. Nicu. Viscosity measurements based on experimental investigations of composite cantilever beam eigenfrequencies in viscous media. *Rev. Sci. Instrum.*, 71:2487–2491, 2000.

[81] N. Ahmed, D. F. Nino, and V. T. Moy. Measurement of solution viscosity by atomic force microscopy. *Rev. Sci. Instrum.*, 72:2731–2734, 2001.

[82] J. E. Elie Sader. Frequency response of cantilever beams immersed in viscous fluids with applications to the atomic force microscope. *J. Appl. Phys.*, 84:64–76, 1998.

[83] S. Boskovic, J. W. M. Chon, P. Mulvaney, and J. E. Sader. Rheological measurements using microcantilevers. *J. Rheol.*, 46:891–899, 2002.

[84] N. Belmiloud, I. Dufour, A. Colin, and L. Nicu. Rheological behavior probed by vibrating microcantilevers. *Appl. Phys. Lett.*, 92:041907, 2008.

[85] E. K. Reichel, C. Riesch, F. Keplinger, and B. Jakoby. Modeling of the fluid-structure interaction in a fluidic sensor cell. *Sens. Actuators, A*, 156:222–228, 2009.

[86] X. Lu, L. Hou, L. Zhang, Y. Tong, G. Zhao, and Z.-Y. Cheng. Piezoelectric-excited membrane for liquids viscosity and mass density measurement. *Sens. Actuators, A*, 261:196–201, 2017.

[87] E. K. Reichel, C. Riesch, F. Keplinger, C. E. A. Kirschhock, and B. Jakoby. Analysis and experimental verification of a metallic suspended plate resonator for viscosity sensing. *Sens. Actuators, A*, 162:418–424, 2010.

[88] F. Lucklum, E. K. Reichel, and B. Jakoby. Miniature density–viscosity measurement cell utilizing electrodynamic-acoustic resonator sensors. *Sens. Actuators, A*, 172:75–81, 2011.

[89] R. Kazys, R. Sliteris, R. Raisutis, E. Zukauskas, A. Vladisauskas, and L. Mazeika. Waveguide sensor for measurement of viscosity of highly viscous fluids. *Appl. Phys. Lett.*, 103:204102, 2013.

[90] V. Ruiz-Díez, J. Hernando-García, A. Ababneh, H. Seidel, and J. L. Sánchez-Rojas. In-liquid characterization of in-plane and high order out-of-plane modes of aln-based square microplates. *Microsyst. Technol.*, 22:1701–1708, 2015.

[91] G. C. DeNolf, L. Haack, J. Holubka, A. Straccia, K. Blohowiak, C. Broadbent, and K. R. Shull. High frequency rheometry of viscoelastic coatings with the quartz crystal microbalance. *Langmuir*, 27:9873–9879, 2011.

[92] Z. Zhao, X. Ji, R. Dimova, R. Lipowsky, and Y. Liu. Viscoelasticity of poly(ethylene glycol) solutions on supported lipid bilayers via quartz crystal microbalance with dissipation. *Macromolecules*, 48:1824–1831, 2015.

[93] E. K. Reichel, M. Heinisch, and B. Jakoby. *Resonant MEMS–Fundamentals, Implementation and Application*, chapter Fluid Property Sensors. Wiley-VCH Verlag GmbH & Co. KGaA, 2015.

[94] Y. Mitsuda, K. Osaki, J. L. Schrag, and J. D. Ferry. Infinite-dilution viscoelastic properties of star polystyrene with nine arms. *Polym. J.*, 4:24–28, 1973.

[95] Y. Mitsuda, J. L. Schrag, and J. D. Ferry. Infinite-dilution viscoelastic properties of comb-shaped polystyrenes. *Polym. J.*, 4:668–674, 1973.

[96] Y. Mitsuda, J. L. Schrag, and J. D. Ferry. Estimation of long-chain branching in ethylene-propylene terpolymers from infinite-dilution viscoelastic properties. *J. Appl. Polym. Sci.*, 18:193–202, 1974.

[97] M. Buchanan, M. Atakhorrami, J. F. Palierne, F. C. MacKintosh, and C. F. Schmidt. High-frequency microrheology of wormlike micelles. *Phys. Rev. E*, 72:011504, 2005.

[98] C. Oelschlaeger, M. Schopferer, M. Scheffold, and N. Willenbacher. Linear-to-branched micelles transition: A rheometry and diffusing wave spectroscopy (dws) study. *Langmuir*, 25:716–723, 2009.

[99] C. Oelschlaeger, M. Cota Pinto Coelho, and N. Willenbacher. Chain flexibility and dynamics of polysaccharide hyaluronan in entangled solutions: A high frequency rheology and diffusing wave spectroscopy study. *Biomacromolecules*, 14:3689–3696, 2013.

[100] L. Hellinckx and J. Mewis. Rheological behaviour of pigment dispersions as related to roller passage. *Rheol. Acta*, 8:519–525, 1969.

[101] W. P. Cox and E. H. Merz. Correlation of dynamic and steady flow viscosities. *J. Polymer Sci.*, 28:619–622, 1958.

[102] R. A. Lionberger and W. B. Russel. High frequency modulus of hard sphere colloids. *J. Rheol.*, 38:1885–1908, 1994.

[103] T. Shikata and D. S. Pearson. Viscoelastic behavior of concentrated spherical suspensions. *J. Rheol.*, 38:601–616, 1994.

[104] A. Weiss, M. Ballauff, and N. Willenbacher. High-frequency viscosity and shear modulus of sterically stabilized colloid particles as probed by torsional resonance oscillation. *J. Colloid Interface Sci.*, 216:185–188, 1999.

[105] J. J. Zanna, P. Stein, J. D. arty, M. Mauzac, and P. Martinoty. Influence of molecular parameters on the elastic and viscoelastic properties of side-chain liquid crystalline elastomers. *Macromolecules*, 35:5459–5465, 2002.

[106] M. Atakhorrami, G. H. Koenderink, J. F. Palierne, F. C. MacKintosh, and C. F. Schmidt. Scale-dependent nonaffine elasticity of semiflexible polymer networks. *Phys. Rev. Lett.*, 112:088101, 2014.

[107] L. Szántó, R. Vogt, J. Meier, D. Auhl, E. Van Ruymbeke, and C. Friedrich. Entanglement relaxation time of polyethylene melts from high-frequency rheometry in the mega-hertz range. *J. Rheol.*, 61:1023–1033, 2017.

[108] C. Clasen, B. P. Gearing, and G. H. McKinley. The flexure-based microgap rheometer (fmr). *J. Rheol.*, 50:883–905, 2006.

[109] PI Ceramic. *Piezoelectric Actuators: components, technologies, operation*, 2016.

[110] M. Rauer. *Personal communication.* PI Ceramic, 2018.

[111] R. H. Ewoldt, M. T. Johnston, and L. M. Caretta. *Complex Fluids in Biological Systems*, chapter Experimental Challenges of Shear Rheology: How to Avoid Bad Data, pages 207–241. Springer, 2015.

[112] J. L. Schrag, J. F. Guess, and G. B. Thurston. Shear-wave interference observed by optical birefringence induced in a viscoelastic liquid. *J. Appl. Phys.*, 36(6):1996–2000, 1965.

[113] W. B. Russel, D. A. Saville, and W. R. Schowalter. *Colloidal Dispersions*. Cambridge University Press, 1989.

[114] N. J. Wagner and J. F. Brady. Shear thickening in colloidal dispersions. *Phys. Today*, 62:27–32, 2009.

[115] B. J. Maranzano and N. J. Wagner. The effects of interparticle interactions and particle size on reversible shear thickening: Hard-sphere colloidal dispersions. *J. Rheol.*, 45:1205–1222, 2001.

[116] L.-N. Krishnamurthy, N. J. Wagner, and J. Mewis. Shear thickening in polymer stabilized colloidal dispersions. *J. Rheol.*, 49:1347–1360, 2005.

[117] D. Lootens, H. van Damme, Y. Hémar, and P. Hébraud. Dilatant flow of concentrated suspensions of rough particles. *Phys. Rev. Lett.*, 95:268302, 2005.

[118] M. Wyart and M. E. Cates. Discontinuous shear thickening without inertia in dense non-brownian suspensions. *Phys. Rev. Lett.*, 112:098302, 2014.

[119] J. R. Royer, D. L. Blair, and S. D. Hudson. Rheological signature of frictional interactions in shear thickening suspensions. *Phys. Rev. Lett.*, 116:188301, 2016.

[120] L. C. Hsiao, S. Jamali, E. Glynos, P. F. Green, R. G. Larson, and M. J. Solomon. Rheological state diagrams for rough colloids in shear flow. *Phys. Rev. Lett.*, 119:158001, 2017.

[121] B. A. de L. Costello, P. F. Luckham, and Th. F. Tadros. Investigation of the interaction forces of polymer-coated surfaces using force balance, rheology, and osmotic pressure results. *Langmuir*, 8:464–468, 1992.

[122] S. J. O'Shea, M. E. Welland, and T. Rayment. An atomic force microscope study of grafted polymers on mica. *Langmuir*, 9:1826–1835, 1993.

[123] G. Bryant, S. R. Williams, L. Qian, I. K. Snook, E. Perez, and F. Pincet. How hard is a colloidal "hard-sphere" interaction? *Phys. Rev. E*, 66:060501, 2002.

[124] C.-P. Hsu, S. N. Ramakrishna, M. Zanini, N. D. Spencer, and L. Isa. Roughness-dependent tribology effects on discontinuous shear thickening. *Proc. Natl. Acad. Sci. U.S.A.*, 115:5117–5122, 2018.

[125] J. F. Brady and J. F. Morris. Microstructure of strongly sheared suspensions and its impact on rheology and diffusion. *J. Fluid Mech.*, 348:103–139, 1997.

[126] J. F. Brady. The rheological behavior of concentrated colloidal dispersions. *J. Chem. Phys.*, 99:567–581, 1993.

[127] J. W. Swan, E. M. Furst, and N. J. Wagner. The medium amplitude oscillatory shear of semi-dilute colloidal dispersions. part i: Linear response and normal stress differences. *J. Rheol.*, 58:307–337, 2014.

[128] J. C. van der Werff, C. G. de Kruif, C. Blom, and J. Mellema. Linear viscoelastic behavior of dense hard-sphere dispersions. *Phys. Rev. A*, 39:795–807, 1989.

[129] A. T. J. M. Woutersen, J. Mellema, C. Blom, and C. G. de Kruif. Linear viscoelasticity in dispersions of adhesive hard spheres. *J. Chem. Phys.*, 101:542–553, 1994.

[130] R. A. Lionberger and W. B. Russel. Microscopic theories of the rheology of stable colloidal dispersions. *Adv. Chem. Phys.*, 111:399–474, 2000.

[131] L. Palangetic, K. Feldman, R. Schaller, R. Kalt, W. R. Caseri, and J. Vermant. From near hard spheres to colloidal surfboards. *Faraday Discuss.*, 191:325–349, 2016.

[132] M. Zanini, C.-P. Hsu, T. Magrini, E. Marini, and L. Isa. Fabrication of rough colloids by heteroaggregation. *Colloids Surf., A*, 532:116–124, 2017.

[133] G. Ourieva. *Instability in sterically stabilized suspensions.* PhD thesis, KU Leuven, 1999.

[134] Y. K. Teh, E.-J.and Leong, Y. Liu, B. C. Ong, C. C. Berndt, and S. B. Chen. Yield stress and zeta potential of washed and highly spherical oxide dispersions — critical zeta potential and hamaker constant. *Powder Technol.*, 198:114–119, 2010.

[135] A. Sierou and J. F. Brady. Accelerated stokesian dynamics simulations. *J. Fluid Mech.*, 448:115–146, 2001.

[136] Z. Cheng, J. Zhu, P. M. Chaikin, S.-E. Phan, and W. B. Russel. Nature of the divergence in low shear viscosity of colloidal hard-sphere dispersions. *Phys. Rev. E*, 65:041405, 2002.

[137] J. Bergenholtz, F.M. Horn, W. Richtering, N. Willenbacher, and N. J. Wagner. Relationship between short-time self-diffusion and high-frequency viscosity in charge-stabilized dispersions. *Phys. Rev. E*, 58:R4088–R4091, 1998.

[138] Z. Varga and J. W. Swan. Linear viscoelasticity of attractive colloidal dispersions. *J. Rheol.*, 59:1271–1298, 2015.

[139] A. A. Potanin and W. B. Russel. Hydrodynamic interaction of particles with grafted polymer brushes and applications to rheology of colloidal dispersions. *Phys. Rev. E*, 52:730–737, 1995.

[140] S. L. Elliott and W. B. Russel. High frequency shear modulus of polymerically stabilized colloids. *J. Rheol.*, 42:361–378, 1998.

[141] R. Zwanzig and R. D. Mountain. High-frequency moduli of simple fluids. *J. Chem. Phys.*, 43:4464, 1965.

[142] V. Gopalakrishnan and C. F. Zukoski. Effect of attractions on shear thickening in dense suspensions. *J. Rheol.*, 48:1321–1344, 2004.

[143] J. Bender and N. J. Wagner. Reversible shear thickening in monodisperse and bidisperse colloidal dispersions. *J. Rheol.*, 40:899–916, 1996.

[144] J. Bergenholtz, J., J. F. Brady, J. F., and M. Vicic. The non-newtonian rheology of dilute colloidal suspensions. *J. Fluid Mech.*, 456:239–275, 2002.

[145] W. J. Stark, P. R. Stoessel, W. Wohlleben, and A. Hafner. Industrial applications of nanoparticles. *Chem. Soc. Rev.*, 44:5793–5805, 2015.

[146] Y. Zhang, S. Ge, B. Tang, T. Koga, M. H. Rafailovich, J. C. Sokolov, D. G. Peiffer, Z. Li, A. J. Dias, K. O. McElrath, M. Y. Lin, S. K. Satija, S. G. Urquhart, H. Ade, and D. Nguyen. Effect of carbon black and silica fillers in elastomer blends. *Macromolecules*, 34:7056–7065, 2001.

[147] E. L. Cussler, S. E. Hughes, W. J. Ward, and R. Aris. Barrier membranes. *J. Membr. Sci.*, 38:161–174, 1988.

[148] C&EN. Building small, 2011.

[149] Y. Matsumoto, R. Chen, P. Anikeeva, and A. Jasanoff. Engineering intracellular biomineralization and biosensing by a magnetic protein. *Nat. Commun.*, 6:8721, 2015.

[150] D. W. Schaefer and R. S. Justice. How nano are nanocomposites? *Macromolecules*, 40(24):8501, 2007.

[151] D. M. Yebra and C. E. Weinell. *Advances in Marine Antifouling Coatings and Technologies*, chapter Key issues in the formulation of marine antifouling paints. Woodhead Publishing, 2009.

[152] C&EN. Fit to print, 2002.

[153] Y. Dzenis. Structural nanocomposites. *Science*, 319:419, 2008.

[154] S. K. Kumar, N. Jouault, B. Benicewicz, and T. Neely. Nanocomposites with polymer grafted nanoparticles. *Macromolecules*, 46:3199–3214, 2013.

[155] J. Vermant, S. Ceccia, M. K. Dolgovskij, P. L. Maffettone, and C. W. Macosko. Quantifying dispersion of layered nanocomposites via melt rheology. *J. Rheol.*, 51:429–450, 2007.

[156] M. E. Mackay, A. Tuteja, P. M. Duxbury, C. J. Hawker, B. Van Horn, Z. Guan, G. Chen, and R. S. Krishnan. General strategies for nanoparticle dispersion. *Science*, 311:1740, 2006.

[157] B. Stuyven, Q. Chen, W. Van de Moortel, H. Lipkens, B. Caerts, A. Aerts, L. Giebeler, B. Van Eerdenbrugh, P. Augustijns, G. Van den Mooter, J. Van Humbeeck, J. Vanacken, V. V. Moshchalkov, J. Vermant, and J. A. Martens. Magnetic field assisted nanoparticle dispersion. *Chem. Commun.*, pages 47–49, 2008.

[158] F. Müller, W. Peukert, R. Polke, and F. Stenger. Dispersing nanoparticles in liquids. *Int. J. Miner. Process.*, 74:S31–S41, 2004.

[159] C. Urban and P. Schurtenberger. Characterization of turbid colloidal suspensions using light scattering techniques combined with cross-correlation methods. *J. Colloid Interface Sci.*, 207:150–158, 1998.

[160] I. D. Block and F. Scheffold. Modulated 3d cross-correlation light scattering: Improving turbid sample characterization. *Rev. Sci. Instrum.*, 81:123107, 2010.

[161] D. J. Pine, D. A. Weitz, P. M. Chaikin, and E. Herbolzheimer. Diffusing-wave spectroscopy. *Phys. Rev. Lett.*, 60:1134–1137, 1988.

[162] G. Fortunato, A. Tenniche, L. Gottardo, and R. Hufenus. Development of poly-(ethylene terephthalate) masterbatches incorporating highly dispersed tio2 nanoparticles: Investigation of morphologies by optical and rheological procedures. *Eur. Polym. J.*, 57:75–82, 2014.

[163] W. You, W. Yu, and C. Zhou. Cluster size distribution of spherical nanoparticles in polymer nanocomposites: rheological quantification and evidence of phase separation. *Soft Matter*, 13:4088–4098, 2017.

[164] F. J. Galindo-Rosales, P. Moldenaers, and J. Vermant. Assessment of the dispersion quality in polymer nanocomposites by rheological methods. *Macromol. Mater. Eng.*, 296:331–340, 2011.

[165] K. A. Fröhlich, E. Mitrentsis, F. Clemens, B. Hoffmann, V. Michaud, and T. Graule. Assessment of the dispersion quality of refractive index-matched nanodispersions. *Appl. Rheol.*, 26:65050, 2016.

[166] Ph. Cassagnau. Melt rheology of organoclay and fumed silica nanocomposites. *Polymer*, 49:2183–2196, 2008.

[167] J.-F. Le Meins, P. Moldenaers, and J. Mewis. Suspensions in polymer melts. 1. effect of particle size on the shear flow behavior. *Ind. Eng. Chem. Res.*, 41:6297–6304, 2002.

[168] J. Mewis and N. J. Wagner. Thixotropy. *Adv. Colloid Interface Sci.*, 147-148:214–227, 2009.

[169] D. B. Genovese. Shear rheology of hard-sphere, dispersed, and aggregated suspensions, and filler-matrix composites. *Adv. Colloid Interface Sci.*, 171-172:1–16, 2012.

[170] C.W.J. Beenakker. The effective viscosity of a concentrated suspension of spheres (and its relation to diffusion). *Physica A*, 128:48–81, 1984.

[171] A. Zaccone, H. H. Winter, M. Siebenbürger, and M. Ballauff. Linking self-assembly, rheology, and gel transition in attractive colloids. *J. Rheol.*, 58:1219–1244, 2014.

[172] R. de Rooij, D. van den Ende, M. H. G. Duits, and J. Mellema. Elasticity of weakly aggregating polystyrene latex dispersions. *Phys. Rev. E*, 49:3038–3049, 1994.

[173] G. Colombo, S. Kim, T. Schweizer, B. Schroyen, C. Clasen, J. Mewis, and J. Vermant. Superposition rheology and anisotropy in rheological properties of sheared colloidal gels. *J. Rheol.*, 61:1035–1048, 2017.

[174] D. E. Koppel. Analysis of macromolecular polydispersity in intensity correlation spectroscopy: the method of cumulants. *J. Chem. Phys.*, 57:4814, 1972.

[175] G. K. Batchelor and J. T. Green. The determination of the bulk stress in a suspension of spherical particles to order c2. *J. Fluid. Mech.*, 56:401–427, 1972.

[176] I. M. Krieger and T. J. Dougherty. A mechanism for non-newtonian flow in suspensions of rigid spheres. *Trans. Soc. Rheol.*, 3:137–152, 1959.

[177] A.A. Potanin. On the self-consistent calculations of the viscosity of colloidal dispersions. *J. Colloid Interface Sci.*, 156:143–152, 1993.

[178] R. Wengeler and H. Nirschl. Turbulent hydrodynamic stress induced dispersion and fragmentation of nanoscale agglomerates. *J. Colloid Interface Sci.*, 306:262–273, 2007.

[179] V.S. Nguyen, D. Rouxel, and B. Vincent. Dispersion of nanoparticles: From organic solvents to polymer solutions. *Ultrason. Sonochem.*, 21:149–153, 2014.

[180] R . C. Sonntag and W. B. Russel. Structure and breakup of flocs subjected to fluid stresses: Ii. theory. *J. Colloid Interface Sci.*, 115(2):378–389, 1987.

[181] P. Akcora, S. K. Kumar, J. Moll, S. Lewis, L. S. Schadler, Y. Li, B. C. Benicewicz, A. Sandy, S. Narayanan, J. Ilavsky, P. Thiyagarajan, R. H. Colby, and J. F. Douglas. "gel-like" mechanical reinforcement in polymer nanocomposite melts. *Macromolecules*, 43(2):1003–1010, 2010.

[182] R. Mangal, P. Nath, M. Tikekar, and L. A. Archer. Enthalpy-driven stabilization of dispersions of polymer-grafted nanoparticles in high-molecular-weight polymer melts. *Langmuir*, 32(41):10621–10631, 2016.

[183] N. F. Carnahan and K. E. Starling. Equation of state for noninteracting rigid spheres. *J. Chem. Phys.*, 51:635, 1969.

[184] S. T. Milner, T. A. Witten, and M. E. Cates. Theory of the grafted polymer brush. *Macromolecules*, 21:2610–2619, 1988.

[185] B. J. Maranzano and N. J. Wagner. Thermodynamic properties and rheology of sterically stabilized colloidal dispersions. *Rheol. Acta*, 39:483–494, 2000.

List of Figures

1.1 Effect of interparticle interactions on the microstructure of a colloidal suspension 4

1.2 Schematic of a simple shear flow 5

1.3 Oscillatory shear flow experiments 6

2.1 Schematic of a propagating shear wave 14

2.2 Frequency range of high-frequency rheometrical techniques . . . 15

2.3 Overview of different subresonant rheometers 18

2.4 Overview of different bulk resonators 23

2.5 Overview of utrasound rheometers 25

2.6 Example of a microcantilever-based rheometer 27

3.1 Schematic of the homebuilt piezo shear rheometer 35

3.2 Model of the measurement cell for COMSOL MP simulations . 37

3.3 Simulation of the free displacement of the excitation unit . . . 40

3.4 Simulation of the detected input voltage for a Newtonian sample 41

3.5 Behaviour of the entire mechanical setup at the 1st resonance frequency 41

3.6 Simulated effect of the error in parallelism on the detected input voltage 42

3.7 Schematic of the signal generation and detection in the experimental setup 44

3.8 Raw signal of the input voltage 46

3.9 Influence of the transfer function of the electric circuit on the measured properties 47

3.10 Shielding of the piezoceramic stack and connections 49

3.11 Calibration results for three low-viscous polymeric samples . . 52

3.12 Limits of gap loading operation 53

3.13 Influence of shear wave propagation effects on the measured properties near the limit of gap loading 54

3.14 Correction for wave propagation effects on a low-viscous fluid . 56

3.15 Validation of the PSR with a quasi-Newtonian low-viscous PDMS grade: comparison between different setups 58

3.16 Validation of the PSR with a high-viscous PDMS grade 59

3.17 Validation of the PSR with a viscoelastic standard 60

3.18 Validation of the PSR with a quasi-elastic cured PDMS film . . . 61

3.19 Comparison between high-frequency measurements and TTS results for linear polymers 63

4.1 Example of the linear viscoelastic moduli, phase angle and complex viscosity for a PMMA suspension 72

4.2 Example of the linear viscoelastic moduli, phase angle and complex viscosity for a silica suspension 73

4.3 Derivation of the effective hydrodynamic volume fraction . . . 75

4.4 Effective volume fraction based on the topological parameters of the particles 76

4.5 Reduced moduli of smooth silica suspensions: illustration of the method of rescaling 78

4.6 Reduced viscous and elastic stresses of PMMA suspensions at $\phi_{eff} \approx 0.43$ 80

4.7 Concentration effect on the viscous stress contributions for PMMA particles with long stabilisation layers 82

4.8 Reduced viscous stresses of smooth and rough silica particles at various concentrations 84

4.9 Reduced elastic stresses of smooth and rough silica particles at various concentrations 85

4.10 Shear thickening behaviour of sterically stabilised PMMA suspensions 88

4.11 Shear thickening behaviour of smooth and rough silica suspensions 89

5.1 Rheological behaviour of partially dispersed suspensions 98

5.2 Relative loss moduli 99

5.3 Scaling behaviour of partially dispersed suspensions 101

5.4 Schematic of the measurement principle for deriving the dispersion quality 102

5.5 Evolution of the relative loss moduli with volume fraction . . . 103

5.6 Derivation of a DQI via the high-frequency loss moduli 104

5.7 Rescaling with the effective volume fraction 105

5.8 Evolution of the DQI during mixing 106

A.1 SEM pictures of different PMMA-*g*-PHSA particles. 120

A.2 SEM pictures of different silica particles. 121

A.3 Application of a 'Gleissle' shift factor 124

A.4 Simulations of the Ultra-Turrax mixer 125

List of Tables

2.1 Comparative overview of different high-frequency rheometrical techniques 16

3.1 Material coefficients of the piezoelectric material 37

3.2 Euler angles for the different orientations of the piezoelectric crystal 38

3.3 Boundary conditions applied for the simulations 39

3.4 Parameters of the piezoceramic stacks 45

4.1 Experimental parameters of the PMMA-*g*-PHSA particles . . . 68

4.2 Experimental parameters of the smooth and rough silica particles 69

5.1 Comparison of the mixing intensity and aggregate properties . 107

Curriculum Vitae

Bram Schroyen was born on the 29th of December 1989 in Hasselt, Belgium. He finished his high school education at Bovenbouw Sint-Michiel in 2007 in Mathematics-Science. Afterwards, he initiated his studies in architectural engineering at KU Leuven (Belgium) and eventually switched to general engineering. Bram obtained his Master's degree in Chemical Engineering at the faculty of Engineering Science in 2014. During his studies he performed an internship at BASF-YPC in Nanjing, China. He collaborated with Nestlé (Switzerland) for his Master thesis and designed and evaluated a subphase exchange cell for interfacial rheological measurements. After finishing his Master, Bram joined the lab of Soft Matter, Rheology and Technology at the Department of Chemical Engineering, KU Leuven, and started his doctoral studies. His project was supported by SIM Flanders and, under the supervision of Prof. Peter Van Puyvelde and Prof. Jan Vermant, aimed at characterising the local structure and properties of colloidal suspensions. During his PhD, Bram spent several periods abroad at ETH Zürich in Switzerland as a visiting researcher. He will join the Soft Materials group at the Department of Materials at ETH Zürich for a postdoc position after finishing his PhD, and will focus on the development of an add-on high-frequency rheometrical tool for in-situ measurements.

List of publications

Articles in internationally reviewed academic journals

- **Schroyen, B.**, Hsu, C.-P., Isa, L., Van Puyvelde, P., Vermant, J., Stress contributions in colloidal suspensions: influence of the surface topology. In preparation.
- **Schroyen, B.**, Van Puyvelde, P., Vermant, J., High-frequency bulk rheometry. In preparation.
- Scherz, L. F., Pepicelli, M., Messmer, D., **Schroyen, B.**, Vermant, J., Schlüter, D. A., Vlassopoulos, D., Dynamics of dendronized polymer monolayers - Film stability, nanostructuring and viscoelasticity at the air-water interface. In preparation.
- Pepicelli, M., Tregouët, C., **Schroyen, B.**, Tervoort, T. A., Monteux, C., Vermant, J., Dilatational viscoelasticity of a polymer multilayer system at an air-water interface. In preparation.
- **Schroyen, B.**, Swan, J. W., Van Puyvelde, P., Vermant, J. (2017). Quantifying the dispersion quality of partially aggregated colloidal dispersions by high frequency rheology. *Soft Matter*, 13(43), 7897-7906.
- Colombo, G., Kim, S., Schweizer, T., **Schroyen, B.**, Clasen, C., Mewis, J., Vermant, J. (2017). Superposition rheology and anisotropy in rheological properties of sheared colloidal gels. *Journal of Rheology*, 61(5), 1035-1048.
- **Schroyen, B.**, Zeynel Gunes, D., Vermant, J. (2017). A versatile subphase exchange cell for interfacial shear rheology. *Rheologica Acta*, 56(1), 1-10.

Meeting abstracts, presented at international scientific conferences and symposia

- **Schroyen, B.**, Hsu, C.-P., Isa, L., Swan, J., Van Puyvelde, P., Vermant, J., High frequency rheology of colloidal dispersions: From hard to soft, from smooth to frictional. *AERC*, Sorrento, Italy. April, 2018.
- **Schroyen, B.**, Swan, J. W., Van Puyvelde, P., Vermant, J.. A High Frequency Rheological Study of Partially Aggregated Colloidal Dispersions. *SoR meeting*, Denver, USA. October, 2017.
- **Schroyen, B.**, Van Puyvelde, P., Vermant, J., High Frequency Rheology on (partially) Aggregated Colloidal Dispersions : Exploring the Field. *SoftComp annual meeting*, Venice, Italy. May, 2017.
- **Schroyen, B.**, Zeynel Gunes, D., Vermant, J., A Versatile Subphase Exchange Cell for Interfacial Shear Rheology. *AERC*, Copenhagen, Denmark. April, 2017.
- **Schroyen, B.**, Van Puyvelde, P., Vermant, J., Characterising the State of Partially Dispersed Colloidal Suspensions by High-frequency Rheology. *AERC*, Copenhagen, Denmark. April, 2017.
- **Schroyen, B.**, Vermant, J., Van Puyvelde, P., Rhéologie à Hautes Fréquences Pour évaluer La Qualité Des Dispersions. *GFR-BGR meeting*, Lille, France. October, 2016.
- **Schroyen, B.**, Van Puyvelde, P., Vermant, J., High-frequency Rheology of Partially Dispersed Colloidal Suspensions. *ACS Colloids meeting*, Cambridge USA. June, 2016.
- **Schroyen, B.**, Van Puyvelde, P., Vermant, J., Rheology on Nanodispersions: A Tool for Assessing the Dispersion Quality. *SoftComp annual meeting*, Ancona, Italy. June, 2015.

Meeting abstracts, presented at other scientific conferences and symposia

- **Schroyen, B.**, Van Puyvelde, P., Vermant, J., High Frequency Rheology on Colloidal Dispersions: Insight into the Local Structure and Interactions. *Swiss Soft Days*, Villigen, Switzerland. March, 2018.
- **Schroyen, B.**, Van Puyvelde, P., and Vermant, J., Investigating Partially Dispersed Colloidal Suspensions by High-frequency Rheology. *SCS Fall meeting*, Zürich, Switzerland. September, 2016.

Meeting abstracts, presented at professionally oriented conferences and symposia

- **Schroyen, B.**, Vermant, J., Van Puyvelde, P., Quantitative Characterization of the Dispersion Quality Based on Mechanical Contrast. M2i meeting, Noordwijkerhout, Netherlands. December, 2017.
- **Schroyen, B.**, Vermant, J., Van Puyvelde, P., Towards More Efficient Dispersion Processes: A Mechanical Approach. *SIM User meeting*, Antwerp, Belgium. June, 2017.
- **Schroyen, B.**, Vermant, J., Van Puyvelde, P., Towards an In-situ Tool to Assess Dispersion Quality. *SIM User meeting*, Ghent, Belgium. October, 2015.

Printing by





FACULTY OF ENGINEERING SCIENCE
DEPARTMENT OF CHEMICAL ENGINEERING
SOFT MATTER, RHEOLOGY AND TECHNOLOGY
Celestijnenlaan 200F box 2424
B-3001 Leuven
https://cit.kuleuven.be/smart